VISUAL SIGNAL PROCESSING OF THE MYOPIC MOUSE RETINA

SEEMA BANERJEE

PhD

The Hong Kong Polytechnic University

2021

The Hong Kong Polytechnic University

School of Optometry

VISUAL SIGNAL PROCESSING OF THE MYOPIC MOUSE RETINA

Seema Banerjee

A thesis submitted in partial fulfilment of the requirements for the degree of Doctor of Philosophy

July 2020

CERTIFICATE OF ORIGINALITY

I hereby declare that this thesis is my own work and that, to the best of my knowledge and belief, it reproduces no material previously published or written, nor material that has been accepted for the award of any other degree or diploma, except where due acknowledgment has been made in the text.

_____ **(Signed)**

Seema Banerjee

_____ **(Name of the student)**

Abstract

Myopia is a substantial public health challenge worldwide. It affects more than 80% of the population of Hong Kong and more than 40% of individuals over the age of 12 years in the United States. Although it is well established that defocused images alter eye growth and ocular refraction, the mechanism, and effects of defocused images on the signaling of retinal ganglion cells (RGCs) that contribute to either emmetropization or refractive error remain unknown. Therefore, the responses of populations of RGCs in dark-adapted mouse retinas to the projection of defocused images of different dioptric powers and spatial frequencies were recorded using a 256 channel Multi-Electrode Array (MEA).

The retina could reflect the projected image, leading to a dramatic change in the firing pattern when presented with the defocused image. The responses of RGCs were also affected by the application of dopamine D1 and D2 receptor antagonists and agonists. In addition, when defocused images were projected, the synchrony firing patterns between the OFF-Delayed RGCs with other delayed response RGCs or displaced amacrine cells (ACs) were lost, which may be related to edge detection. The results suggest that defocused images could change the multineuronal firing pattern in the mouse retina. Such a change in the population of RGC activities may serve as an early step in myopia development in the retina.

Gap junctions play important functional roles, such as signal averaging, noise reduction, and neuronal synchronization to code fundamental visual information in the retinal circuit. Modulation of gap junctions contributes to retinal plasticity, which enables the retina to adapt to visual inputs as self-adjusting neuronal networks. AII ACs coupled by connexin36 (Cx36) are actively modulated through phosphorylation at serine 293 via dopamine in the mouse retina. Therefore, insight into the regulation of Cx36 function is important to understand the visual signaling processes in both the normal and

myopic retina. Form deprivation mouse myopia models were used to evaluate the expression patterns of Cx36-positive plaques (structural assay) and the state of Cx36 phosphorylation (functional assay) in AII ACs.

The results showed increased Cx36 phosphorylation in the myopic retina compared to the normal control animals, but there was no change in the expression of Cx36. The results indicate increases in the functional gap junction coupling of AII ACs in the myopic retina, a mechanism that potentially adjusts to alter the noisy signal condition.

In summary, this study showed that the population of RGCs/displaced ACs in the retina can respond differently to focused and defocused images and increases in the functional gap junction coupling of AII ACs in the myopic retina. These findings may be the basis for the proposed retina-to-sclera signaling pathway. Retinal signaling might be the first and the most important step in triggering myopia and may also serve as a continuous key signal in myopia development.

List of Presentations, Publications, and Awards arising from the thesis.

Publications

1. Banerjee, S., Wang, Q., So, C. H., & Pan, F. (2020). Defocused Images Change Multineuronal Firing Patterns in the Mouse Retina. *Cells, 9*(3), 530.

2. Banerjee, S., Wang, Q., Zhao, F., Tang, G., So, C., Tse, D., . . . Pan, F. (2020). Increased Connexin36 Phosphorylation in AII Amacrine Cell Coupling of the Mouse Myopic Retina. *Frontiers in Cellular Neuroscience, 14*(124). doi:10.3389/fncel.2020.00124.

3. Wang, Q., Banerjee, S., So, C., Qiu, C., Lam, H. C., Tse, D., . . . Pan, F. (2020). Unmasking inhibition prolongs neuronal function in retinal degeneration mouse model. *Faseb j*. doi:10.1096/fj.202001315RR

4. Seema Banerjee, George Tang, Sze Wan Shan, King Kit Li, Chi-Wai Do, Feng Pan. Functional connexin36 increased in the myopic chicken retina, "under consideration" by Experimental Eye Research.

5. Qin Wang[1], Seema Banerjee[1], ChungHim So[1], YingHon Sze[1], Thomas Chuen Lam[1], Chi-Ho To[1], Feng Pan[1,2]* Low dose atropine might intervene alpha ganglion cell signaling in the mouse retina, "under revision" by Frontiers in Cellular Neuroscience.

Conference Presentations

1. Banerjee S., Wang Q., and Pan F. "A preliminary data on the mechanism of myopia: a multielectrode array approach". *Presented at the International Conference of Vision and Eye Research (iCover), 2018. Hong Kong.*

2. Banerjee S., Wang Q., and Pan F. "Defocused images affect the multineuronal firing pattern in the mouse retina". Presented at *The ABCT Research Postgraduate Symposium in the Biology Discipline, (2019). Hong Kong.*

3. Banerjee S., Wang Q., and Pan F. "Defocused images affect the multineuronal firing pattern in the mouse retina: a multielectrode array study". Presented at *Association for Research in Vision and Ophthalmology (ARVO), 2018. Vancouver, Canada.*

Award

"Best Poster" Presentation Award

The ABCT Research Postgraduate Symposium in the Biology Discipline, (2019) held in Hong Kong for the Poster entitled "Defocused images affect the multineuronal firing pattern in the mouse retina".

Acknowledgments

First of all, I would like to acknowledge with a deep sense of reverence, my gratitude towards my parents: Maa, Baba, and my brothers Mithun and Mrinal. Without their support, prayers, enthusiasm, and availability, I would have not reached where I am.

I am highly indebted to The Hong Kong Polytechnic University, and The School of Optometry for allowing me to fulfill my dream.

I would like to express my sincere gratitude and profound respect to my supervisor and mentor Dr. Feng PAN, who has helped and encouraged me throughout this Ph.D. journey. He has the substance of genius, always taught me to be professional and to do the right thing even when the path got tough. Without his persistent support and patience, I would have not reached my goal.

Besides my supervisor, I would like to sincerely thank my co-supervisor Dr. Chi-Wai DO, for his insightful comments and encouragement, but also for the hard question which inspired me to widen my research from various perspectives.

I would also like to pay my special regards and appreciation to Prof. Maureen Boost and Dr. Lily Chan, for helping me in preparation for my thesis and their invaluable detailed advice.

“Teachers affect eternity, no one can tell where their influence stops” a famous quote by Henry Brooks Adam, I would like to thank Dr. Ranjan Mukherjee and Dr. Rohit Khanna for being the most wonderful teachers in my life and influencing me to achieve what I dreamt off.

My completion of this project could not have been possible without the support of my lab mates, for their energy, understanding, stimulating discussion and for all the fun and enjoyment we have had in the last three years. And the best part, we always taught and shared our knowledge.

Table of Contents

List of Figures

List of tables

List of abbreviations

AC	Amacrine cell
AII ACs	AII amacrine cells
AL	Axial length
BC	Bipolar cell
CB	Cone bipolar
CCP	cross-correlogram profiles
d/ACs	Displaced amacrine cells
D1R	Dopamine 1 receptor
D2R	Dopamine 2 receptor
GC	Ganglion cell
HC	Horizontal cell
HS	High sensitive
ILS	Intermediate low sensitive
IPL	Inner plexiform layer
IS	Intermediate sensitive
IR	Infrared
LS	Low sensitive
MEA	Multi-electrode array
OCT	Optical coherence tomography
OPL	Outer plexiform layer
OLED	Organic light-emitting display
RB	Rod bipolar
RGC	Retinal ganglion cell
YFP	Yellow fluorescence protein

CHAPTER 1 Introduction and overview

1.1 Background

“Clear at near and blur at far” this poetic rendition explains the definition of Myopia very well. Despite having a long history, enormous research, and studies, the aetiology and progression of myopia remain unknown. It has become a major public health issue globally, affecting more than 80% of the population in Hong Kong (Goh & Lam, 1994; Morgan, Ohno-Matsui, & Saw, 2012). Its prevalence and progression are causing a global medical burden. According to The World Health Organization (WHO), by 2050 more than 50% of the global population will be myopic (Holden et al., 2016).

Excessive elongation of the axial length causes the thinning of the ocular coats resulting in high myopia. High myopia is associated with an increased risk of vision loss due to several ocular complications such as myopic maculopathy, retinal detachment, cataract, and glaucoma (Morgan et al., 2018; Ohno-Matsui, 2016). Therefore, understanding the underlying mechanism of myopia's development is very important to prevent it.

Previously reported use of form depriving methods such as a diffuser, occluder, or suturing methods can induce myopia in chicken (Schaeffel, Glasser, & Howland, 1988), mouse (Barathi, Boopathi, Yap, & Beuerman, 2008), monkey (Smith III & Hung, 2000), tree shrew (McBrien & Norton, 1992), all these studies have provided strong evidence that defocused images responsible for the alteration of eye growth and refractive status of the eye.

1.1.1 The Neuronal Retina (a brief introduction to its layers)

The retina is the most important structure of the eye and the site of major eye diseases, including pathological myopia, maculopathy, diabetic retinopathy, glaucoma, and retinal detachment. Eye growth, which changed in myopia, is largely governed by the retina. Therefore, it is important to understand the visual signal processes in the retina to understand myopia. The retina is the innermost neural layer of the eye which is light sensitive and consists of several layers of neurons that are interconnected via various electrical or chemical synapses. It is a sandwich-like structure consisting of three layers of neurons- photoreceptors (outer nuclear layer), bipolar cells (inner nuclear layer), and ganglion cell layer, between the two layers of synaptic connection, the inner and outer plexiform layers (**figure 1.1**). The visual signals received by photoreceptors are then converted into electrical signals to retinal ganglion cells (RGCs) via bipolar cells.

This study mainly focuses on the RGCs firing pattern, classifications of different types of RGCs based on light-evoked potentials, and its signaling in the mouse retina. We have also discussed the role of amacrine cells (ACs), especially AII amacrine cells (AII ACs), and gap junction functions in the myopic mouse retina.

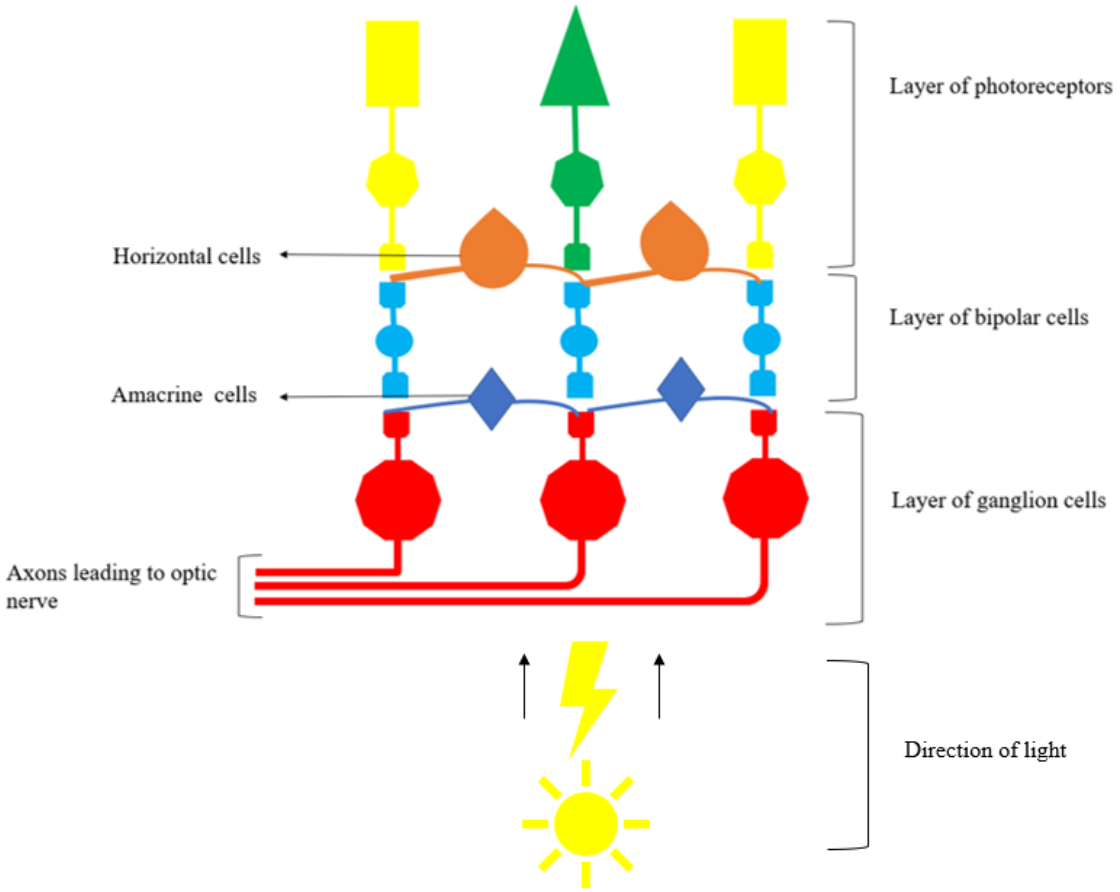

Figure 1.1 Illustration of the basic structure of retinal layers of the human eye.

1.1.1.1 The Photoreceptors

The retina consists of two main kinds of photoreceptors, – Rods and Cones. Rod photoreceptors detect dim signals under scotopic conditions whereas cone detects bright and colour signals under photopic conditions. Photoreceptors hyperpolarize to light stimulation takes place in the visual phototransduction cascade. Phototransduction is the process that occurs in the retina, in which light

energy is converted into electrical signals and can be detected by the retinal photoreceptors. The phototransduction cascade is a set of steps in the molecular level described below in the flow chart (**figure 1.2**).

In the human retina, more than 95% of the photoreceptors are rods, equating to approximately 100 million (Massey, 2006). In the mouse retina, 97% of rods make the total photoreceptors (Fu & Yau, 2007). Rod photoreceptors are very sensitive and can transduce absorption of single photons which allows them to be active for night vision, whereas cones are less sensitive and provide for daytime vision. There are intermediate light conditions like twilight, both rods and cones are sensitive (Demb & Singer, 2015).

The rod and cone photoreceptors are linked to the ON and OFF bipolar cells and segregate into ON and OFF pathways for encoding the change in the light stimulus intensity. Cones are found in a conical-shaped structure, whose cell bodies are below the outer limiting membrane, and they are highly concentrated in the foveal region. In contrast, rods are located in slim, rod-shaped structures and their cell bodies are found in the outer nuclear layer, below the cone cell bodies. Both photoreceptors are supported by the outer pigmented epithelium layer. The rods consist of the visual pigment, -rhodopsin. Cone photoreceptors have cone opsins as their visual pigments, based on the opsin molecule structure. Cones of distinctive wavelength sensitivity and the resulting pathways to the brain are responsible for color recognition in the visual system. Photoreceptors are known to supply parallel bipolar cell pathways by synapsing onto 12 different types of bipolar cells (Demb & Singer, 2015) and at this synapse, the responses are split into parallel signaling streams.

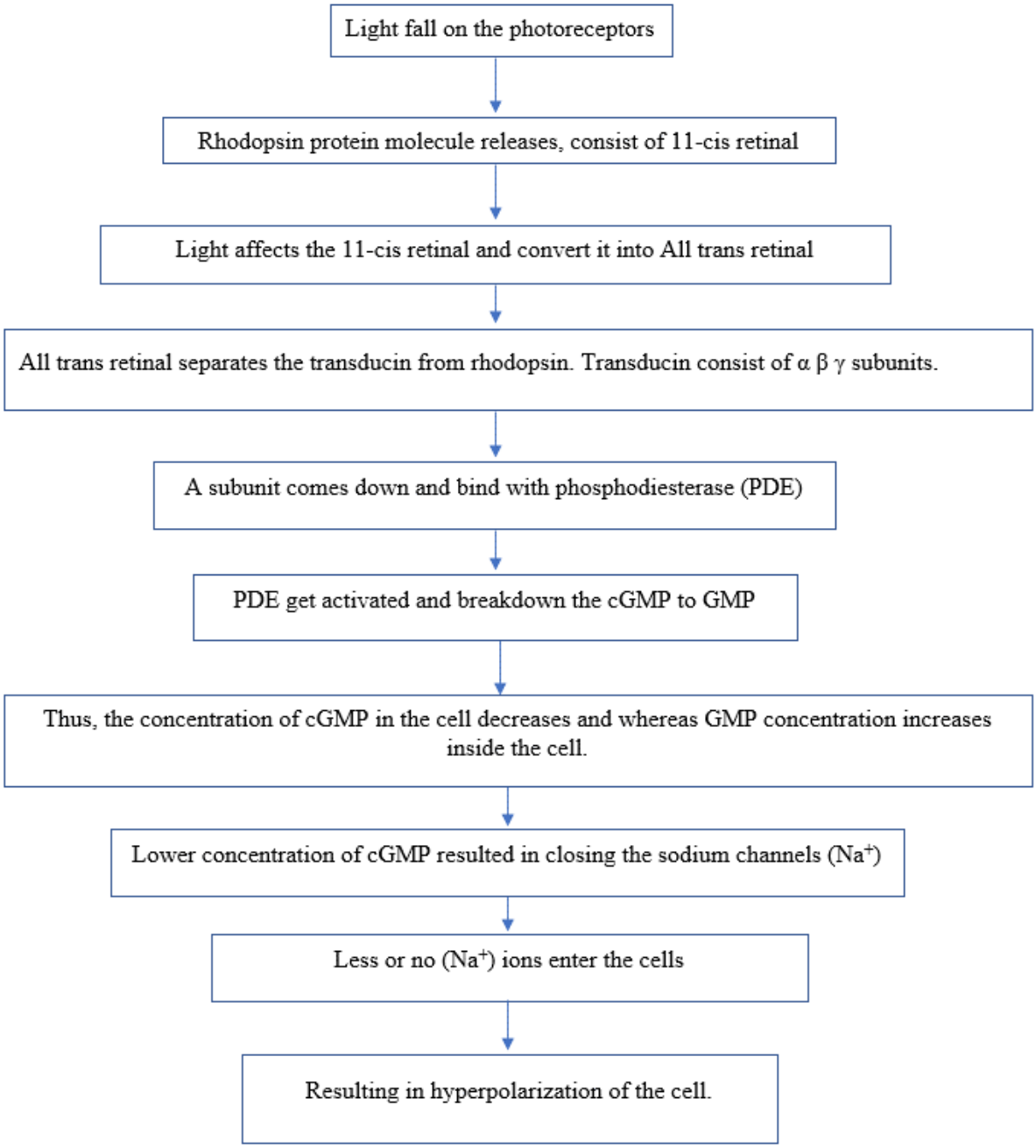

Figure 1.2 flowchart describing the steps in the visual phototransduction cascade.

1.1.1.2 Bipolar Cells

Bipolar cells are the connecting thread between the Photoreceptor cells and the RGCs; it carries the light signals from photoreceptors to amacrine cells (ACs) and RGCs. Strettoi and Masland (Strettoi & Masland, 1995) reported that bipolar cells make up to 41 % of total cells in the inner nuclear layer (INL) and are subdivided into two kinds, rod bipolar cells and cone bipolar cells according to their connection with rod or cone respectively.

There are 13 distinct types of bipolar cells (12 cone bipolar cells and 1-rod bipolar cell) identified in mouse retina (Ghosh, Bujan, Haverkamp, Feigenspan, & Wassle, 2004; H. Wässle, Puller, Müller, & Haverkamp, 2009). Each of these bipolar cells receives inputs from the photoreceptors and transforms it into different functions such as contrast, polarity, chromaticity, and temporal profile (Euler, Haverkamp, Schubert, & Baden, 2014). All bipolar cell terminals receive both feedforward and feedback mechanisms at their synaptic terminals and a highly selective inhibitory input from the amacrine cells (Masland, 2012). Bipolar cells act directly or indirectly by transmitting signals from the photoreceptors layer to the ganglion cell layer and horizontal cell layer.

1.1.1.3 Horizontal Cells

In some species horizontal cells (HCs) morphologically are of two types and largely interconnected with different gap junctions. In mouse and rat retina only 1 type of axon bearing horizontal cells is found (Masland, 2001, 2012). They are extensively arranged laterally and form the large cell network across the outer plexiform layer (OPL). Horizontal cells provide lateral inhibition to the dendrites which give rise to the center-surround inhibition, responsible for edge enhancements from its

background (Hartline, 1938; Masland, 2012). Jackman and Kramer (Jackman, Babai, Chambers, Thoreson, & Kramer, 2011) have identified that there is both negative and positive feedback provided by the horizontal cells to the cone photoreceptors which is regulated by the AMPA receptors on the HCs. The horizontal cells provide negative feedback to cones and direct feed-forward to the bipolar cells (BCs) (Thoreson & Mangel, 2012). The HCs depolarized in the absence of light thus hyperpolarizes the neighbouring photoreceptors and releases glutamate. In contrast, in the presence of light, the HCs are hyperpolarized and depolarizes the neighbouring photoreceptors with minimal or no glutamate release. Therefore, horizontal cells participate in providing negative feedback to the retinal photoreceptor cells.

Feedback and feed-forward mechanisms from the horizontal cells participate in important functions to process various visual characteristics such as light adaptation, color constancy, generating color opponency, and enhancing the ability to identify spatial differences (Thoreson & Mangel, 2012).

1.1.1.4 The Amacrine Cells (ACs)

More than 30 types of different kinds of amacrine cells are identified in the mammalian retina (Masland, 2012). Amacrine cells are the diverse class of neurons in the inner plexiform layer of the retina. They receive synaptic inputs from bipolar cells and other amacrine cells and provide the signal input to amacrine cells, ganglion cells, and feedback to bipolar cells.

Amacrine cells lack axon, firstly named by Cajal in 1893. But Lin and Masland in 2006 (Lin & Masland, 2006) reported about some of ACs covered large fields with axon like processes which looks like real axon. Most of the amacrine cells are coupled by the gap junctions to amacrine cells, ganglion cells, or other types of amacrine cells (Bloomfield & Volgyi, 2009).

AII amacrine cells (ACs) are the most abundant amacrine cells (AC) type about 11% (Vaney, 1985, 1991) in the retina coupled by connexin36 gap junctions (Mills, O'Brien, Li, O'Brien, & Massey, 2001). AII ACs play a major role in the primary rod pathway involving electrical signals between each other (Bloomfield & Volgyi, 2009). AII ACs transmit both rod and cone-driven signals to the ON and OFF pathway in the inner retina. AII ACs coupled with Cx36 is present on the cross-over of the ON-OFF pathway and segregate signals to the respective ON and OFF pathway (Bloomfield & Völgyi, 2004) and actively modulated through phosphorylation at serine 293 via dopamine in the mouse retina. The AII ACs dendrites are spread over the entire IPL, and differentiated into 5 strata (Ghosh et al., 2004).

AII ACs are electrically coupled via gap junctions to the ON- cone bipolar cells (ON CBP) in the sublamina b (Famiglietti & Kolb, 1975; Kolb & Famiglietti, 1974) forming a heterologous gap junction coupling via Cx36/45 mainly in strata 3 and 4; in contrast, AII coupled to the other AII cells (AII/AII ACs) in the strata 5 (Strettoi, Dacheux, & Raviola, 1990; Strettoi, Raviola, & Dacheux, 1992) forming homologous gap junction coupling. This AII/AII homologous gap junction structure is formed by connexin 36 subunit (Feigenspan, Teubner, Willecke, & Weiler, 2001; Mills. et al., 2001). Dopamine affects the Cx36 gap junction coupling in AII ACs by activating protein kinase A (PKA) (Kothmann, Massey, & O'Brien, 2009). As it is well established, that dopamine plays a significant role in myopia development and the Cx36 gap is modulated through Ser293 via dopamine (Kothmann et al., 2009; Zhou, Pardue, Iuvone, & Qu, 2017), therefore it is important to understand the mechanism and effect of Cx36 gap junction role in the myopic retina.

1.1.1.5 The Retinal Ganglion Cell

There are more than 40 types of different kinds of RGCs (Baden et al., 2016) (**figure 1.3**). RGCs respond to diverse visual features, such as increases or decreases in light intensity color, or moving objects (Masland, 2001). Previous studies have classified cells as ON, OFF, or ON-OFF and transient or sustained type based on the RGCs response to the light stimuli (Lettvin, Maturana, McCulloch, & Pitts, 1959; Werblin & Dowling, 1969).

In electrophysiological retinal recordings, cells respond to light increments (ON cells) while others are activated by light decrements (OFF cells). In a mature retina, the circuitry mechanism underlying ON and OFF responses are well developed. Specifically, the dendrites of ON and OFF-centre (RGCs) are stratified in a different sublaminar layer of the inner plexiform layer (IPL), where they are innervated by spatially segregated ON- and OFF-cone bipolar cell inputs. They are also segregated into ON and OFF sublamina layer of the IPL (**Figure 1.4**).

According to the previous study based on a range of threshold intensities calculated from the intensity–response functions of the population of dark-adapted ON and OFF RGCs, the ON and OFF cells could be classified into four groups high (HS), intermediate (IS), low-intermediate (LIS) and low (LS) sensitivity (Pan et al., 2016).

Based on the discrete properties and physiological properties RGCs are found to be Transient (brief spike burst) and Sustained (maintained spikes) types (Murphy & Rieke, 2006; Pang, Gao, & Wu, 2003). A recent study reported newly identified RGCs types in mouse retina known as ON Delayed RGC (Mani & Schwartz, 2017). Where they have also mentioned that role of ON-Delayed RGCs might be responsible for image focus, However, they have not shown any data on OFF-Delayed RGCs

recording. It is also reported that the normal emmetropization process possibly depends on the ON-pathways of the retina (Chakraborty et al., 2015).

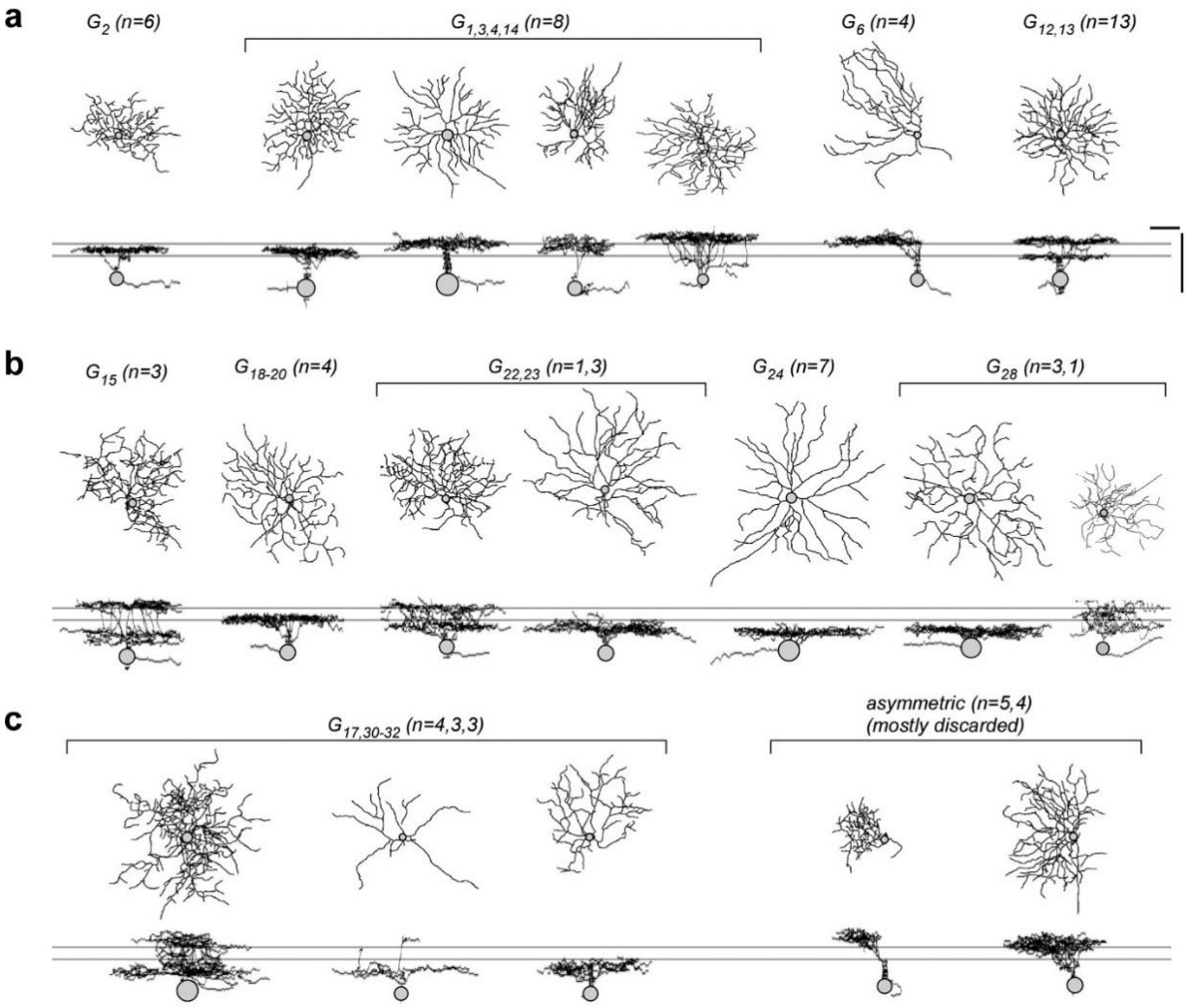

Figure 1.3 Mapping RGCs group to morphology, scale bar 50µm, (Baden et al., 2016)

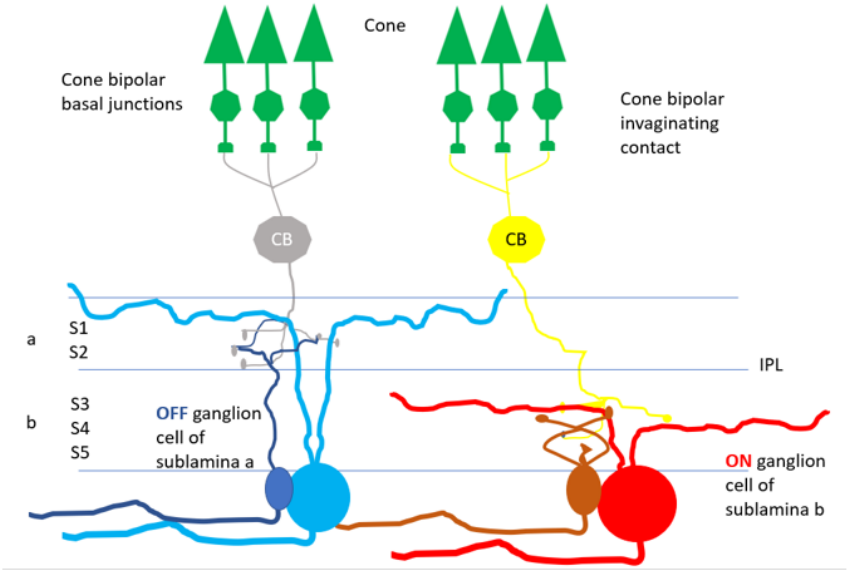

Figure 1.4 Illustration of organization of ON and OFF-central ganglion cells into sublamina a and b.

1.1.2 Photoreceptors: Vertical Pathways

The retinal circuit consists of two major pathways for functioning. Firstly, the cone pathway is also known as the vertical pathway, and secondly, the rod pathway, considered as the primary pathway.

In the cone pathway, signal transfer vertically from cone photoreceptors to cone bipolar cell and then to RGCs. This is considered the shortest and majorly available pathway circuit in the retina **(figure 1.5)**. In cone pathways when light falls on the photoreceptors, it converts the light signals to electrical signals. The signals then further reach the bipolar cells via chemical synapses and are finally transmitted through the ON and OFF pathway to the RGCs.

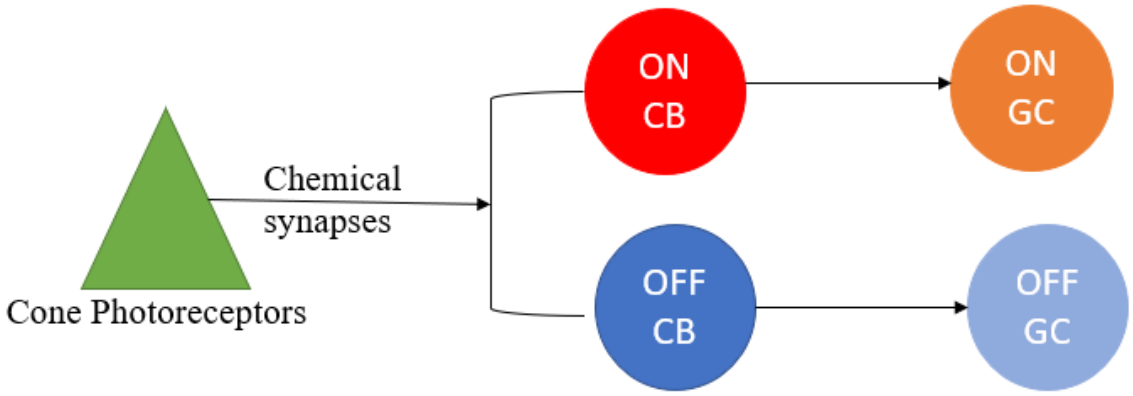

Figure 1.5 Arrow diagram represents the cone pathway in the retinal circuitry. (CB) cone bipolar; (GC) ganglion cell.

Rod pathway consists of a primary pathway along with two alternate pathways.

- In the primary rod, pathway signals are transferred from rods to rod bipolar cells and then to AII cells. Further on AII cells make sign-conserving electrical synapses via gap junction with ON cone bipolar cells and sign-inverting inhibitory chemical synapses with OFF cone bipolar cells. Resulting, the ON and OFF cone bipolar cells will make excitatory chemical synapses with ON and OFF ganglion cells (Bloomfield & Volgyi, 2009) (**figure1.6**).
- In the secondary pathway signals from rod photoreceptors are transferred directly from rods to cone photoreceptors through gap junctions between rods and cones. Then the rod signals are transmitted to ON and OFF cone bipolar cells, which further transport the signals via cone pathway to retinal ganglion cells in the inner retina (Bloomfield & Volgyi, 2009) (**figure 1.7**).

- In the tertiary pathway, the rods photoreceptors connect directly through chemical synapses with a subgroup of OFF bipolar cells, which further transfer the signals to a few OFF retinal ganglion cells. This pathway possibly has a counterpart in the ON circuitry (**figure 1.8**) (Bloomfield & Volgyi, 2009).

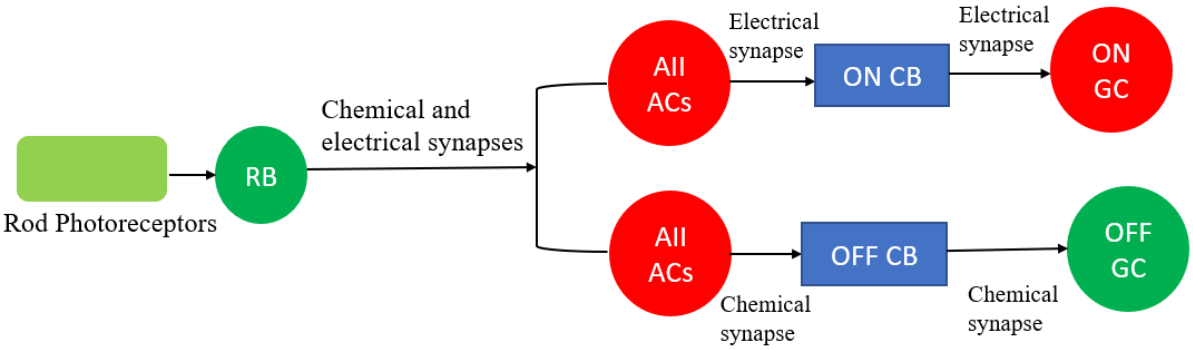

Figure 1.6 Arrow diagram represents the primary rod pathway in the retinal circuitry. (RB) rod bipolar; (CB) cone bipolar; (GC) ganglion cell; (AII ACs) AII amacrine cells

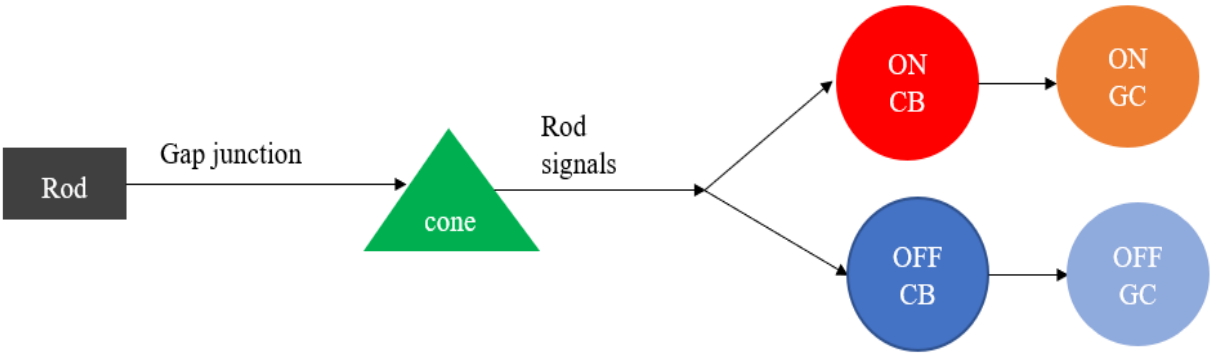

Figure 1.7 Arrow diagram represents the secondary rod pathway in the retinal circuitry. (CB) cone bipolar; (GC) ganglion cell; (AII ACs) AII amacrine cells

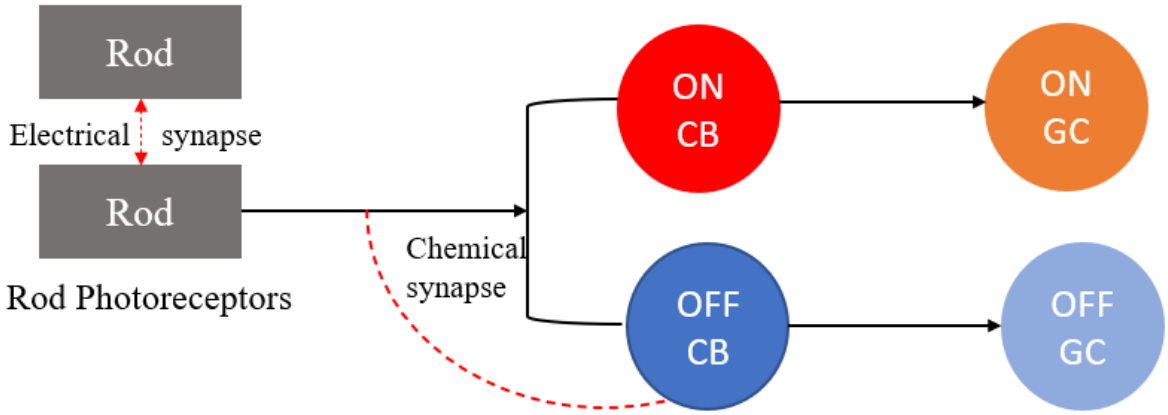

Figure 1.8 Arrow diagram represents the tertiary rod pathway in the retinal circuitry. (BC) bipolar cell; (GC) ganglion cell.

1.1.3 Gap Junctions in the Retinal Circuitry

Gap junctions are also known as the electrical synapses which form in between the plasma membrane of two neighbouring cells, that are electrically conductive and allowing a pathway to exchange of ions and small molecules between two cells or channels (Bloomfield & Volgyi, 2009; Söhl, Maxeiner, & Willecke, 2005).

Gap junctions are composed of hemichannels known as connexon, each of these connexons are consist of 6 connexins surrounding with a central pore for the exchange of ion and molecules between the connected cells **(figure 1.9 a)**. These pores form an intracellular channel between the connected cells (Bloomfield & Volgyi, 2009; Vaney & Weiler, 2000). To form a functional gap junction minimum of two hemichannels are required (Goodenough & Paul, 2003; Vaney & Weiler, 2000). There are more than 20 connexins identified in humans and 19 in mouse retina (Willecke et al., 2002). These numerous connexins are coupled by gap junctions in the 5 major types of the neuronal layer of the retina (Söhl et al., 2005; Söhl & Willecke, 2003). Gap junctions: connexin 36, connexin 45, and connexin 57 are identified in the mouse model based on their neuron types (Söhl et al., 2005).

Each connexin consists of four transmembrane domains (M1, M2, M3 & M4), two extracellular loops (E1 & E2), and two terminal domain; amino terminus (N) and carboxyl terminus (C) **(Figure 1.9 b).** Connexins forms connexons and gap junctions' channels of different types. When gap junctions occur between two same kinds of a cell then it is known as homologous gap junctions. Whereas the gap junction's formation between different cell types is known as heterologous gap junctions. Similarly, when gap junctions occur between hemichannels of the same connexins are called homotypic channels and when hemichannels of different connexins form results in heterotypic channels (Goodenough & Paul, 2003).

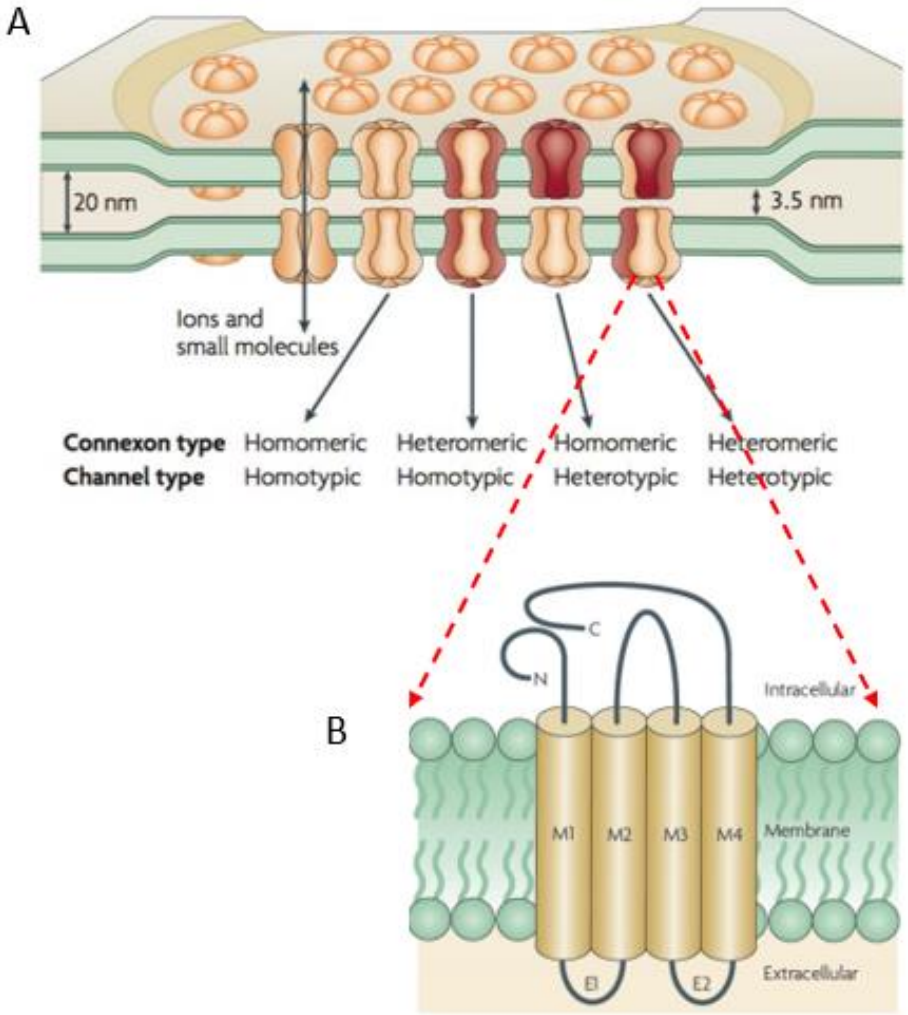

Figure 1.9 Showing the illustration of the structural and molecular organization of gap junctions. E1 and E2: Extracellular loops, M1-M4: Transmembrane domain, C and N: Terminal domain. (A) Gap junctions between two membranes. (B) Connexin subunits. Modified from (Bloomfield & Volgyi, 2009)

1.1.3.1 Functions of gap junctions in the retina

Gap junctions play a pivotal role in signal transmissions such as noise reduction, signal averaging, neuronal synchrony, and electrical coupling (Deans et al., 2001; DeVries, Qi, Smith, Makous, & Sterling, 2002). The coupling of neurons formed by gap junctions is of high plasticity. Gap junctions are a common pathway for intercellular communication to the central nervous systems (Bloomfield & Volgyi, 2009). There is a total of 7 different types of electrical coupling of gap junction occurs in the neurons of the retinal circuitry **(figure 1.10).**

The connexin36 gap junction plaques are present between the electrical coupling of the cone-cone junction and rod-cone junction (red circles) **(figure 1.10)**, but there is no evidence of any other connexin protein in the rod-cone coupling junction rod side (Feigenspan et al., 2004; Lee et al., 2003; Béla Völgyi, Michael R. Deans, David L. Paul, & Stewart A. Bloomfield, 2004). The yellow rectangle shows the other Cx36 gap junction between the electrical coupling of the (GC-GC, GC-AC, AII-AII, AII-CB; yellow rectangle) **(figure 1.10)**. The type of connexin protein expression in the rod-rod junction is still unknown (Bloomfield & Volgyi, 2009).

The horizontal cells are extensively coupled and two types of connexin expression take place, in mammals connexin50 at axon less horizontal cells and connexin 57 at the dendrites of axon bearing horizontal cells in the rabbit retina (Hombach et al., 2004; O'Brien et al., 2006; Shelley et al., 2006).

In AII amacrine cells the gap junction form two major types, the gap junction coupling between AII-AII amacrine cells form as the homotypic coupling consists of Connexin36 whereas the coupling between AII amacrine cells and the cone bipolar cells form the heterotypic coupling and AII with other amacrine cells form homotypic and bot the junction coupling consists of connexin36 and

Cx45(Deans, Volgyi, Goodenough, Bloomfield, & Paul, 2002; Dedek et al., 2006; Feigenspan et al., 2001; Mills, O'Brien, Li, O'Brien, & Massey, 2001).

The ganglion cells are extensively coupled with the other neighbouring ganglion cells and with amacrine cells. In the mouse retina, connexin36 mainly forms gap junctions with ON and OFF RGCs and ACs (Timm Schubert et al., 2005; Schubert, Maxeiner, Kruger, Willecke, & Weiler, 2005; Völgyi, Abrams, Paul, & Bloomfield, 2005).

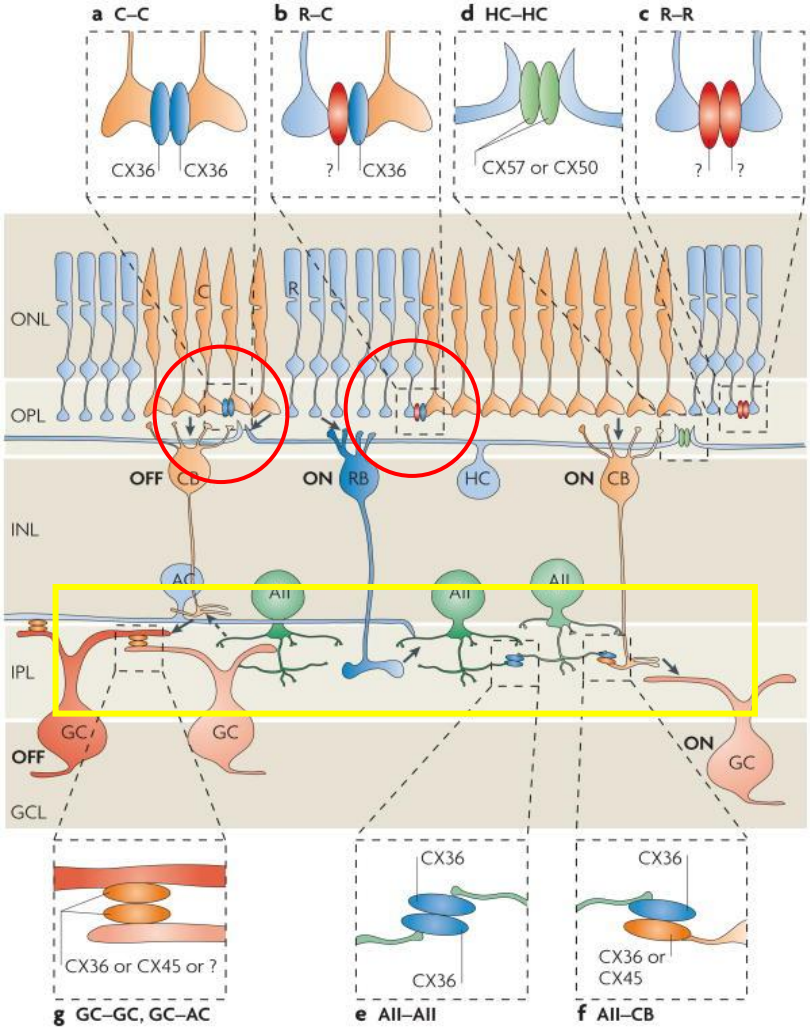

Figure 1.10 Summary of gap junctions expressed by retinal neurons (Bloomfield & Volgyi, 2009) (modified from Bloomfield and Volgyi)

1.1.4 Neurotransmitters in the Retina.

The chemical neurotransmitter releases from the synaptic contacts of retinal neurons are responsible for the processing of the visual information (Pourcho, 1996). There are several neurotransmitters in the retinal neurons classified into excitatory and inhibitory type. Previous studies on biochemical analysis have demonstrated that all the neurotransmitters found in the brain are also present in the retina (Pourcho, 1996).

The excitatory neurotransmitter has excitatory effects on the neurons so that it can fire the action potential such as Glutamate, Acetylcholine, Dopamine, and Histamine. The inhibitory neurotransmitters have an inhibiting effect on the neurons such as GABA gamma-aminobutyric acid, Glycine, and serotonin. Dopamine has both excitatory and inhibitory effects on the neurons depended on the receptor types and dopamine subtypes. In this study, we have focused mainly on Dopamine's two subtypes and their receptors application by agonists and antagonists. Dopamine has a modulatory effect on refractive and visual development and plays a very significant role in myopia development.

1.1.4.1 Role of Dopamine and its receptors.

Dopamine has been proposed to be a "stop signal" for myopic eye growth (Zhou et al., 2017). It is well known from several studies that dopamine can be a potential therapeutic target for myopia however the exact mechanism of action and contribution in the retinal pathways has remained elusive.

Dopamine is an important neurotransmitter and its signaling can modulate the exact retinal pathways to improve visual performances (Zhou et al., 2017). Dopamine releases from dopaminergic amacrine cells which regulate the light-adaptive retinal process (Doyle, McIvor, & Menaker, 2002).

Dopamine D1 and D2 receptors types are present on the neurons of the inner and outer retina (Lasater & Dowling, 1985).

Both D1 and D2 receptors are found in RGCs and had different effects on the gap junctions between the amacrine cells and ganglion cells (Mills. et al., 2001). D1 receptors act upon the gap junction of amacrine cells whereas the D2 receptor has effects on the ganglion cells gap junction.

Dopamine affects both the homologous and heterologous gap junctions coupling by decreasing the coupling between the cells. Dopamine affects the coupling between AII-AII ACs via cAMP whereas the gas transmitter nitric oxide affects the coupling between AIIACs and the ON CBP cells.

The D1 receptor might be responsible for axial length elongation and possibly contribute to myopia development (Huang et al., 2018). Several studies have hypothesized that the dopaminergic system is responsible for the development of myopia in children, but the mechanism remains unclear (Gao et al., 2006; Nebbioso, Plateroti, Pucci, & Pescosolido, 2014; Schmid & Wildsoet, 2004).

1.1.5 Visual Feedbacks: Optical defocus, Axial length, and Myopia

Ocular growth and visual processing are regulated by the retina (Fischer, McGuire, Schaeffel, & Stell, 1999). Defocus is known to be the first step in inducing myopia resulting in axial elongation and ocular structures expansion and thus altering eye growth (Bowrey et al., 2017; Pan, 2019). Abnormal visual stimuli to the retina cause changes to the overall ocular growth modulation resulting in myopia development. It is important to understand the underline mechanisms of the retina that controls the

growth of the eye and to identify the potential growth-regulating cells in the retinal circuitry that participate in this process.

During eye growth, defocus influences the transcription of the ZENK protein, which is suggested to result in myopia (Bitzer & Schaeffel, 2002; Lan, Yang, Feldkaemper, & Schaeffel, 2016). ZENK, also known as egr-1, is an immediate-early gene responsible for the acceleration of axial growth, acting bi-directionally (Ashby, Zeng, Leotta, Tse, & McFadden, 2014; Schippert, Burkhardt, Feldkaemper, & Schaeffel, 2007).

The retina can sense both focused and defocused images and delivers retinal signals to control eye growth during refractive development of the eye (Norton, 1999; Schaeffel, 2010). A study on marmosets revealed that the retina can quickly differentiate between myopic and hyperopic defocus and can affect different sets of gene expressions and retinal signaling pathways (Tkatchenko, Troilo, Benavente-Perez, & Tkatchenko, 2018).

The effects defocus may have on retinal ganglion cells signaling during the process of refractive error development and emmetropization; is still unknown. It is important to record the visual stimulus responses from the retinal ganglion cell population to investigate how the retina encodes visual scenes and delivers this information to the brain (Ghahari, Kumar, & Badea, 2018).

Studies on animal models have demonstrated the visual feedback mechanism in eye growth control and provided major evidence that defocused images can affect eye growth, consequently changing the refractive status of the eye (Banerjee, Wang, So, & Pan, 2020; Pan, 2019). The study reported that myopia development may be influenced by responses from subsets of retinal ganglion cells (RGCs) as feedback from focused and defocused images; thus, contribute to the modulation of ocular growth and refraction (Pan, 2019).

1.1.6 Retinal Ganglion cells and Myopia

Visual processing begins in the retina (Masland, 2012). The visual information is transferred from photoreceptors via interneurons to the Retinal ganglion cells (RGCs) in the retina. Axons of RGCs then travel through the optic nerve and sending the information to the brain about the visual world. Previous studies have already shown that most RGCs are not simply light detectors but also feature detectors, which helps in sending processed information about much fascinating and interesting visual world on to the central nervous system. Movement, color, fine detail, and contrast are represented by different classes of ganglion cells (Heinz Wässle, 2004).

Studies have demonstrated that myopia can cause a decrease in GC density and thinning of the retinal nerve fibre layer (RNFL) (Chui, Yap, & Chan, 2002). RGCs with their different types and distinct visual-feature helps in delivering highly processed visual information to the visual centres (Sanes & Masland, 2015). However, the mechanisms of these specified RGCs remain largely unknown (Muzyka, Brooks, & Badea, 2018).

During refractive development, while the retina senses defocus (Schaeffel & Wildsoet, 2013), these distinctive retinal signals are eventually used to mediate the retinal-scleral signaling pathway (Park et al., 2013; Stone, Pardue, Iuvone, & Khurana, 2013), eventually leading to refractive error changes such as myopia. Therefore, to better understand the mechanism of myopia, it is important to consider how the underlying firing RGC pattern is affected during the early development of myopia where defocused images are projected. To date, the exact effects of defocused images on RGCs' firing patterns remain unknown.

1.1.7 Role of Dopamine Receptors in Myopia Development

Dopamine released from dopaminergic neurons plays a key role in visual processing, synaptic transmission, and light adaptation (Zhang, Zhou, & McMahon, 2007). Its signaling can modulate the exact retinal pathways to improve visual performances (Legros, Botteri, & Vernier, 1999; Zhou et al., 2017). Dopamine performs its function through two major types of receptors: Receptors D1 and D2. Dopamine D1 receptors are found in horizontal cells (HCs), amacrine cells (ACs), bipolar cells (BCs), and RGCs (Farshi, Fyk-Kolodziej, Krolewski, Walker, & Ichinose, 2016; Mazade, Flood, & Eggers, 2019) while D2 receptors are found in photoreceptor cells, ACs and RGCs (Nguyen-Legros et al., 1999; Tian, Xu, & Wang, 2015). Previous studies have shown that dopamine is associated with myopia where D1 receptors play a key role in myopia development by modulating eye growth in mouse retina (Huang et al., 2018; Nebbioso et al., 2014; Zhou et al., 2017). Therefore, we aim to examine the effects dopamine signaling has on the firing pattern of RGCs in the focus and defocus image detection.

1.1.8 Role of Gap junction in Myopia

Gap junctions in the retina are highly plastic and help in the configuration of transmission and processing of visual inputs (O'Brien & Bloomfield, 2018; O'Brien., 2014). Defocused images were projected onto the retina to mimic myopia and observe their effect on signal transmission (Pan, 2019). The change in the signaling of ON and OFF RGCs and ON-OFF RGCs is believed to be the basis of visual information in the mouse retina because ON and OFF responses are the major component of the visual system encoded by RGCs (Asari & Meister, 2012; Gjorgjieva, Sompolinsky, & Meister, 2014). Defocus is known to be the first step in inducing myopia resulting in axial elongation and altering the eye growth which is largely governed by the retina (Maiello, Walker, Bex, & Vera-Diaz,

2017). To alter eye growth, the retinal signals, need to reach the sclera. ACs are the interneurons synapses with RGCs, which possibly further mediate the retinal signals to the sclera. In AII ACs, the gap junctions coupling is highly plasticity and modulated through phosphorylation at Ser293in the mammalian retina (Kothmann et al., 2009; Kothmann et al., 2012; Meyer et al., 2014). It is also unclear, whether gap junction expression and the AII ACs coupling are altered in the myopic retina.

Dopamine affects the Cx36 gap junction coupling in AII ACs by activating protein kinase α (PKA) (Kothmann et al., 2009). As we know dopamine regulates the process of myopia development (Huang et al., 2018; Zhou et al., 2017). However, their effects on specific cell types and neurotransmitters in myopia remain elusive. To test this hypothesis, we evaluated the expression of Cx36, which is predominantly expressed in AII amacrine cells (AII ACs).

Ser293-P antibodies were used to visualize phosphorylated connexin36 which is previously used in mice (Ivanova, Yee, & Sagdullaev, 2015), rabbits (Kothmann et al., 2009; Kothmann et al., 2012), and perch retinas (Kothmann, Li, Burr, & O'Brien, 2007). Ser293-P expression in the inner plexiform layer (IPL) of WT mouse which contains AII ACs processes were previously reported (Ivanova et al., 2015). AII ACs are coupled with Cx36 gap junctions, these gap junctions are present in the IPL which is further differentiated into 5 strata. The Localizations of Cx36 gap junctions are illustrated in our published study (Banerjee, Wang, Zhao, et al., 2020), shown in **figure 1.11(A-H)**.

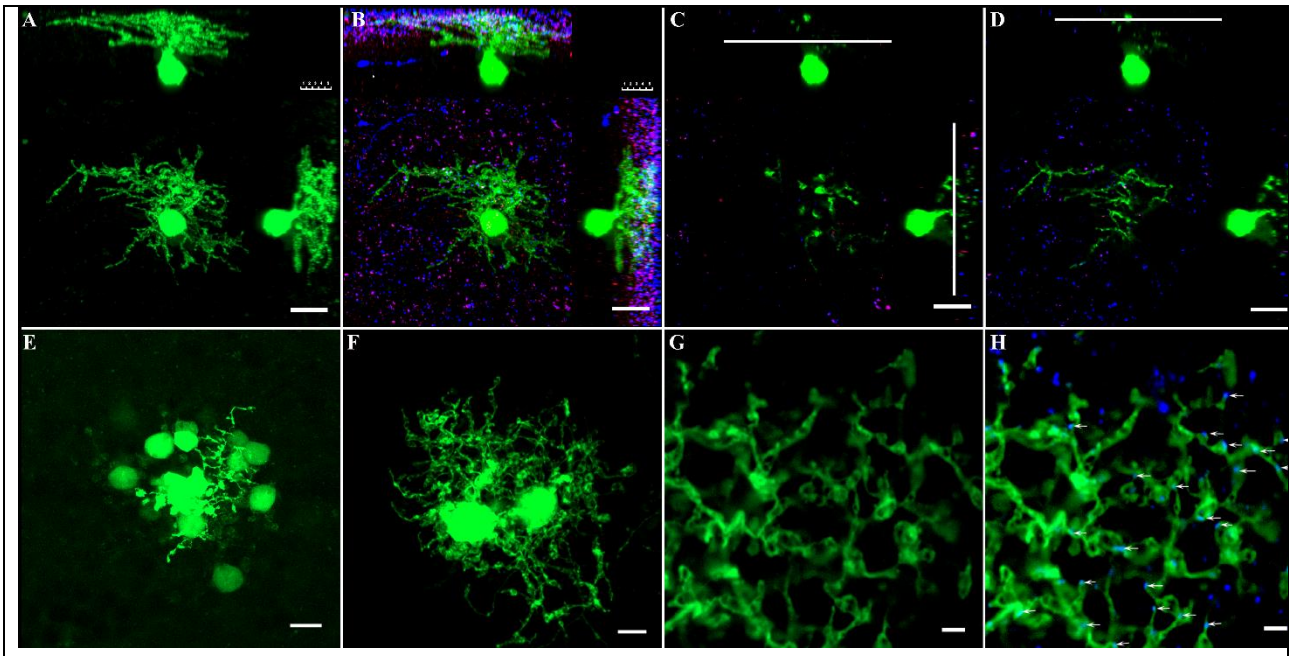

Figure 1.11 showing AII ACs in mouse retina and their colocalization with Cx36. (A) GFP labeling of single AII AC in Fam81a mice to be visualized by Neurobiotin injection. (B) Double labeling of AII ACs with Cx36 & 293-P antibodies. (C) Single-layer of AII AC in the lobular layer. (D) Single-layer of AII AC in arboreal dendrite layer. (E) Coupled AII ACs labeled with Neurobiotin injection. (F) Dendritic gap junctional coupling in AII ACs, two neighbouring AII ACs were injected with Neurobiotin. (G) Dendrites between the two neighbouring AII ACs were injected with Neurobiotin in the S5layer. (H) The homologous gap junction between AII ACs located in the S5 layer of the IPL, labeled with monoclonal anti Cx36/35(blue). Scale bar: A-D: (10µm); E-F: (5µm); G-H: (2µm) (Banerjee, Wang, Zhao, et al., 2020).

1.2 Multi-electrode Array

Multielectrode Arrays (MEAs) recognized as a useful technique in retina research (Meister, Pine, & Baylor, 1994), as it is capable of real-time recording from a large number of cell populations at a given point of time (Ghahari et al., 2018). It can simultaneously allow recordings from multiple RGCs and displaced amacrine cells(d/ACs) and directly compare spontaneously and light-evoked spiking responses from the local region of the retina (Volgyi et al., 2013).

Multielectrode arrays consist of multiple shanks and plates through which the neuronal signal is delivered. These electrodes can be used in both in-vivo and in-vitro experiments.

The first model of MEA planar electrodes consisted of 30 electrodes, arranged in two rows 100 um apart within rows and 50 µm apart between rows (Thomas, Springer, Loeb, Berwald-Netter, & Okun, 1972). However, recording of cell response was not successful, possibly due to the low extracellular of the materials used. An ideal MEA should have good electrical properties, transparency, biocompatibility, and low cost (Liu et al., 2012).

The MEA electrophysiological recordings are more efficient than patch-clamp methods (Miccoli et al., 2019), as patch-clamp is difficult to perform for long term measurements of the neuronal network compared to MEA (Maccione et al., 2015; Obien, Deligkaris, Bullmann, Bakkum, & Frey, 2014).

The parallel recording of the retinal signals with different visual stimuli has become achievable in MEA (Reinhard et al., 2014).

Modern MEAs consist of thousands of electrodes that can measure many neurons simultaneously (Segev, Goodhouse, Puchalla, & Berry, 2004; Pan, 2016) allowing signaling of ON and OFF ganglion cells to be recorded together and covers almost the whole retina. Advantageously, the cells with a wide range of physiological activities in terms of Transient/Sustained components and further separate mouse RGC can be categorized based on their ON/OFF and Sustained /Transient response. However, there may be a limitation to this as it becomes difficult to separate the response from different cells due to interference in response.

1.3 Research Question and Hypothesis.

Although there are enough shreds of evidence that image blur or defocused images alter eye growth and refraction and that the retina in large part governs refractive development. However, the comprehensive understanding of the signaling pathways that account either for emmetropization or refractive errors has remained indefinable, and clinically acceptable therapies that prevent myopia onset are not now available, which is the potential research gap we wanted to address in our study. **Therefore, the research rationale is based on the hypothesis, is that defocused, or blur images affect the retinal ganglion cells (RGCs) signaling and firing patterns in the mouse retina.**

Also, gap junctions are the key players for the signal transmission from the neurons to the higher centres. They are highly plastic and helps in the modulations of the transmission of the signals in visual development. In myopia, the eye growth alters, and we know that alteration of eye growth needs the retinal signals to reach the sclera. However, the roles of gap junction's expression and alteration of coupling in myopic retina remain unanswered. Connexin 36 (CX36) is a gap junctional protein, expressed in the gap junctions between the AII -AIIACs and largely participate in the retinal circuit pathway. **Therefore, we hypothesized that Cx36 phosphorylation increased in AII ACs in the myopic retina.**

1.4 Aims and objectives

Based on the hypotheses and research gaps, the following objectives have been defined.

1. To determine the effects of defocused light or images on RGCs signaling in the mouse retina.
2. To identify the biophysical properties of RGCs in the myopic retina including the spatial firing location pattern of RGCs and the latency of spikes firing.
3. To investigate functional gap junction coupling between AII amacrine cells (AII ACs) in the myopic mouse retina.
4. To determine how dopamine and its receptors effects of Cx36 of AII amacrine cells (AII ACs) in the myopic mouse retina.

CHAPTER 2 Methodology

2.1 Ethics Approval

All animal procedures, including rearing, handling, and tissue extraction in the experiments were approved by the Animal Subject Ethics Sub-Committee (ASESC) of the Hong Kong Polytechnic University in compliance with the guidelines for the care and use of Laboratory Animals published by the National Institute of Health.

2.2 Animal Preparation

The mouse was used as our animal model in all the following experiments as detailed below.

The study population comprised of adult (postnatal day 14–56) C57BL/6J (RRID: IMSR_JAX:000664) wild-type (WT), n=230 and Cx36 $^{-/-}$ knockout mice (RRID: MGI: 3810172), n= 4, from David Paul's laboratory, Harvard Medical School, kindly provided as a gift from Prof. Samuel M. Wu, Baylor College of Medicine. Animals were maintained in a 12 h–12 h day-night cycle, and all experiments were performed during daylight hours. The list of animals used in the overall study are shown below in **Table 2.1.**

Table 2-1 List of animals used in the experiments

S.no	Section	Number	Type	Postnatal day
1	3.1	C57BL/6J	70	14
2	3.2	C57BL/6J	43	42-56
3	3.3	C57BL/6J	5	56-70
4	3.4	C57BL/6J	75	42-56
5	3.5	C57BL/6J	10	56
6	3.61	C57BL/6J + Cx36 KO	5 +4	56
7	3.62	C57BL/6J	16	56-60

The mice underwent deep anesthesia using an intraperitoneal injection technique of ketamine (Vedno, St. Joseph, MO, USA) and xylazine (Akron, Decatur, IL, USA) [80 and 10 mg/kg (body weight), respectively], and Lidocaine hydrochloride (20 mg/ml, Sigma-Aldrich, St. Louis, MO, USA) was applied locally to the eyelids and surrounding tissue to alleviate local stimulation and pain to the mice. The animals were sacrificed by deeply anesthetizing the animals followed by cervical dislocation immediately after enucleations. Tissues were collected for further analysis.

2.3 Experimental Myopia Model: Form deprivation by lid suture method

Form deprivation is achieved by suturing the lids of the mice eye. 7˚nylon nonabsorbable sutures, black monofilament (A.C. S®, Alcon® Surgical, TX, USA) were used to suture the right eye (OD) of the mice on day 14 after birth. To minimize pain, the mice were anesthetized deeply as previously described under section 2.2.

Left eyes (OS) were not sutured and served as controls. Mice were maintained in groups of 15. The duration of suture was as follows: 28 days (n =5); 42 days (n =5) and 56 days (n =5). Treatment was terminated at post-natal times of 28, 42, and 56 days, respectively.

2.4 Refraction Measurement in Mouse Model

To evaluate changes in refractive error, ocular components such as photorefraction crescent, axial length, and streak retinoscopy were performed as described below.

2.4.1 Infrared (IR) Photorefraction

Infrared Photorefraction **(figure 2.1)** is useful in allowing measurements of the refractive status in very small eyes (Schaeffel, Farkas, & Howland, 1987). The application and function of infrared photorefraction were first introduced by Schaeffel and Howland (Howland, 1985; Schaeffel et al., 1987). IR photorefraction is a remote measurement technique that is suitable for any species with the subjects unaware of the measurement while it is done. The technique has been used immensely in previous studies for the measurement of refractive error in mice (Barathi et al., 2008; Schaeffel, Burkhardt, Howland, & Williams, 2004).

The mouse post-dilation refractive status and pupil size of each eye were measured using the IR photo refraction technique, calibrated according to published procedures (Schaeffel, 2008). The mouse was placed for measurements before the Infrared Photorefractor, Refractor DMK21AU04 (Mouse photorefraction, version April 3, 2017, camera DMK21AU04) with camera driver version 2.8.9, so that the first Purkinje image was focused on the center of the pupil. The camera can be adjusted accordingly with a custom-made holder as shown in **figure 2.1.** Measurements were randomized between both eyes of each mouse.

Figure 2.1 Eccentric infrared (IR) Photorefraction, lens, focal length extender, and 2.5 mm extension ring arrangement.

A platform set-up positioned 70 cm away from the camera was devised to align the eyes with the camera. This customized setting was needed to ensure a sharp image capture, which is not too far from the direction of the gaze and the optical axis of the eye. To customize this platform for mouse eyes, an initial calibration was done by putting a small object on top of the platform to test the mouse-camera orientation for image sharpness adjustments. After this was achieved, it was important not to change the focus settings. The mouse was then placed on top of the platform and restrained by holding their neck (Figure 2.2). If necessary, light doses of intraperitoneal anaesthesia to alleviate stimulation were carefully applied according to their body weight. Measurements obtained under local anaesthesia allowed for more consistency in refractive error data measurements.

Figure 2.2 Restrain the mice by holding the neck gently while performing refraction.

Once the set-up alignment was achieved, the connected computer screen displayed the identified mouse eye using the dmk refractive software program, illustrated in **(figure 2.3).**

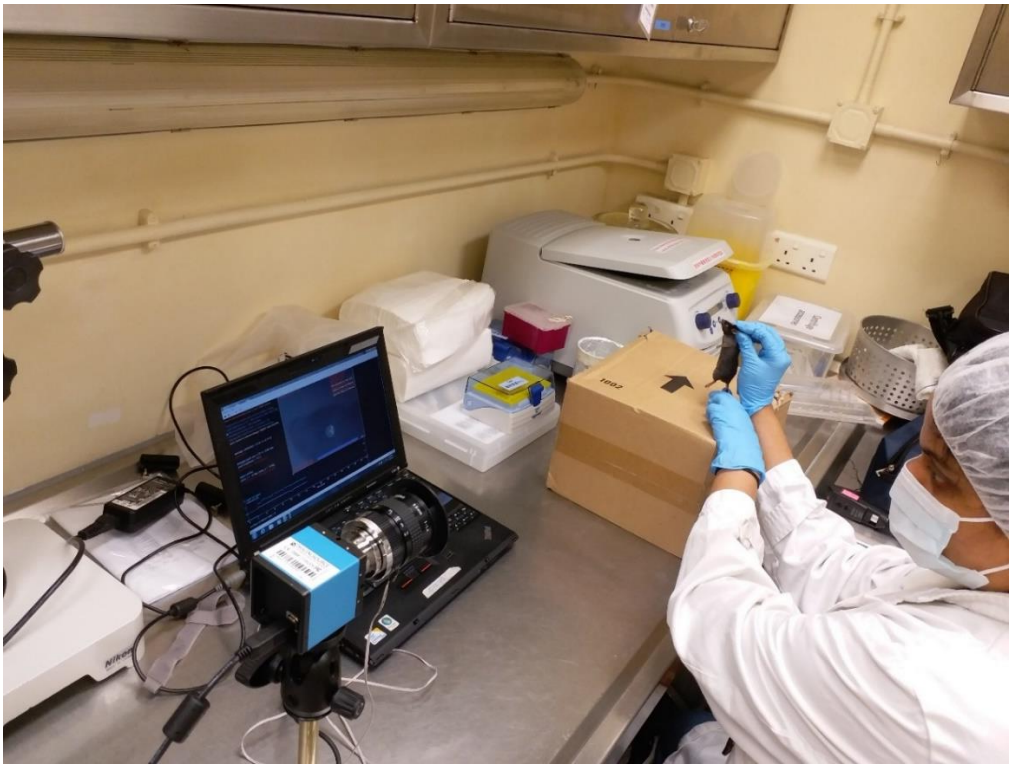

Figure 2.3 screen example from the dmk refractor software while measuring the refraction in the mouse eye.

The direction of gaze must first be detected, and the image acquired for refraction analysis must be close to the optical axis of the mouse eye during each recording. The refractive error was calculated by the accompanying software after positions of the first Purkinje image was detected with adequate brightness across the pupil. Ten consecutive measurements were acquired simultaneously to generate an averaged refractive error reading within 90 seconds. All refraction data readings were stored within the software file.

2.4.2 Streak Retinoscopy Refraction

Previous studies have mentioned that it is possible to measure the refractive status of the mouse eye using the streak retinoscopy technique (Barathi et al., 2008; Pardue., Stone, & Iuvone, 2013). We wanted to compare the results of streak retinoscopy with IR photorefraction. Particularly for higher hyperope, the streak reflex becomes very small, making it difficult to obtain an accurate value (Pardue. et al., 2013). Cycloplegic retinoscopy using streak retinoscope (Heine, Beta 200 Steak Retinoscope Set 2.5V) (figure 2.4) was performed under dim illumination. Topical cycloplegic eye drop (Mydrin-P Ophthalmic solution, Santen, Osaka, Japan) was used to cycloplege and dilate the pupils. Mice were anesthetized with 0.08–0.1 ml (IP) of a mixture of 0.2 ml 10% ketamine hydrochloride (Vedno, St. Joseph, MO, USA) and 0.1 ml 2% xylazine hydrochloride (Akron, Decatur, IL, USA), dissolved in 1.0 ml mouse ringer solution. Retinoscopy was performed at a distance of 33cm, similar to published work by- (Barathi et al., 2008; Tejedor & de la Villa, 2003), which accounted for a working lens distance of +1.50D (computed as the reciprocal of working distance in meters). A lens bar (up to +/- 15.00D in 0.5D steps)(figure 2.4) was used to neutralize the two principal meridians. During the whole procedure, topical lubricating eye gel (Lacryvisc; Alcon, Fort Worth, TX, USA) was applied every 20 minutes to prevent cornea desiccation and immediately wiped out with a swab stick before performing steak retinoscopy (this did not affect measurement accuracy). A lens rack holder was placed against the corneal plane to aid in this refraction procedure. The refraction values were recorded in a notebook and then transferred to the excel entries (Microsoft Office 2016 Tools) for the data analysis. Results were recorded as a mean spherical equivalent (S.S.= Spherical power + ½ cylindrical power).

Figure 2.4 Streak retinoscope and lens rack with both plus and minus lenses.

2.4.3 Axial Length Measurement

The axial length measurement was performed by capturing images using a Spectral-Domain Optical Coherence Tomography (SD-OCT) system EnvisuTM R-Series SDOIS R-Series Spectral Domain Ophthalmic Imaging Systems; Bioptigen, Inc.; Lieca, Germany. Depth-resolved images of ocular tissue microstructures were acquired, processed, displaced, and saved for analysis. The whole mouse eye program and the mouse 50 mm telocentric lens were selected to image the following parameters: radial scan 0.8 mm 1000 A scan with 6 radial and 30 B-scan. Once a clear and focused image was obtained, the axial length was measured with built-in program calipers. To confirm a proper mouse eye alignment, the Dynamic Scan Control feature was used **(figure 2.5 B)**, where the surface of the eye was followed and light source adjustments were made for the central reflection along the vertical and horizontal optical meridians. The axial length was measured from the anterior surface of the cornea to the RPE layer/ Bruch's membrane **(Figure 2.5 C)**. The axial length measurement calipers

were calibrated assuming a refractive index of 1.38; the inbuilt standardized refractive index of the whole mouse eye in the Spectral-Domain Optical Coherence Tomography (SD-OCT) system.

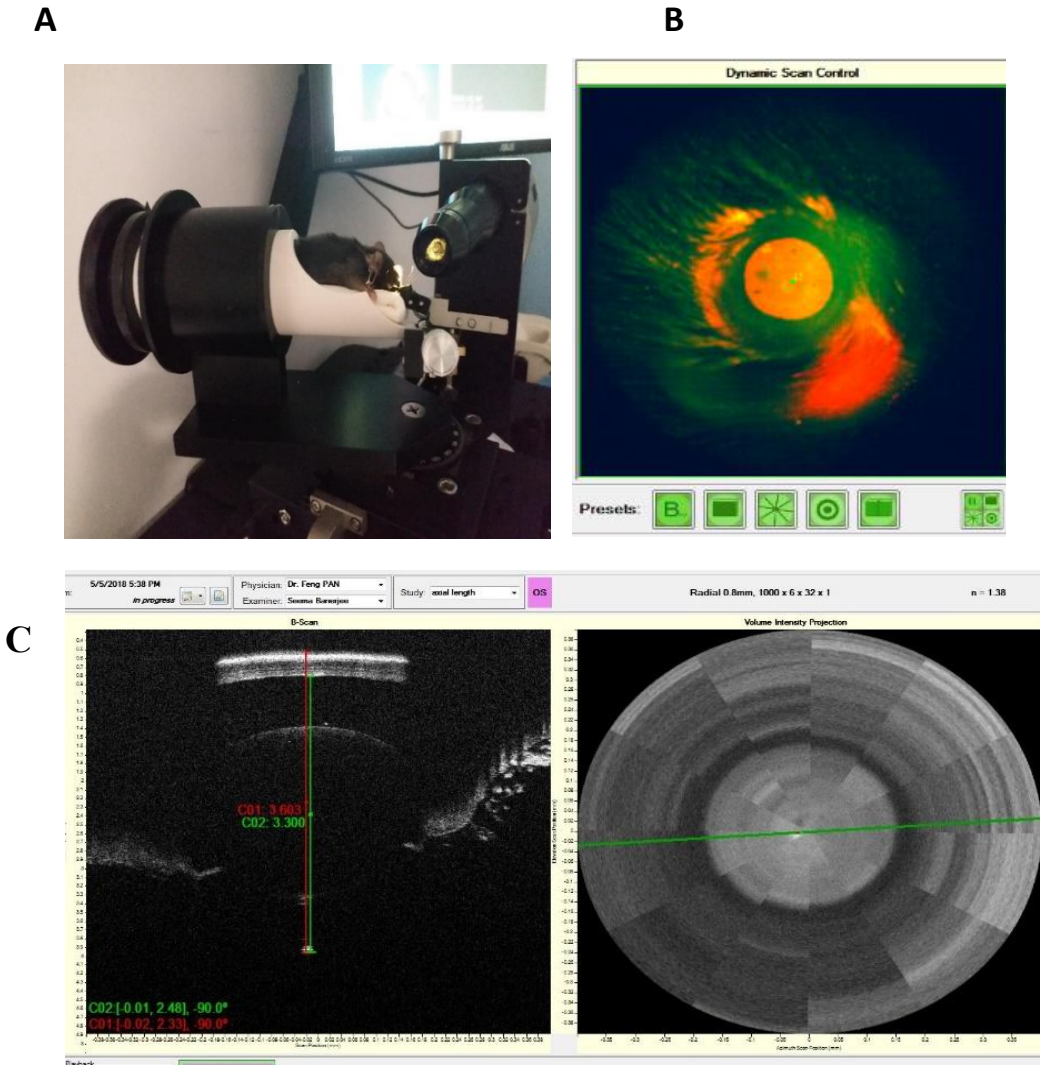

Figure 2.5 Axial length measurement procedure. (A) Aerial view of a mouse within the cassette while attached to the bite bar. (B) Dynamic scan image of the mouse eye. (C) B-scan and volume intensity projection of the mouse eye. Axial length was defined from front of the cornea to the RPE layer/Bruch's membrane.

To perform the axial length measurement of the mouse eye, animals needed to dark-adapt for at least half an hour for the pupillary muscle relaxations, which is likely to help capture good quality images and measurements. The mice were anesthetized with an IV injection of 0.05-0.06 ml of (0.1 ml of 15% ketamine hydrochloride and 0.1ml 2% xylazine hydrochloride with the 0.8ml composition of standard Mouse Ringer solution). The mouse eyes were dilated with one drop of Tropicamide-Phenylephrine Hydrochloride ophthalmic solution (Mydrin-P; Santen Pharmaceutical Co., Ltd; Japan) 15 minutes before measurement to achieve a maximum pupillary dilatation of 2.33mm. To capture better images and further improve precision, the mouse eyes were moistened with eye gel (Lacryvisc; Alcon, Fort Worth, TX, USA). During image capture, the animal kept in position by first holding in a comfortable position, then wrapping the mouse with tissue paper and placing it on the mouse cassette stage. It is important to hold the mouse nose with a bite bar for better restraint control. The system program called "EnvisuTM R-Series SDOIS" was used to analyze AL. For each mouse tested, one had to input and save the clinical details under the parameter bar as a New patient. Likewise, examiner details, date of examination, and type of program were recorded and saved under the same program. The "Mouse whole eye" configuration was selected to capture the whole eyeball. Position the 50-degree telecentric mouse lens and put the reference arm of the instrument at 695 nm **(figure 2.5 A)**. Next, select the program by Right-clicking the mouse, then select edit, for mouse axial length select radial scan, and select the saved program. Also, select the eye to measure and save it. During image capture, the telecentric mouse lens was moved as close as possible by the scale arm to the mouse eye until a clear image was observed by the scale arm. Two sponge buds, which were soaked with (Refresh plus lubricating eye drop; Allergan, Irvine, CA, 92612) were used to remove the eye gel from the mouse eye. For correct imaging, the angle between the mouse eye and the lens was maintained at 45 degrees to be matched with the reference line of the OCT while capturing the image and also help in maintaining the proper alignment. Images were captured using the Snapshot button on the screen.

2.5 Electrophysiological Recording

2.5.1 Multielectrode Arrays

Extracellular recording of the RGCs from all quadrants of the retina were obtained using Multielectrode Arrays (MEAs), which allowed simultaneous recordings of up to 252 neuronal retinal cells (figure 2.6). Retina–eyecups were isolated, mounted on filter paper (8μmpore size; Millipore). The RGCs were placed side down on MEA 256 channel grid system (Multichannel systems Gmbh, Reutilingen, Germany) as shown in **Figures 2.6 & 2.7.**

The electrodes were arranged in a 16 × 16 grid with, 256 MEA electrodes used over an electrode spacing of 200/100 μm and a diameter of 30 μm (256MEA200/30iR-ITO or 256MEA100/30iR-ITO, see **Figure 2.6**). The retina was covered over a 27.76–12.11 mm^2 area. The bathing temperature in MEA was maintained at 31–33°C by heating the bottom of the recording chamber and the inflowing solution. Retinal tissue was placed on the array for at least 15 to 20 minutes before recording because the contact between the electrode and the retinal tissue needed time to generate the spike and amplitude of the recorded spikes, which -usually improved during this period.

During the experiment, all data were recorded simultaneously and stored for off-line analysis. Spike trains were recorded digitally at a sampling rate of 20 kHz with the MC Rack software (Multichannel Systems Gmbh, Reutilingen, Germany). For additional off-line analysis, Off-line Sorter (Plexon, Dallas, TX, USA) and Neuroexplorer (Nex Technologies, Littleton, MA, USA) software was used.

Spikes were sorted and time-stamped from digitized recordings using principal-component analysis (Offline Sorter; Plexon). Peri-stimulus time histograms (PSTHs) (5-ms bins) and cross-correlogram profiles (CCPs) (1-ms bins) were generated from the time-stamped spike recordings of RGC pairs using Neuroexplorer software (Nex Technologies).

The significance of correlated spikes above chance was determined as those correlations exceeding the 99% confidence intervals. To determine the percentage of correlated spikes between RGC pairs,

area under the curve measures were computed for profiles within the shift predictor CCP that exceeded the 99% confidence interval as a percentage of the entire profile in a ± 50-ms epoch (Origin; OriginLab Corporation). The number of lights evoked ON and OFF spikes of RGCs or current amplitudes were calculated by subtraction of the background spike or current activity from those evoked by the light stimulus onset and offset, respectively.

The classification of cells as a sustained or transient type was based on spike frequency parameters as previously described (Della et al., 2013; Pan et al., 2016).

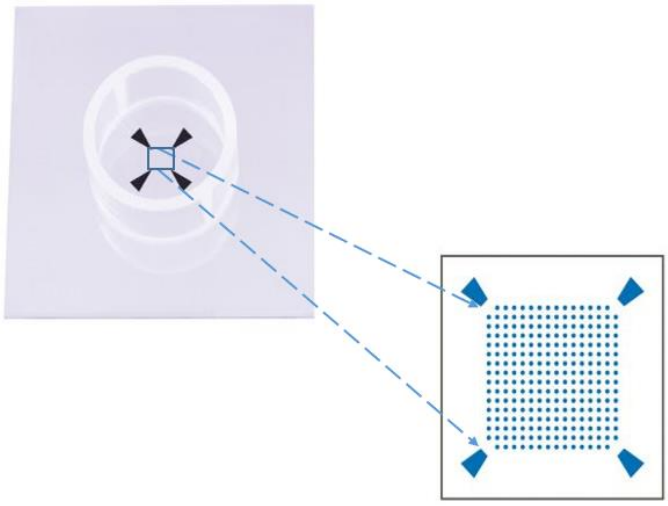

Modified from multichannel systems , 256MEA200/30-IT

Figure 2.6 showing 256 MEA 200/30-IT, glass electrode used for recording the RGC signals.

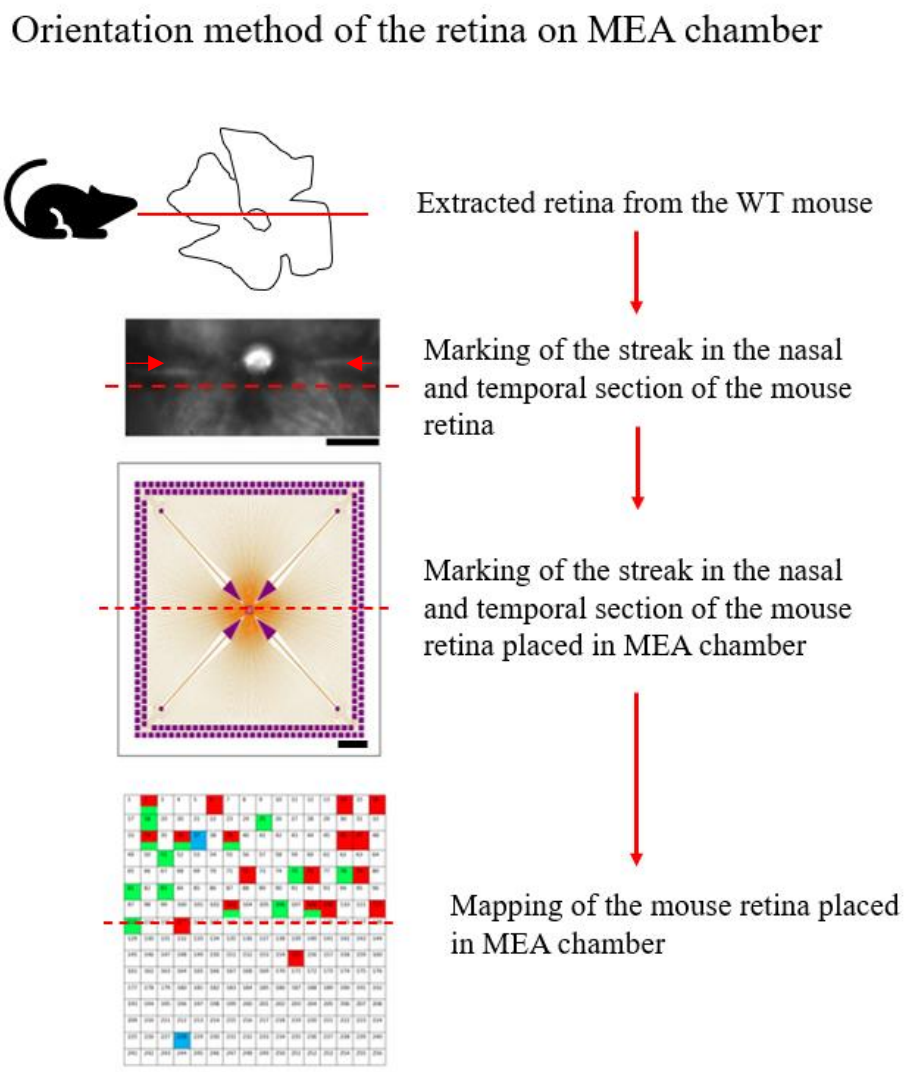

Figure 2.7 Figure showing the orientation and placing of mouse retina onto the MEA chamber and its response mapping.

2.6 Flattened Retina and Sclera Preparation

All the experiments were performed during daylight hours. The mice were anesthetized deeply with an intraperitoneal injection of ketamine (Vedno, St. Joseph, MO, USA) and xylazine (Akron, Decatur, IL, USA) [80 and 10 mg/kg (body weight), respectively], and lidocaine hydrochloride (20 mg/ml,

Sigma-Aldrich, St. Louis, MO, USA) applied locally to the eyelids and surrounding tissue. Eyes were removed under dim red-light conditions, hemisected from the anterior segment to the ora serrata. The anterior segment structure along with the vitreous was removed. The leftover whole retina-eyecup including the scleral tissue was placed in the super-fusion chamber. The retinas were dissected radially into four equal quadrants and mounted on filter paper (8μmpore size; Millipore) for flat mounting. The flattened retinas were then superfused with oxygenated mammalian Ringer solution Ph 7.4, AT 34° C (Bloomfield & Miller, 1982). The animals were sacrificed by deeply anesthetizing the animals followed by cervical dislocation immediately after enucleations.

2.7 Patterned Light Stimulation

Different patterned light stimulation approaches were used to record the signals from RGCs.

2.7.1 Full-field Light Technique

A green (525 nm) light-emitting diode delivered uniform full-field visual stimuli to the surface of the retina. The intensity of the square-wave light stimuli was calibrated with a portable radiometer/photometer and expressed in terms of the time-averaged rate of photoisomerization per rod per second (Rh*per rod s−1). Light intensities were calculated assuming an average rod density of 437,000 rods mm−2 and a quantum efficiency of 0.67. The light stimulation method used to project onto the retina is shown in **Figure 2.8.**

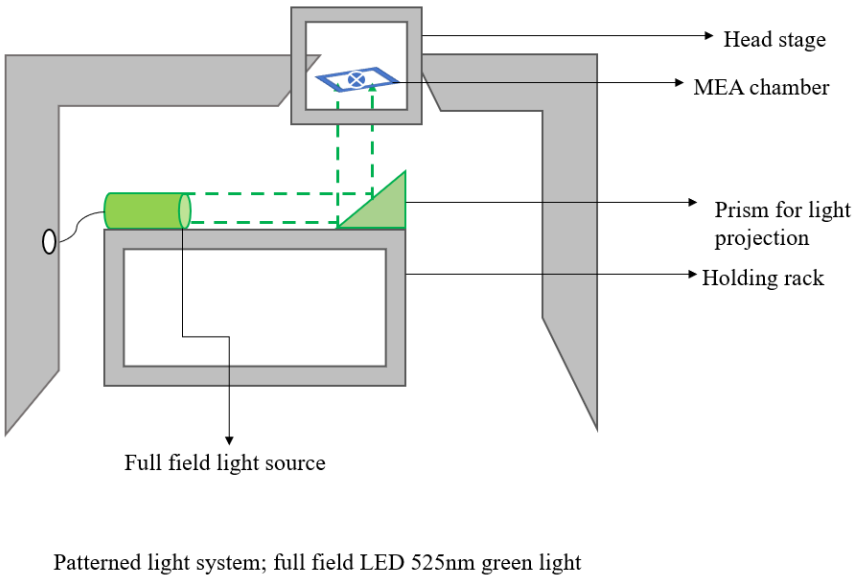

Figure 2.8 Schematic representation of the patterned light system for full-field 525 nm green light

2.7.2 OLED Light Technique

For MEA, spatial frequency stimuli were generated by PsychoPy onto the photoreceptor layer. Images emitted from a green organic light-emitting display (OLEDXL, Olightek, Kunming- China; 800 × 600-pixel resolution, 85 Hz refresh rate) were illuminated directly on to the electrode layer of an MEA chamber through the 8 mm diameter hole via custom made Badal system. OLED was mounted on the micrometers to move on the rail with plano-convex lenses via a prism to project-focused and defocused images below the electrodes of the MEA chamber, as shown in **Figure 2.9**. To ensure that the retina was stimulated by the image projected on OLED, the optical axis of the projection lens, prism, and lens on the optical rail were carefully checked before the experiment and not disturbed during the recording (Banerjee, Wang, So, et al., 2020).

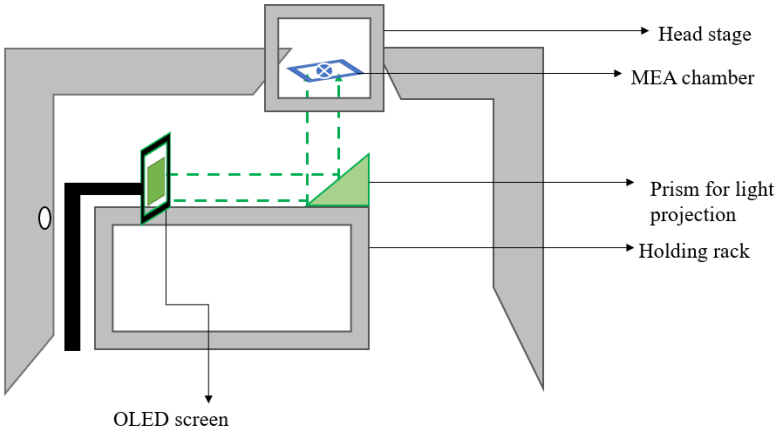

Patterned light system; OLEDXL, Olightek, China; 800 × 600-pixel resolution, 85 Hz refresh rate

Figure 2.9 Schematic representation of the patterned light system using the OLED.

2.7.3 Custom made Light Device

A custom-made light system shown in **Figure 2.10,** was designed to produce light stimulus was used to create myopic and hyperopic defocus, using light intensities of 0.001x2, 0.001x5, 0.001x 8, 0.01x 2, 0.01x 5, 0.01x 8, 0.1x 2, 0.1x 5, 0.1x 8 and 1x 2 Rh*/rods/sec. The light intensities were calculated assuming an average rod density of 4,37,000 rods mm^2 and a quantum efficiency of 0.67. The +25 D lens was moved by a micro-manipulator with steps of 5 microns to create defocus of +10 D, +20 D, -10 D, and -20D under 1x 2 light intensity.

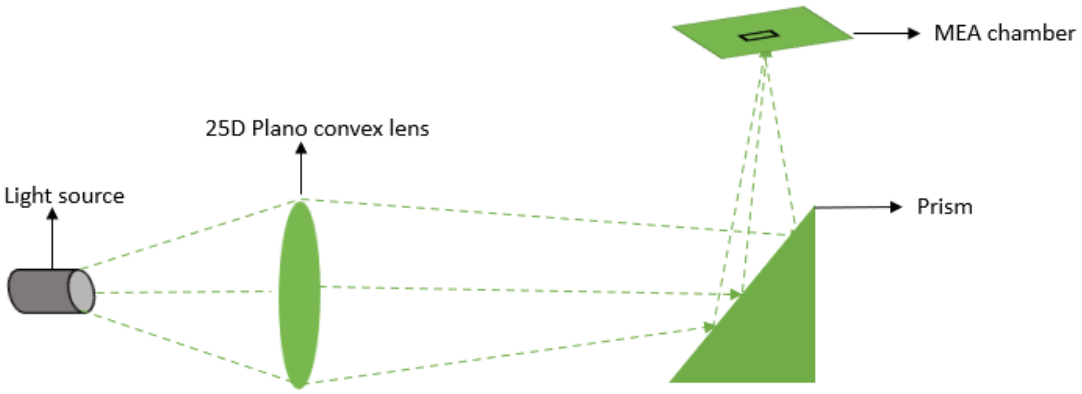

Ray diagram showing experimental design for the custom made light device.

Figure 2.10 Experimental design for the custom-made light device.

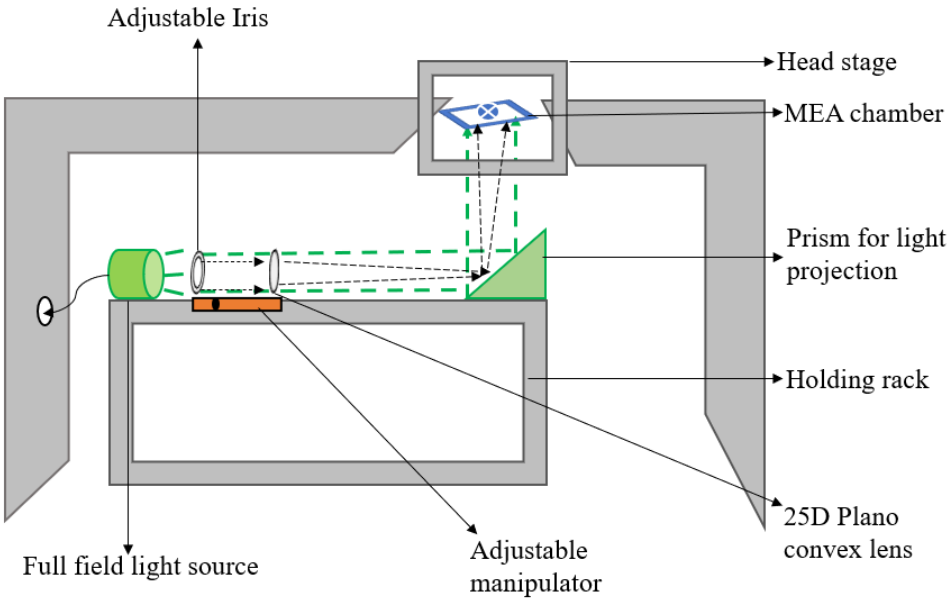

Figure 2.11 Schematic representation of the patterned light system using the LED 525 nm green light for the defocus model.

2.7.4 Patterned Light Stimulus Optical Defocus

Rigid gas-permeable (RGP) contact lens with dioptric power +/- 10 and 20 D and larger diameters was used on top of the OLED to create defocus as shown in **Figure 2.12**. Image of 5x5 dot with a spatial frequency of 0.2 cycles per degree projected for recording the stimulus-response. After 1 minute of recording with the focused image, we rerun the stimulus program and placed the RGP contact lens on top of the OLED in such a way that it should cover the whole area of image projection. The contact lens is hard and thus it is very convenient to sit stable on the OLED surface.

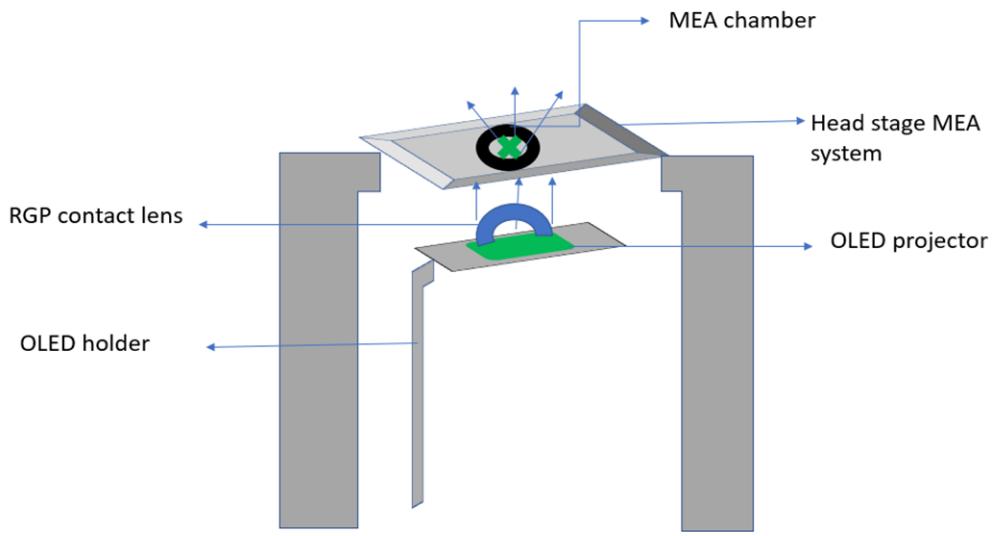

Figure 2.12 Experiment design to project the defocus image with the help of the RGP contact lens on to the mouse retina in the MEA system.

2.8 Light Stimulus Program Code

To present images via OLED to the surface of the retina, the PsychoPy software package was used in the python programming language. This program is primarily and extensively used in neuroscience and experimental psychology research (Peirce, 2007, 2009). In the first stage, 0.2 cycles per degree spatial frequency 10 × 10grid pattern square wave grating (for a clear image) and gaussian blur (for blur image) were projected. Later, only 0.2 and 0.5 cycles per degree spatial frequency 5x5 grid pattern gaussian blur were used **(Figure 2.13 A, B).**

A **B**

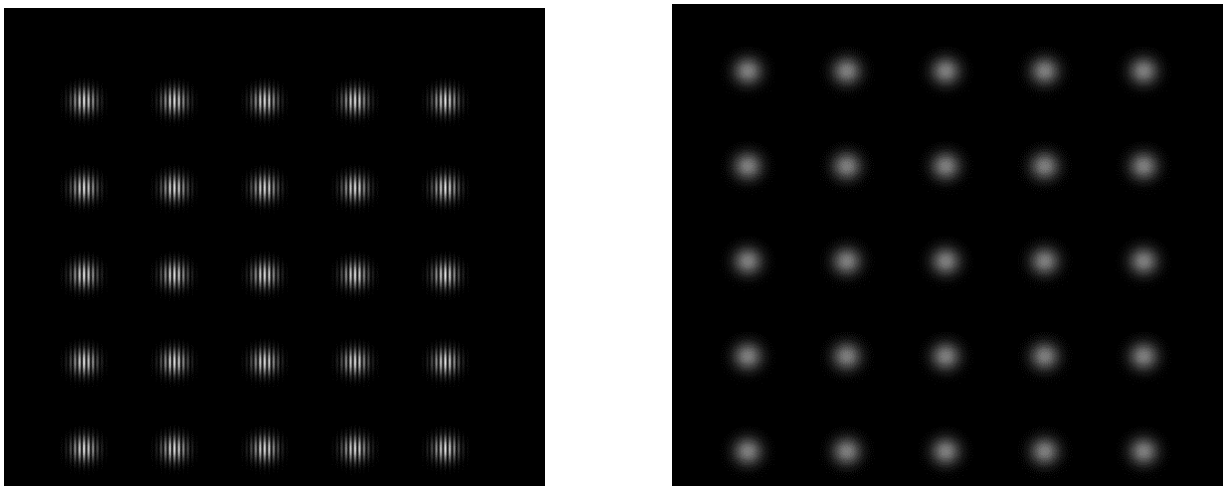

Figure 2.13 (A & B) 0.2c/d and 0.5 c/d (cycles per degree) 5×5 grid NumPy array.

2.9 Injection Neurobiotin

To reveal the morphology of ON and OFF alpha RGCs, Neurobiotin injection was performed on the GFP-labelled cells and was visualized at 40X magnification. Then the targeted interesting cells were penetrated with sharp electrode pipette tips filled with 4% Neurobiotin (Vector Laboratories, Burlingame, CA, USA) and 0.5% Lucifer yellow-CH (Molecular Probes, Eugaene, OR, USA) in double-distilled water, then backfilled with 3M LiCl. The electrode resistance was ~100 MΩ. The cell was then injected with a biphasic current (+1.0 nA, 3Hz) for 1 minute (Banerjee, Wang, So, et al., 2020).

To perform the pharmacological experiments using AII ACs, a pharmacology injection method was used with a patch-clamp, and injections were done within one minute and kept for a 10-minute

diffusion period. Pieces of the retinas were superfused for 15 minutes before commencing the injection and diffusion periods with either bubbled Ringer's solution at 35˚ C or with D1R agonist (SKF38393, [(±)-1-phenyl-2,3,4,5- tetrahydro-(1H)-3-benzazipine-7,8- diol hydrobromide],10 µM, (Tocris Bioscience, Bristol, United Kingdom) or antagonist (SCH23390, SCH [R(+)-7- chloro-8-hydroxy-3-methyl-1-phenyl-2,3,4,5- tetrahydro-1H-3-benzazipine hydrochloride] at a lower concentration of 5 µM, Sigma-Aldrich, St Louis,Mo, USA; D-054).

The experiments were performed in dim white light, around $1.27x10^3$ photon μm^{-2} s^{-1} to avoid certain changes in the gap junction's property as it can be influenced by extreme bright or dark conditions. The brighter condition can dramatically regulate the gap junctions or can be completely shut down in dark (Bloomfield & Volgyi, 2009; Bloomfield & Völgyi, 2004). Following injection, the retinal pieces were fixed in 4% paraformaldehyde for 15 minutes and then incubated overnight in 0.1M PB with 0.5% Triton-X 100 and 0.1% NaN3 containing 1% donkey serum at 4°C. After extensive washing (6 times for 1 hour), the tissues were incubated overnight at 4°C in Alexa-488 conjugated streptavidin (Invitrogen, Carlsbad, CA, USA) 1:200. The tissues were then mounted on glass slides with the help of Vectashield (Vector Laboratories) on the glass slides for observation.

2.10 Immunocytochemistry

Mouse retina, retinas were obtained from the dorsal section of the mid-peripheral retina in the nasotemporal plane as shown in **(Figure 2.14).** The retinal pieces, attached with filter paper (RGCs up), after injection and isolated from the eyecups were submersion-fixed in 4% paraformaldehyde in 0.1M PB, pH 7.5 for 30 min at room temperature. Following fixation, the retinas were detached from the filter paper and washed extensively with 0.1M phosphate buffer (PB, pH 7.4). The tissue was then blocked with 3% donkey serum in 0.1M PBS with 0.5% Triton-X 100 and 0.1% NaN_3 overnight. Table 2.2 shows the list of primary antibodies used in the study.

Table 2-2 Showing the list of primary antibodies used for immunocytochemistry.

Primary antibody	Clonality	Host	Dilution	Catalog No
Anti-acetyltransferase antibody	Polyclonal	Goat	1:500	AB144P
Anti- connexin 35/36 antibody	Monoclonal	Mouse	1:1000	MAB3045
Connexin 36 antibody	Polyclonal	Mouse	1:1000	36-4600
Ser293-P	Polyclonal	Rabbit	1:1000	Kindly provided by Dr. John O' Brien, The University of Texas

Western blotting was used to verify the monoclonal mCx35/36 and polyclonal antibody anti-Cx36 in both mouse and chicken retinas (Kothmann et al., 2007). Goat anti-ChAT (1:500, Millipore; Cat# AB144P, RRID: AB_2079751) was used for labeling the ON and OFF layers in the inner plexiform

layer in the mouse retina. Secondary antibodies used were donkey anti-rabbit, goat and mouse, Alex fluor 488 conjugate, 633, Cy3, and Cy5.

The antibodies were diluted in 0.1M PBS with 0.5% Triton-X 100 and 0.1% NaN3, containing 1% donkey serum. The tissues were incubated in primary antibodies for 3–7 days at 4°C and then, after extensive washing, were incubated in secondary antibodies overnight at 4°C. Following secondary antibody incubation, the tissues were washed with 0.1M PB and then mounted with Vectashield on glass slides for observation, previously described (Farajian, Pan, Akopian, Völgyi, & Bloomfield, 2011).

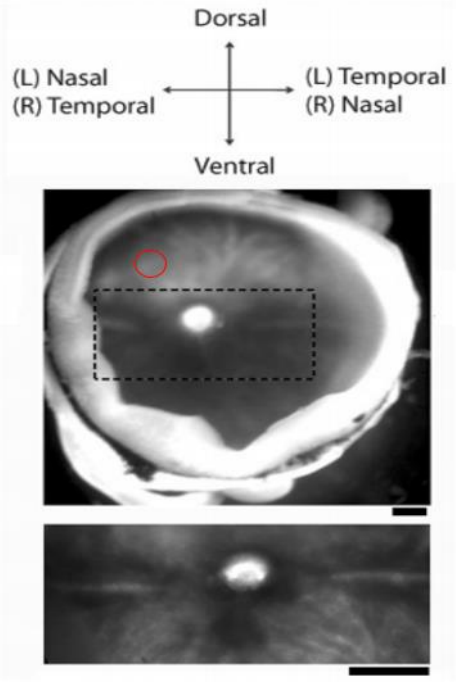

Figure 2.14 Showing the dorsal section of the retinal eye cup dissection under a microscope, modified from (Wei, Elstrott, & Feller, 2010).

2.11 Vibratome Section for Mouse Retina

After extracting the eyes from deeply anesthetized mice, the retina–eyecups were isolated, divide radially into four, and mounted on filter paper (8µmpore size; Millipore) for flat mounting. The retinas were then fixed with 4% paraformaldehyde in 0.1M PB, pH 7.5 for 1 hour. After fixation, the filter paper was removed, and the retina transferred gently to a gelatin block by facing the photoreceptors towards the gelatin block.

Additional molten 4% gelatin was gently injected on top of the fixed retina on the gelatin slice and allowed to set. For 15 to 20 minutes for complete sealing of the retina in the gelatin slice block. Extra gelatin was trimmed from the retinal block and it was attached to the black support disc of the vibratome (LEICA VT 1200S) with super glue. After setting up the vibratome, the black supporting disc was inserted together with the retinal gelatin block and attached to the vibratome instrument. A sufficient PBS solution was added to the vibratome tank to cover the gelatin block completely. Initially, 100µm continuous sections were cut until the retina was reached. Then thinner slices between 50-80 µm were produced, which were collected in a 35×10 mm tissue culture dish containing 3% donkey serum in 0.1M PB.

2.12 Pharmacology

For pharmacological experiments, different drugs were applied to the retina by adding the drug to the Ringer's solution in the MEA chamber. After adding the drug, the perfusion and waste outflow system are stopped for 70 seconds. 10 seconds for the adaptation period and the rest 60 seconds for recording. The following agents were used: D1 and D2 agonist SKF38393 and Quinripole from (Tocris); D1 and D2 antagonist SCH 23390 and Eticlopride obtained from (Sigma-Aldrich), 18β-glycyrrhetinic acid (18β-GA; Sigma) **(Figure 2.15).**

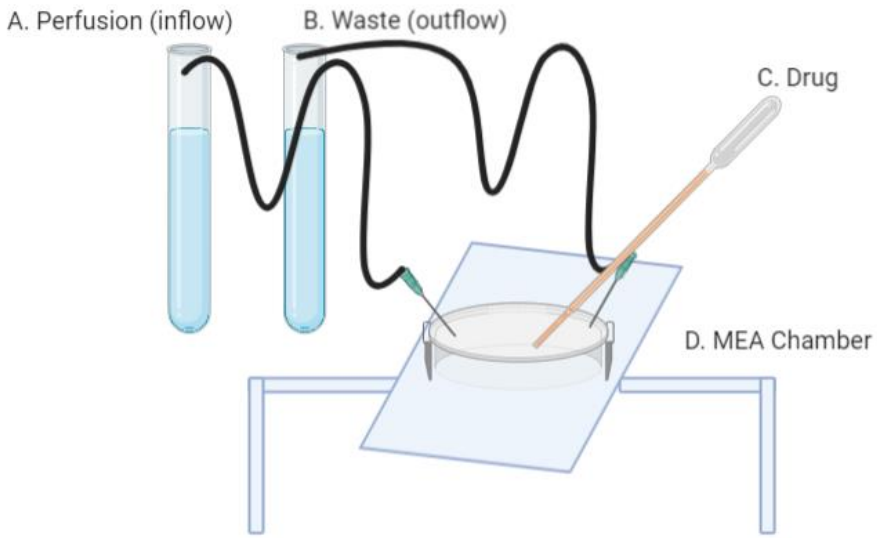

Figure 2.15 Illustrates the methodology used to deliver the drug onto the retina.

2.13 Imaging and Data Quantification

ZEISS LSM 800 with Airyscan (Zeiss, Thornwood, NY, USA) confocal microscope with a 40× and 63× objective (N.A. 0.8 and 1.4 respectively) were used to acquire images from whole-mount retinal tissue. The XY resolution of the instrument was 120 nm and 350 nm in z resolution and all three channels were superimposed. Z-axis steps were usually 0.35 µm. The size threshold was filtered by 0.01µm^2. The mice retinas were imaged under the same acquisition conditions, including laser intensity, pinhole, photomultiplier amplification, and z-stack step size. Three animals from each mouse line were analyzed. The evaluation was performed as reported previously (Ivanova et al., 2015; Kothmann et al., 2009; Kothmann et al., 2012). All four fields were analyzed for every mouse retina and the images were evaluated using Image J software (Image J, 1.52i, RRID: nif-0000-30467). The ratio of the mean intensity of Ser293-P to mCx36 immunofluorescence was estimated for each of the regions of interest (ROIs) and averaged across all ROIs in all images per condition. This way allowed, the overall phosphorylation data to be collapsed into one value per condition per animal to perform statistical analysis.

2.14 Statistical Analysis

Graph Pad Prism7 (GraphPad Software, Inc., USA) and Origin software (OriginLab, Northampton, MA, USA) were used for data analysis. All data are reported as means ± S.E.M unless otherwise specified. The notation 'n' represents the sample size included in the experiment for analysis. A statistical significance ($p \leq 0.05$) was determined using the Wilcoxon-Mann-Whitney rank-sum test paired t-test and ANOVA unless otherwise specified. The P-value notation used for statistical analysis is shown below, in **Table 2.3**.

Table 2-3 ***The P-value notation used for statistical analysis.***

Symbol	*P*-value
ns	>0.05
*	<0.05
**	<0.01
***	<0.001

Part of section 2 (Chapter 2: Methodology) is published and * Reproduced with permission:

(1). BANERJEE, S., WANG, Q., ZHAO, F., TANG, G., SO, C., TSE, D., TO, C.-H., FENG, Y., ZHOU, X. & PAN, F. 2020b. Increased Connexin36 Phosphorylation in AII Amacrine Cell Coupling of the Mouse Myopic Retina. *Frontiers in Cellular Neuroscience,* 14.

(2). BANERJEE, S., WANG, Q., SO, C. H. & PAN, F. 2020. Defocused Images Change Multineuronal Firing Patterns in the Mouse Retina. *Cells,* 9**,** 530.

3.1 Myopia Development Model.

Mouse models offer several advantages over other animals in studying refractive development (Barathi et al., 2008; Pardue. et al., 2013). Our initial sample size consisted of 100 mice and 30 were excluded from this study group due to ocular health problems such as cataracts, bleeding lids and some died during experiments. Mice with bleeding lids were not resutured back as the eyes were open and left for healing and thus excluded from the study within the first week of suturing.

The remaining mice (n=70) were divided into three groups of 20+ mice based on lid suture times: Group 1. 42-days lid suture (n=22), Group 2. 56-days lid suture (n=22), and Group-3. 70 days of lid suture (n=22). The treatment groups and the number of animals used for the measurement are summarized in Table 3.1.

Table 3-1 Mice Grouping and life-span treatment days

Groups	No. of animals	Starting age (days)	Ending age (days)	Treatment days
Lid suture 6 weeks	22	14	56	42
Lid suture 8 weeks	22	14	70	56
Lid suture 10 weeks	22	14	84	70

3.1.1 In vivo Measurement of Axial Length (AL)

The AL was examined by the SD-OCT system adjusted for mice (Fig.3.1). the system offered a high-level resolution of 2.6 μm, which was needed to detect, exact and repeatable estimations from the very small changes in AL observed in mice. (Jiang et al., 2018) The AL was measured from the first corneal surface reflex to the RPE layer.

Figure 3.1 compares the changes in the AL between sutured and control eye groups. The mean AL of the experimental eye (sutured eye at 6 weeks) was 3.398 ± 0.009 mm (±S. E.M; n=23), in contrast to 3.374 ± 0.009 mm (±S. E.M; $p \leq 0.001$, n=22) of the contralateral control eye. The (sutured eye at 8 weeks) was 3.438 ± 0.01mm (±S. E.M; n=24), in contrast to 3.400 ± 0.01mm (±S. E.M; $p \leq 0.001$, n=22) of the contralateral control eye. The (sutured eye at 10 weeks) was 3.547 ± 0.01mm (±S. E.M; n=23), in contrast to 3.492 ± 0.009 mm (±S. E.M; $p \leq 0.001$, n=22) of the contralateral control eye. Also, the average AL of the sutured eye compared between the 6, 8, and 10 weeks were found statistically significant of $p \leq 0.001$ performed with 2-way ANOVA post-hoc Tukey test.

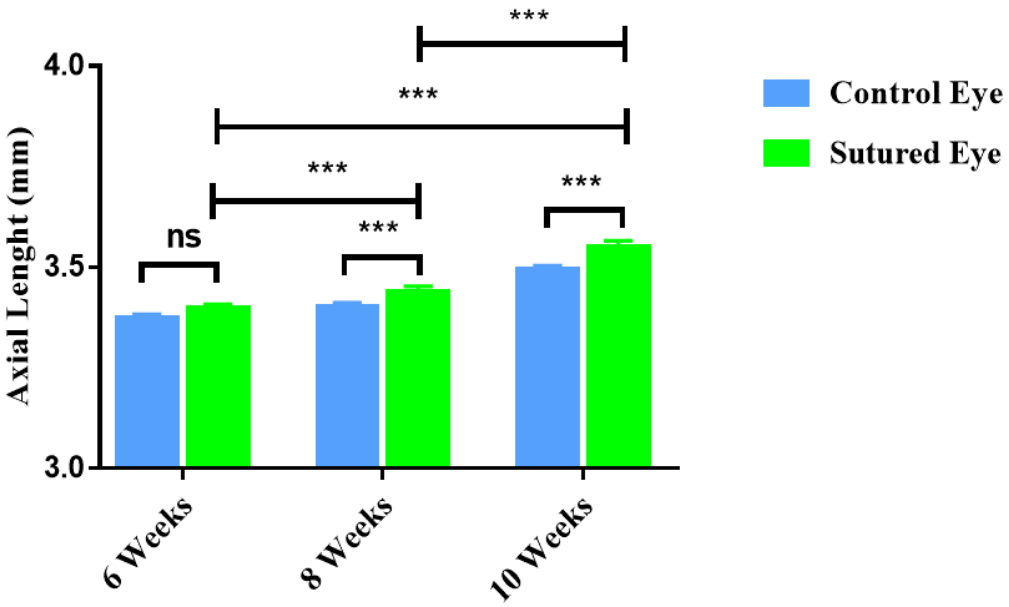

Figure 3.1. Axial length measurement performed with SD-OCT on the control and sutured eye mice. The column graph shows the axial length measurement between the control and sutured eyes in 6, 8, and 10 weeks, respectively. $P \leq 0.001$, was statistically significant in all three groups performed with 2-way ANOVA post-hoc Tukey test.

The averaged AL increased from 3.398mm to 3.547mm (absolute change= 0.15mm; $p \leq 0.05$) within four weeks (at 6 to 10 weeks in the experimental eye), which equates to an estimate of 27 dioptres (D) defocus, - as [an axial elongation of 5.5 to 6µm (0.005-0.006mm) can induce 1D or more of myopia (Christine Schmucker & Frank Schaeffel, 2004)].

3.1.2 Dioptric Power Calculation of Axial Length Measurements.

The dioptric power was calculated based on the OCT axial length measurements. The calculated dioptric power was (± 4.73 D ± 0.99, mean ± S.E.M; n=23) at 6 weeks, (±7.70 D ± 1.4, mean ± S.E.M; n=23) at 8 weeks, and (±10.94 D ± 2.3, mean ± S.E.M; n=23) at 10 weeks respectively in the experimental eye (Figure 3.2). The calculated refractive error based on AL measurements from OCT images served as more precise and reliable data to benchmark against photorefraction data.

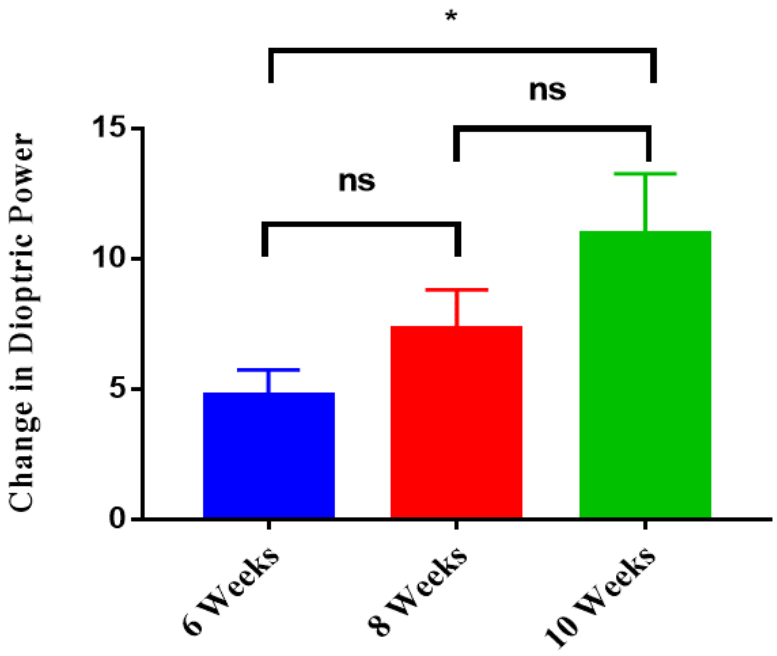

Figure 3.2 Change is dioptric power calculated from the axial length measurements at 6, 8, and 10 weeks. The change in dioptric power between 6 and 10 weeks was statistically significant ($p \leq 0.05$ one-way ANOVA, post-hoc, Tukey test).

3.1.3 Refractive Error measurement with IR Photorefraction

Refractive errors (RE) in mouse eyes were estimated by infrared photorefraction. The average RE of mice at 6 weeks old for the control eye was +4.323D ± 0.7, (mean ±SEM; n=22) whereas in the sutured eye was +0.821 D ± 0.7, (mean ±SEM; n=22). For the 8 weeks old group, control eye RE was +7.490 D ± 0.7, (mean ± SEM, n=22) and in the sutured eye was +3.913 D ± 0.7, (mean ±SEM; n=22). For the 10 weeks old control eye, RE was +10.92 D ± 1.16, (mean ±SEM; n=22) whereas in the sutured eye RE was +5.994 D ± 1.6, (mean ±SEM; n=22).

Hypermetropia was the least at 6 weeks old and relatively higher at 8 weeks old. It reached its peak at 10 weeks for the control eye (RE stabilized at +10.92 D ± 1.16D). We have found a shift in refractive status in the sutured eye, where the amount of refractive power displayed a significantly less hyperopic power than the control eye.

An average difference of -3.502 D, -3.577 D, and -4.978 D of a myopic shift was seen between the control and sutured eyes. There was also an anatomical increased in axial length in the experimental eye in 6/8/10 weeks, respectively. The difference in RE between the control and sutured eyes was statistically significant with $p \leq 0.001$ (2-way ANOVA, post-hoc Tukey test) in 6 weeks, 8 weeks, and 10 weeks, respectively **(Figure 3.3**). Compared to previous studies, more myopic refractions were reported at a younger age (-13D ± -2.0 D; mean ±SD) at 2 days and reached emmetropization at 36 to 40 days in (Tatiana V. Tkatchenko, Shen, & Tkatchenko, 2010).

RE with infrared photorefraction was measured before the axial length measurement to avoid corneal artifact due to the invasive nature of the SD-OCT technique. A total of 10 consecutive measurements were acquired for both eyes to minimize error. Our results were similar to RE measurement by

photorefraction in the normal mice eye ranging from +4D ± 0.6D to +7D ± 2.5D from 30 days to 70 days. (Barathi et al., 2008; C. Schmucker & F. Schaeffel, 2004).

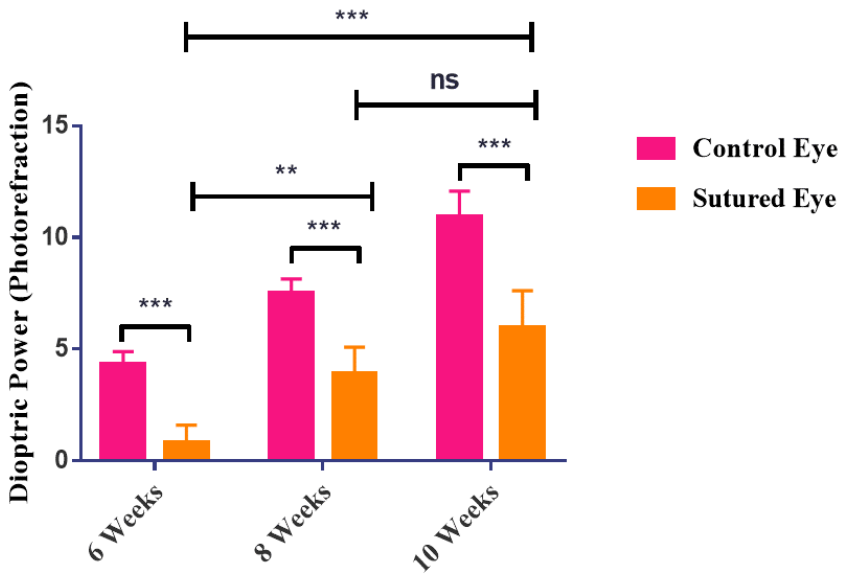

Figure 3.3 Summary of refractive error measurements with Infrared photorefraction in the mouse of 6, 8, and 10 weeks control and sutured eye. $P \leq 0.001$, was statistically significant in all three groups performed with 2-way ANOVA post-hoc Tukey test.

3.1.4 Refractive error measurement with streak retinoscopy

RE with streak retinoscopy was measured after the photorefraction measurements. The average RE of mice at 6 weeks old for the control eye was +4.735D ± 0.4, (mean ±SEM; n=17) whereas in the sutured eye was +4.235 D ± 0.4, (mean ±SEM; n=17). For the 8 weeks old group, control eye RE was +8.118 D ± 0.4, (mean ± SEM, n=17) and in the sutured eye was +7.765 D ± 0.4, (mean ±SEM; n=17). For the 10 weeks old control eye, RE was +9.500 D ± 0.4, (mean ±SEM; n=17) whereas in the sutured eye RE was +8.059 D ± 0.4, (mean ±SEM; n=17). The results were very much similar to photorefraction. The amount of refractive power displayed a significantly less hyperopic power in the

sutured eye compared to the control eye. The difference in RE between the control and sutured eyes was statistically significant with p=0.012 (2-way ANOVA, post-hoc Tukey test) in 10 weeks, whereas 6 and 8 weeks was found not significant **(Figure 3.4).**

Similar to the IR photorefraction, hypermetropia was the least at 6 weeks old, relatively higher at 8 weeks old, and reached its peak at 10 weeks for the control eye (RE stabilized at +9.5 D ± 0.4D).

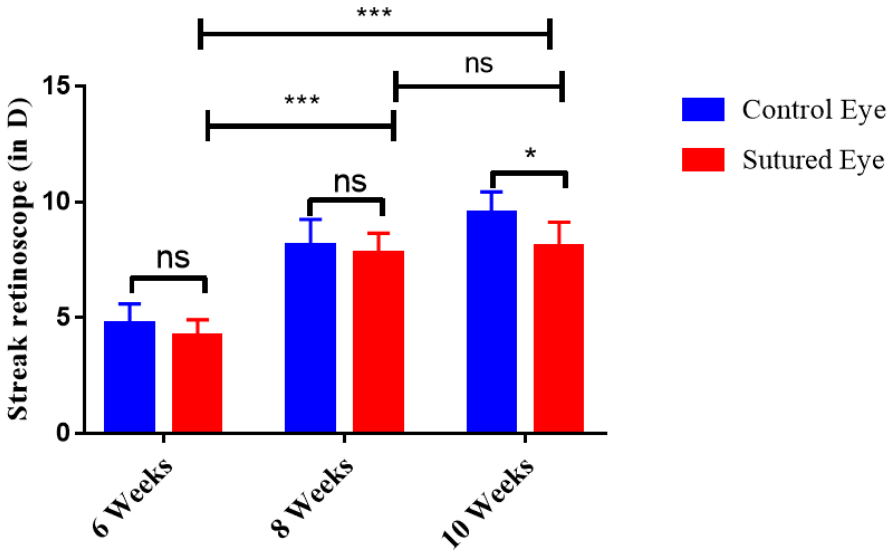

Figure 3.4 Summary of refractive error measurements with Streak retinoscopy in the mouse of 6, 8, and 10 weeks in control and sutured eye. P ≤ 0.003, was statistically significant in the 10 weeks sutured group performed with a 2-way ANOVA post-hoc Tukey test.

3.1.5 Comparison between IR Photorefraction and Streak Retinoscopy

The RE measurement between the photorefraction and streak retinoscopy has shown some differences. This could be possibly because in high hyperopic eyes the streak reflex appears very small and it is difficult to obtain accurate measurements (Pardue et al., 2013).

Also, it is difficult to identify the reflex in eyes with mild cataract and corneal abrasions or scar with streak retinoscopy in the mice, whereas photorefraction can refract even mild opacities quite accurately. The comparison between the measurements of the two groups can be seen in table 3.2.

Table 3-2 Showing a comparison between the RE measured with IR photorefraction and streak retinoscopy.

IR Photorefraction				Streak Retinoscopy		
Groups	Control eye	Suture eye	P-value	Control eye	Suture eye	P-value
6 Weeks	+4.32	+0.821	0.001	+4.75	+4.23	ns
8 Weeks	+7.61	+4.05	0.001	+8.81	+7.13	ns
10 Weeks	+10.92	+5.90	0.001	+8.92	+7.00	0.003

3.2 Electrophysiological recording

3.2.1 Classification of different types of RGCs

A 256 channel Multielectrode Arrays (MEAs) system was used to record the firing pattern of RGCs from the overnight dark-adapted mouse retina from all quadrants. For recording the light-evoked responses, a green (525 nm) light-emitting diode delivered uniform full-field visual stimuli on the surface of the retina. Before recording the RGCs response the retina is given a dark adaptation time of 15 to 20 minutes in the chamber.

RGCs from mouse retina were recorded by using the MEAs system and the response profiles were identified based on firing the ON and OFF set of lights. Based on the response profile to light and firing pattern 5 major types of cells were classified **(Figure 3.5).**

1. **ON-Transient:** ON-Transient cell's response was defined as their firing upon the onset of the light stimulus. The light stimulus starts at time (t) = 0s **(Figure 3.5 A)**. A short spike burst was seen, which was transient, and no further response was found after the stimulus turned off at t=1s.
2. **ON- Sustained:** Upon the onset of the light stimulus, the cell fired and maintained spiking for some time before turning off **(Fig 3.5 B)**. The response maintained from stimulus turned on at t=0 and sustained at the peak till the second onset of stimulus at t=1, thus classified as a sustained response.
3. **OFF- Transient**: OFF cell response was defined upon the firing response while the offset of light stimulus at t = 1s **(Fig 3.5 E)**. A single transient (short burst) peak of the spike was observed when the stimulus turned off at t=1 whereas no substantial second spike response was noted when the stimulus turned on at t=0.

4. **OFF- Sustained**: OFF-Sustained cells responded upon the offset of light stimulus, the cell fired and maintained spiking for some time **(Fig 3.5 F)**. The response was maintained from stimulus turned on at t=1 and sustained at the peak till the second onset of stimulus at t=2, thus classified as a sustained response.
5. **ON- Delayed:** ON-delayed cells were much like the ON response cell type, but their delayed response kinetics which is more than > 0.3-sec latency **(Fig 3.5 C)** upon onset of light stimulus define them delay cell types. These results were very similar to the previous study by (Mani & Schwartz, 2017).
6. **OFF- Delay:** OFF-delayed cells were much like the OFF-response cell type, but their delayed response kinetics which is more than > 0.3-sec latency **(Fig 3.5 G)** upon offset of light stimulus define them delay cell types.
7. **ON-OFF:** ON-OFF cells were defined as responding simultaneously on both the onset and offset of light stimulus at a moment **(Fig 3.5 D)**. Spikes fired on the onset (t=0s) and offset of stimulus at t=1 and t=2 respectively which explain the firing pattern as both ON and OFF.

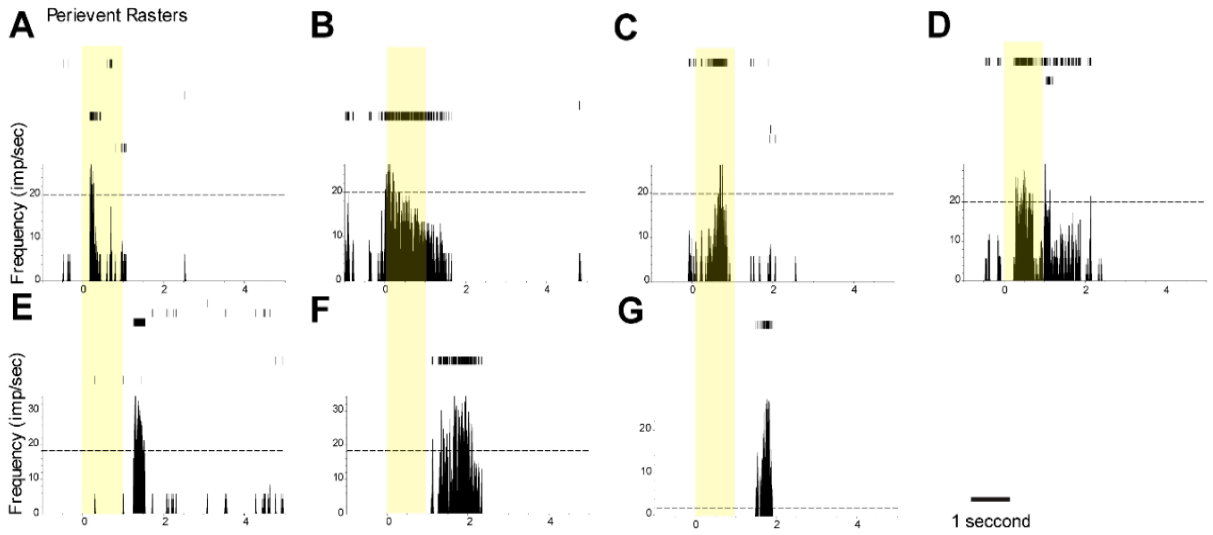

Figure 3.5 Major types of RGCs based on their response profile to light stimulus. Full-field LED of525 nm; with light intensity = 1311 Rh/rod/sec; 1 s stimulation, 5 s interval applied.*

3.2.2 Major Types of RGCs Population

Three different kinds of cell response ON, OFF, and ON/OFF was invented in 1938 by Hartline & Haldan. Frequency, latency, and intensity were completely based on the response fashion of the stimulus intensity and duration (Hartline, 1938). Therefore, we have classified the cells based on their light-evoked activity to square wave stimuli (525 nm full field; I = 1311 Rh*/rod/sec; 1 s stimulation, 5 s interval) the recorded RGCs were classified. An increase in spiking frequencies can be seen to either light ON or OFF sets, respectively which can easily segregate the ON and OFF types of RGCs. Both RGC classes then were further subdivided into sustained (maintained spiking) or transient (short spike bursts) populations similar to previous research by (Murphy & Rieke, 2006; Pang et al., 2003).

The firing of RGCs (n= 8,316) from 33 mouse retina were recorded based on their light-evoked potentials are classified as below in **(Figure 3.6)**. ON transient (n = 436), ON sustained (n = 207), OFF transient (n = 889), OFF sustained (n = 379) and ON-OFF (n = 247), ON delayed (n = 26), OFF

delayed (n = 279). Delayed response RGC types were differentiated based on their delayed response kinetics with >0.3 s latencies. But it must be noted that MEA recordings may comprise of a mixture of RGC and dACs signals. Therefore, all RGC categories might be composed of both RGCs and dACs.

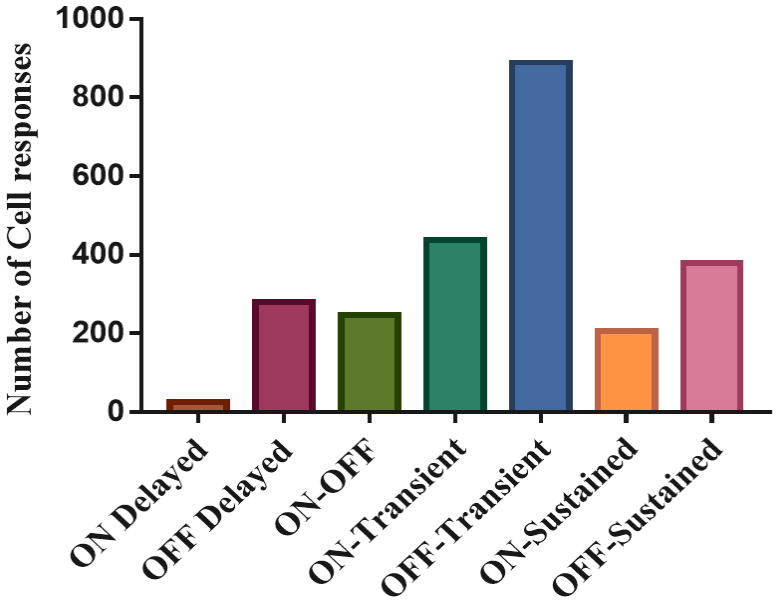

Figure 3.6 Summary of major types of RGCs population response based on light-evoked potential.

After categorization of the different cell types (**Figure 3.6**), firing pattern maps of populations of RGCs were designed and recorded for ON, OFF, ON-OFF, and ON/OFF delayed RGC responses to indicate their positions over the MEA in the following experiments using the color representations shown in figure (**Figure 3.7**).

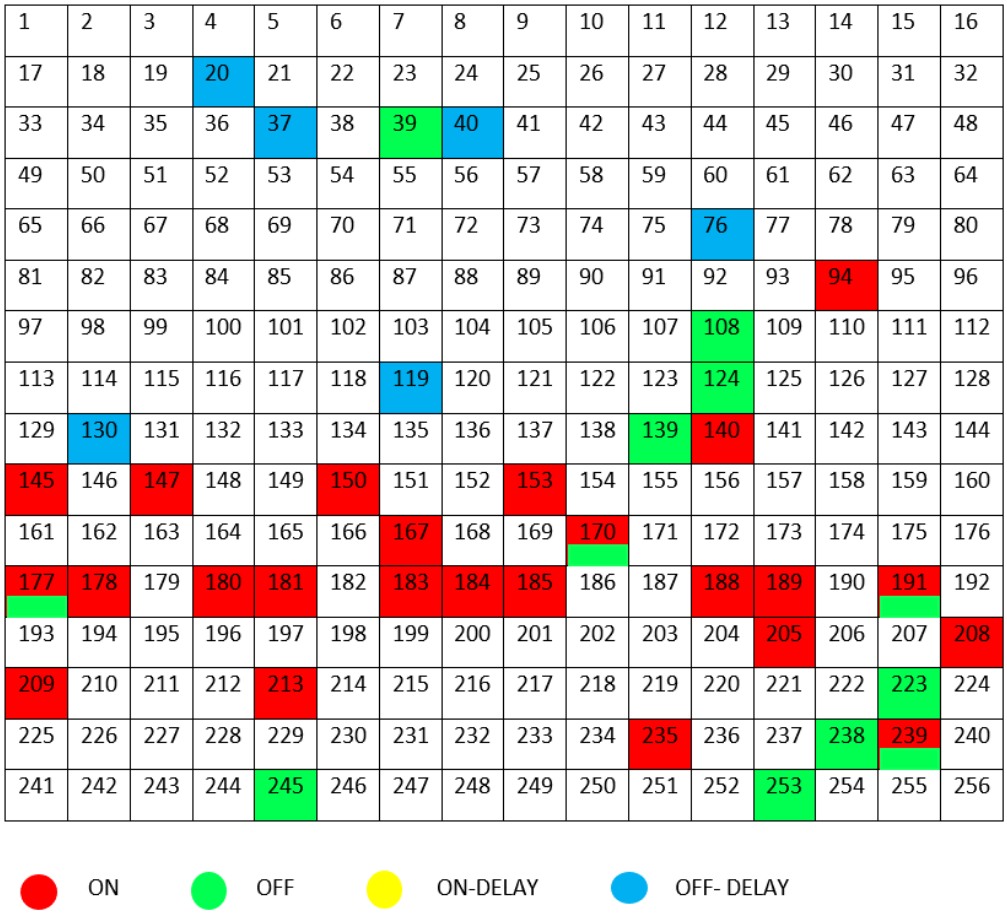

Figure 3.7 Example of the cell response mapping to indicate their position on the MEAs, cells with dual-color indicates two kinds of responses.

The morphology of RGCs visualized by the dye injection method is shown in **figure 3.8**. The ON and OFF alpha RGCs were injected with Neurobiotin injection (red) and double-labeled with anti-ChAT antibody (blue).

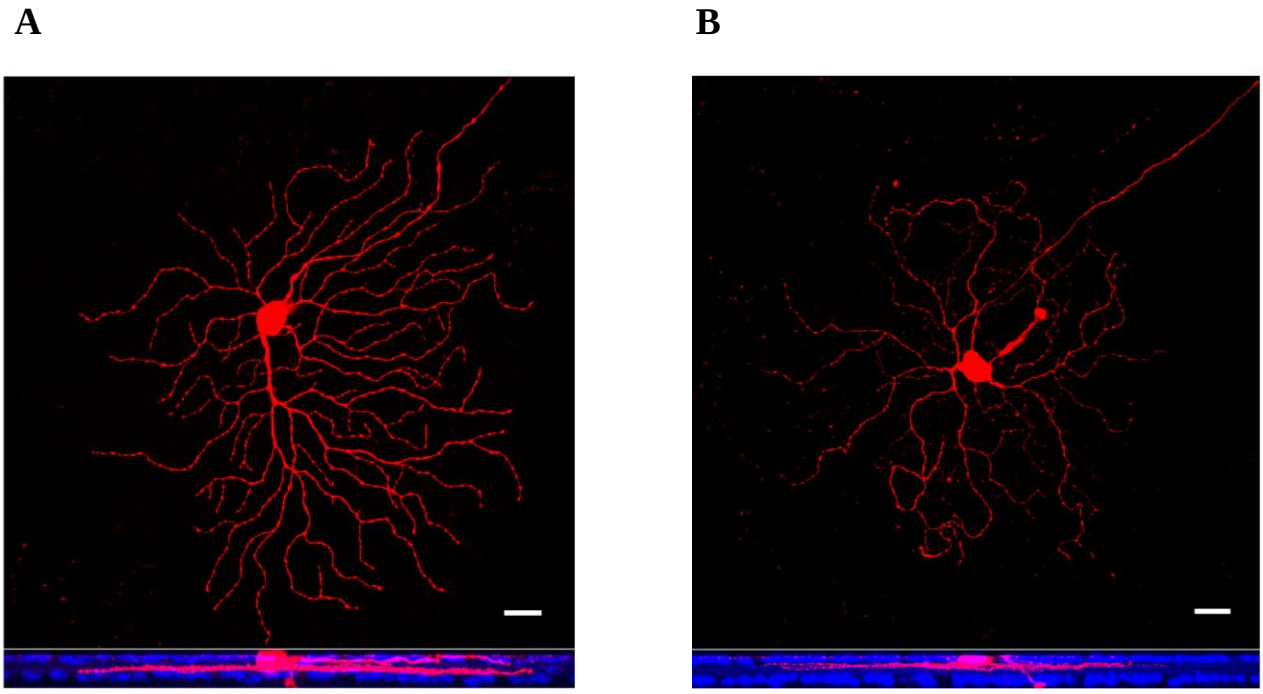

Figure 3.8 (A & B) showed OFF α-RGC and ON α-RGC with Neurobiotin filling after recording. Lower images show the ganglion cell branched in OFF and ON layer with anti-ChAT labelling (Blue). Scale bar- 20µm (Banerjee, Wang, Zhao, et al., 2020).

3.2.3 Major types of RGCs identified with different dioptric power

Firing RGCs (n= 2520 cells) from 10 mouse retinas, postnatal day 56, C57/BL6J mice were examined under different dioptric power of optical defocus, the mouse retina was projected with designated program diameter of 1.804 mm; 0.2 c/d, square-wave grating; Light intensities varied from 1.5×10^5 Rh*/rod/sec to 1.1×10^5 Rh*/rod/sec. Details of the experimental design are shown in section 2.7.4 (**Figure 2.11**).

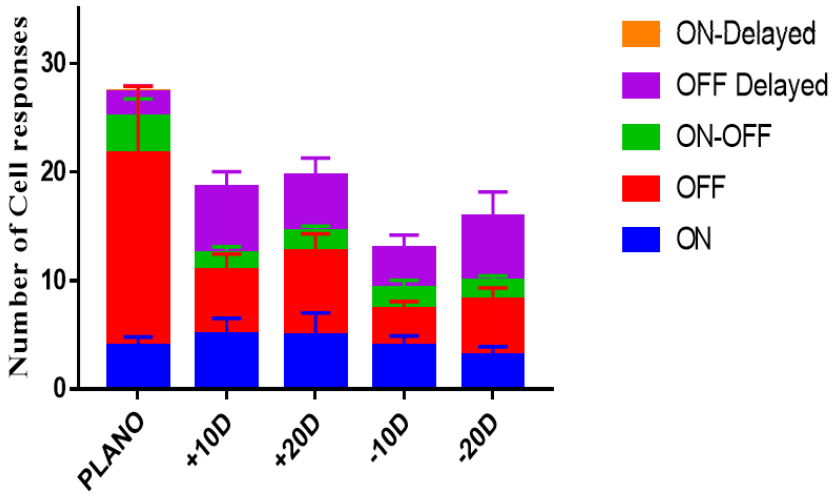

Figure 3.9 Summary of 5 major types of RGCs response recorded with MEA under optical defocused (+10D/+20D/−10D/−20D) conditions.

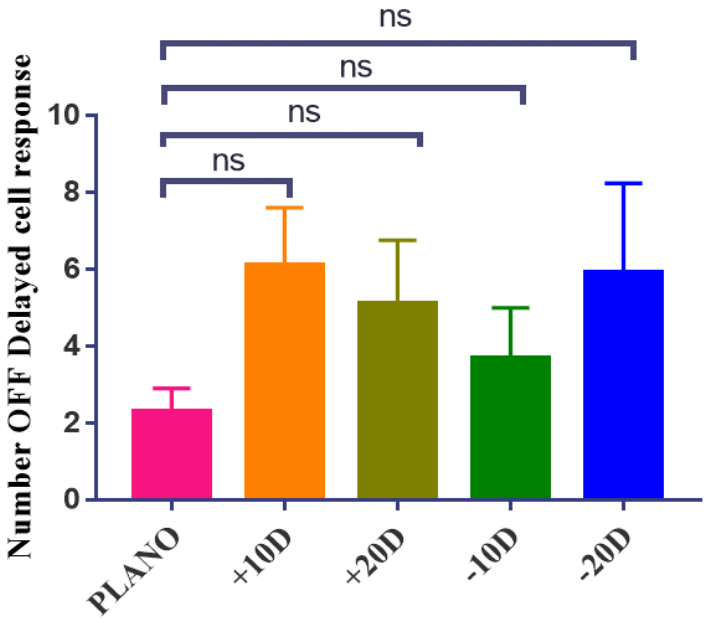

Figure 3.10 Summarizes the number of OFF Delayed cells recorded under different defocus and focus. Difference in between the group were not significant, performed with 2-way ANOVA, post-hoc Tukey test.

A summary of the total numbers of cells responding with different dioptres of optical defocus are shown in **Figure 3.9**. Recording of various cell responses by projecting different dioptric powers revealed that cells with longer time latencies (delayed cells) present in higher numbers compared to the focused image shown in **Figure 3.10**. There was an increase in the response of delayed cells, especially OFF- Delayed GCs cells in response to different dioptric power of defocus, but this did not reach significance. A total of 942 cells from 10 mouse retinas were analyzed at different dioptric powers of defocus and focus.

A total of 274 cell responses were recorded from 10 mouse retinas with focused image projection, while the number of responses was decreased with +/- 10 D and 20 D of defocus to 185/196 cells on +10/20D and 129/158 cells on -10/20D (**Figure. 3.14**). There was no significant difference in the number of ON and ON-OFF responses from focus to different dioptre of defocus. But numbers of

OFF-RGCs and OFF-Delayed RGCs responses were decreased with defocused compared to focused image.

3.2.3.1 Firing pattern of RGCs on different dioptric power.

To examine the biophysical properties and spike responses of RGCs under different dioptric power of optical defocus, the mouse retina was projected with a designed program diameter of 1.804 mm; 0.2 c/d, square-wave grating and light intensities varying from 1.5×10^5 Rh*/rod/sec to 1.1×10^5 Rh*/rod/sec allowing changes in the response properties and specific RGCs conditions under different defocus and focus images to be determined. In the diagrams (**Figure 3.10 to 3.14**) responding, cells were mapped according to their respective positions as MEA system and cell types shown in different colours (Red=ON, Green=OFF, Blue= OFF Delay, Yellow= ON-Delay) that responded.

Changes in the response properties and specific conditions of RGCs under different defocus and focus of an image were determined. Even with the use of different dioptric powers, it appeared that the response was a mixture of RGC and dAC signals because in the mouse retina, the RGCs layer consists of both RGCs and displaced ACs and it is also believed that the dACs are highly stratified in the inner retinal layers (Müller, Shelley, & Weiler, 2007). In the present study, we have recorded signals from the whole-mount retina due to which multiple cell responses were recorded simultaneously with MEA, therefore it is highly plausible that the response recorded from the retina are combinations of RGCs and ACs (Pan et al., 2016). Combined visual signals are transferred from lateral inhibition which includes the functions of HCs and ACs with both feedback and feedforward mechanism. Therefore, the possible gap junction coupling between the RGCs and ACs of the mouse retina was further explored.

Focus

1	2	3	4	5	6	7	8	9	10	11	12	13	14	15	16
17	18	19	20	21	22	23	24	25	26	27	28	29	30	31	32
33	34	35	36	37	38	39	40	41	42	43	44	45	46	47	48
49	50	51	52	53	54	55	56	57	58	59	60	61	62	63	64
65	66	67	68	69	70	71	72	73	74	75	76	77	78	79	80
81	82	83	84	85	86	87	88	89	90	91	92	93	94	95	96
97	98	99	100	101	102	103	104	105	106	107	108	109	110	111	112
113	114	115	116	117	118	119	120	121	122	123	124	125	126	127	128
129	130	131	132	133	134	135	136	137	138	139	140	141	142	143	144
145	146	147	148	149	150	151	152	153	154	155	156	157	158	159	160
161	162	163	164	165	166	167	168	169	170	171	172	173	174	175	176
177	178	179	180	181	182	183	184	185	186	187	188	189	190	191	192
193	194	195	196	197	198	199	200	201	202	203	204	205	206	207	208
209	210	211	212	213	214	215	216	217	218	219	220	221	222	223	224
225	226	227	228	229	230	231	232	233	234	235	236	237	238	239	240
241	242	243	244	245	246	247	248	249	250	251	252	253	254	255	256

Figure 3.11 Firing cells are presented on this checker box plotting map to show the cell's actual position on to the MEA electrode with a focus image projection.

+10.00 D

1	2	3	4	5	6	7	8	9	10	11	12	13	14	15	16
17	18	19	20	21	22	23	24	25	26	27	28	29	30	31	32
33	34	35	36	37	38	39	40	41	42	43	44	45	46	47	48
49	50	51	52	53	54	55	56	57	58	59	60	61	62	63	64
65	66	67	68	69	70	71	72	73	74	75	76	77	78	79	80
81	82	83	84	85	86	87	88	89	90	91	92	93	94	95	96
97	98	99	100	101	102	103	104	105	106	107	108	109	110	111	112
113	114	115	116	117	118	119	120	121	122	123	124	125	126	127	128
129	130	131	132	133	134	135	136	137	138	139	140	141	142	143	144
145	146	147	148	149	150	151	152	153	154	155	156	157	158	159	160
161	162	163	164	165	166	167	168	169	170	171	172	173	174	175	176
177	178	179	180	181	182	183	184	185	186	187	188	189	190	191	192
193	194	195	196	197	198	199	200	201	202	203	204	205	206	207	208
209	210	211	212	213	214	215	216	217	218	219	220	221	222	223	224
225	226	227	228	229	230	231	232	233	234	235	236	237	238	239	240
241	242	243	244	245	246	247	248	249	250	251	252	253	254	255	256

Figure 3.12 Firing cells are presented on this checker box plotting map to show the cell's actual position on to the MEA electrode with +10D defocus.

+20.00 D

1	2	3	4	5	6	7	8	9	10	11	12	13	14	15	16
17	18	19	20	21	22	23	24	25	26	27	28	29	30	31	32
33	34	35	36	37	38	39	40	41	42	43	44	45	46	47	48
49	50	51	52	53	54	55	56	57	58	59	60	61	62	63	64
65	66	67	68	69	70	71	72	73	74	75	76	77	78	79	80
81	82	83	84	85	86	87	88	89	90	91	92	93	94	95	96
97	98	99	100	101	102	103	104	105	106	107	108	109	110	111	112
113	114	115	116	117	118	119	120	121	122	123	124	125	126	127	128
129	130	131	132	133	134	135	136	137	138	139	140	141	142	143	144
145	146	147	148	149	150	151	152	153	154	155	156	157	158	159	160
161	162	163	164	165	166	167	168	169	170	171	172	173	174	175	176
177	178	179	180	181	182	183	184	185	186	187	188	189	190	191	192
193	194	195	196	197	198	199	200	201	202	203	204	205	206	207	208
209	210	211	212	213	214	215	216	217	218	219	220	221	222	223	224
225	226	227	228	229	230	231	232	233	234	235	236	237	238	239	240
241	242	243	244	245	246	247	248	249	250	251	252	253	254	255	256

Figure 3.13 Firing cells are presented on this checker box plotting map to show the cell's actual position on to the MEA electrode with +20D defocus.

-10.00 D

1	2	3	4	5	6	7	8	9	10	11	12	13	14	15	16
17	18	19	20	21	22	23	24	25	26	27	28	29	30	31	32
33	34	35	36	37	38	39	40	41	42	43	44	45	46	47	48
49	50	51	52	53	54	55	56	57	58	59	60	61	62	63	64
65	66	67	68	69	70	71	72	73	74	75	76	77	78	79	80
81	82	83	84	85	86	87	88	89	90	91	92	93	94	95	96
97	98	99	100	101	102	103	104	105	106	107	108	109	110	111	112
113	114	115	116	117	118	119	120	121	122	123	124	125	126	127	128
129	130	131	132	133	134	135	136	137	138	139	140	141	142	143	144
145	146	147	148	149	150	151	152	153	154	155	156	157	158	159	160
161	162	163	164	165	166	167	168	169	170	171	172	173	174	175	176
177	178	179	180	181	182	183	184	185	186	187	188	189	190	191	192
193	194	195	196	197	198	199	200	201	202	203	204	205	206	207	208
209	210	211	212	213	214	215	216	217	218	219	220	221	222	223	224
225	226	227	228	229	230	231	232	233	234	235	236	237	238	239	240
241	242	243	244	245	246	247	248	249	250	251	252	253	254	255	256

Figure 3.14 Firing cells are presented on this checker box plotting map to show the cell's actual position on to the MEA electrode with -10D defocus.

-20.00 D

1	2	3	4	5	6	7	8	9	10	11	12	13	14	15	16
17	18	19	20	21	22	23	24	25	26	27	28	29	30	31	32
33	34	35	36	37	38	39	40	41	42	43	44	45	46	47	48
49	50	51	52	53	54	55	56	57	58	59	60	61	62	63	64
65	66	67	68	69	70	71	72	73	74	75	76	77	78	79	80
81	82	83	84	85	86	87	88	89	90	91	92	93	94	95	96
97	98	99	100	101	102	103	104	105	106	107	108	109	110	111	112
113	114	115	116	117	118	119	120	121	122	123	124	125	126	127	128
129	130	131	132	133	134	135	136	137	138	139	140	141	142	143	144
145	146	147	148	149	150	151	152	153	154	155	156	157	158	159	160
161	162	163	164	165	166	167	168	169	170	171	172	173	174	175	176
177	178	179	180	181	182	183	184	185	186	187	188	189	190	191	192
193	194	195	196	197	198	199	200	201	202	203	204	205	206	207	208
209	210	211	212	213	214	215	216	217	218	219	220	221	222	223	224
225	226	227	228	229	230	231	232	233	234	235	236	237	238	239	240
241	242	243	244	245	246	247	248	249	250	251	252	253	254	255	256

Figure 3.15 Firing cells are presented on this checker box plotting map to show the cell's actual position on to the MEA electrode with -20D defocus

Change in the firing pattern can be observed in the MEA checker box plot map of firing cells with various focus and defocus (**Figure 3.10 to 3.14**) as in section 3.2.3.1, each box represents the electrode specific number and the color in the box represents the firing type of RGC/dACs response, with color-coding as before. The total number of actively responding RGCs obtained from the

recordings were 29 in focus; 24 in +10D (4 in the same position): 33 in +20D (7 in the same position), 32 in −10D (10 in the same position); 29 in −20D (6 in the same position).

There were 12 ON responses with a focused image but these changed instantly when a defocused image was projected as shown in Table 3.3.

Table 3-3 Altered responses of ON cells under defocus.

No. of cells	Changed Responses			
	Degree of defocus			
	+10D	+20D	-10D	-20D
6	None	None	None	None
2			None	
1				None
2			OFF	OFF
1		OFF		

- Blank cells indicate no response

In the same study experiment, 9 OFF responding RGCs were observed in focus status, but this changed instantly in defocus conditions to 7 and 11 cells at +10D and +20D respectively and, 2 and 1 at -10D and -20D of defocus. Responses of these 9 altered cells with defocused images as shown in table 3.4 below.

Table 3-4 Altered responses of OFF cells under defocus.

No. of cells	Changed Responses			
	Degree of defocus			
	+10D	+20D	-10D	-20D
5	None	None	None	None
2		ON-OFF	ON-OFF	ON-OFF
1		OFF	OFF	
1		ON	ON-OFF	

- Blank cells indicate no response

Changes to defocus were also noted in the 6 ON-OFF responding RGCs under focused status as shown in table 3.5.

Table 3-5 Altered responses of ON-OFF cells under defocus.

No. of cells	Changed Responses			
	Degree of defocus			
	+10D	+20D	-10D	-20D
3	None	None	None	None
2	ON	ON	ON	
1	OFF	ON	ON	OFF

- Blank cells indicate no response

Although only a few ON/OFF delayed RGCs were observed in focused status (n = 2), and +10D (n = 3) and +20D (n = 1) defocused status, the number of OFF-Delayed cells increased to 13 in -10D and

23 in -20D. Three OFF-Delayed cells were found in the same position in both -10/20D of defocus with the same response, but close to 10 cells have lost their response in -20D of defocus.

3.2.3.2 Effects of gap junction blocker on RGCs

To observe the effect of gap junctions on the response of RGCs firing pattern, 25 µM of 18-Beta glycyrrhetinic acid, a non-selective gap junction blocker was applied. 18-Beta effectively uncoupled cells and eliminate spontaneous spiking of RGCs but cannot reverse the response back (Völgyi et al., 2013). After its application, the probability of the RGCs firing response decreased dramatically (**Figure 3.15**), there is no response regardless of different spatial frequencies or dioptric powers of defocus. One of the possible reasons is that the responses recorded were enabled by gap junctions and the firing pattern of a GC correlated with that of its neighboring AC's response. As ON and OFF alpha RGCs are coupled with AC's or other OFF alpha RGCs in the mouse retina, the findings indicate that AC's contribute to the responses of RGCs to defocused image status. Also, 25 µM of 18-Beta glycyrrhetinic acid might block the RGCs light response by blocking the sodium channel (Du et al., 2012).

1	2	3	4	5	6	7	8	9	10	11	12	13	14	15	16
17	18	19	20	21	22	23	24	25	26	27	28	29	30	31	32
33	34	35	36	37	38	39	40	41	42	43	44	45	46	47	48
49	50	51	52	53	54	55	56	57	58	59	60	61	62	63	64
65	66	67	68	69	70	71	72	73	74	75	76	77	78	79	80
81	82	83	84	85	86	87	88	89	90	91	92	93	94	95	96
97	98	99	100	101	102	103	104	105	106	107	108	109	110	111	112
113	114	115	116	117	118	119	120	121	122	123	124	125	126	127	128
129	130	131	132	133	134	135	136	137	138	139	140	141	142	143	144
145	146	147	148	149	150	151	152	153	154	155	156	157	158	159	160
161	162	163	164	165	166	167	168	169	170	171	172	173	174	175	176
177	178	179	180	181	182	183	184	185	186	187	188	189	190	191	192
193	194	195	196	197	198	199	200	201	202	203	204	205	206	207	208
209	210	211	212	213	214	215	216	217	218	219	220	221	222	223	224
225	226	227	228	229	230	231	232	233	234	235	236	237	238	239	240
241	242	243	244	245	246	247	248	249	250	251	252	253	254	255	256

Figure 3.16 Response of RGCs under 18-Beta glycyrrhetinic acid a non-selective gap junction blocker application.

3.3 Firing Pattern of RGCs in myopic Vs Non-myopic mouse retina

In myopia, the structural and functional performance is reduced compared to emmetropia. In moderate to high myopia, the outer plexiform layer to the nerve fibre layers thickness reduces and causes retinal thinning (Wolsley, Saunders, Silvestri, & Anderson, 2008).To determine the basic changes in the firing pattern of RGCs in the myopic retina, RGCs response were recorded from form-deprivation myopic mouse retina. Five mice with successful myopia development were evaluated by projecting focused and defocused images to the experimental eye (sutured eye). Firing RGCs (n= 1,260) cells from the retinas were recorded by using the MEAs system.

Response from a total of 139 cells from 5 mouse retinas were recorded and analyzed. These included responses under clear and blur image projections. Responses were recorded under focused image (0.2c/d square wave grating image) projection from 58 (41.7%) cells, but the numbers of responses were reduced to 53 cells (38.1%) with defocused images (0.2c/d gaussian blur) **(Figure 3.17)**. Almost 52.9% of cell response firing was found in the same location between the focus and defocus image projection.

Overall, no statistically significant change was observed in the firing pattern of RGCs examined under focused and defocused images on the myopic mouse retina, as shown in **Figure 3.17**.

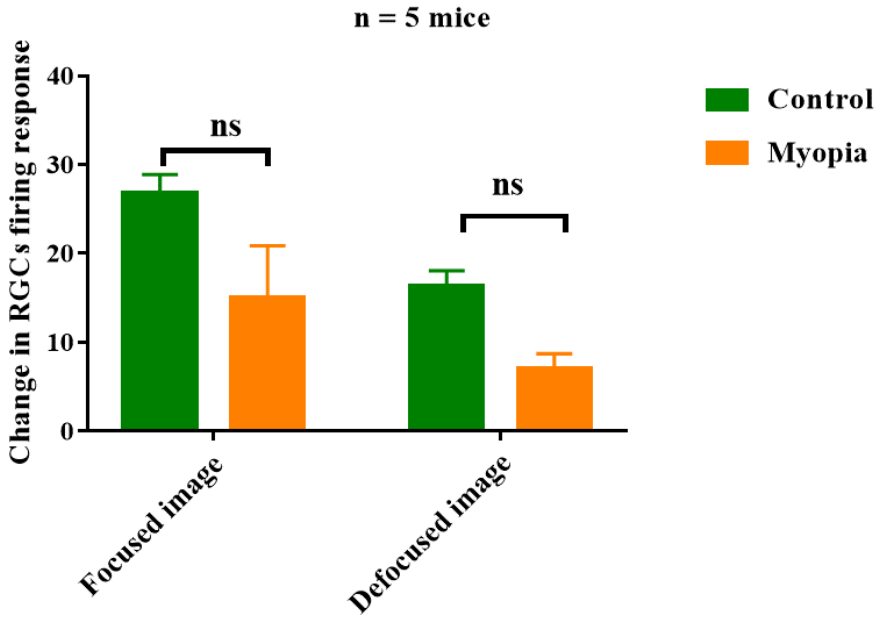

Figure 3.17 Bar graph showing the RGCs cell response in myopia induced and control mice under focused and defocused image projection (None of the group shown any significance performed 2-way ANOVA post-hoc Tukey test).

3.4 RGCs respond to different spatial frequency images.

To observe the firing pattern response of RGCs images of different spatial frequencies made using PsychoPy programming language were designed and tested. A pilot study was conducted using spatial frequencies ranging from 0.001 to 0.5 c/d and a box-plot graph with SEM plotted for statistical analysis (**figure 3.17**). The projected image was designed as a 5 × 5 array image which covers an area of 300 µm in height and 300 µm in width from spatial frequency 0.001c/d, 0.1c/d, 0.2c/d, 0.4 c/d, and 0.5 c/d (light intensity 7.4×10^4 Rh*/rod/sec; stimuli time 1 s in 6 s circle for 10 min) which was projected onto the surface of the in-vitro retina preparation for 10 min and RGCs firing patterns recorded. A total of 2,520 firing RGCs were observed from (n=10) mouse retina. The cells had a maximum response with 0.2 c/d and a minimum of 0.5 c/d **(Figure 3.17)**. A spatial frequency of 0.2 c/d represents a clear image whereas 0.5 c/d represents a blurred image.

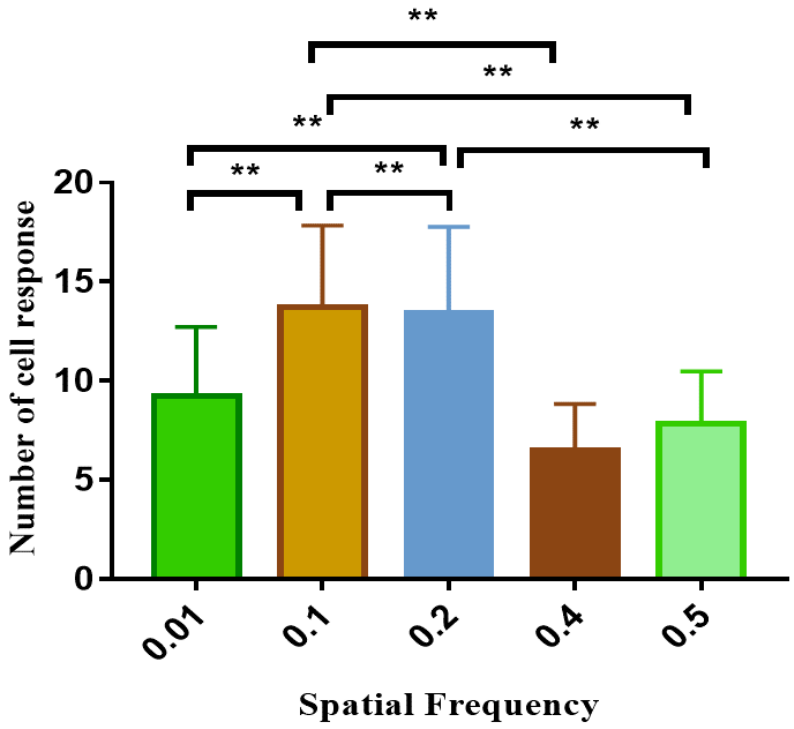

Figure 3.18 The bar graph shows the RGCs cell's response to different spatial frequencies, difference between the group is statistically significant with p< 0.001 performed by 2-WAY ANOVA post-hoc Tukey test. 0.2 c/d spatial frequency has shown a maximal response.

Firing RGCs (n= 8,316) cells from 33 mouse retinas were recorded from all quadrants by using the MEAs system and the response profiles were identified based on response firing upon different spatial frequencies. From the pilot study **(Figure 3.18)** spatial frequency 0.2 c/d was selected as a clear image and 0.5 c/d as a blurred image. Based on the response profile to these spatial frequencies, five types of cells were identified **(Figure 3.19)**. Projection of the 0.2 c/d image resulted in active responses from ON (n = 198), OFF (n = 486), ON-OFF (n = 102), ON delayed (n = 16), and OFF delayed (n = 157) cells whereas with 0.5 c/d the responses were fewer with the exception of OFF-Delayed cells response: ON (n = 137), OFF (n = 237), ON-OFF (n = 125), ON delayed (n = 9), OFF delayed (n = 322) **(Figure 3.19)**. A total of 830 cells from 33

retinas had a response under 0.5 c/d, which increased to 959 cells (86.5 %) after a 0.2 c/d image projected. Of these cells, only 251 cells (26.2 %) had a response in the original position.

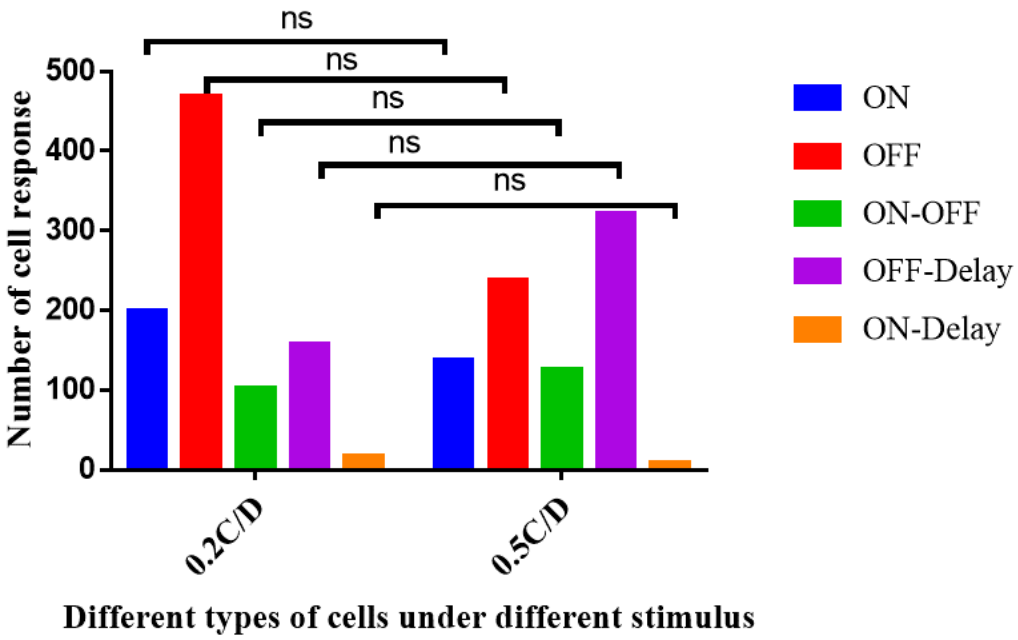

Figure 3.19 Summary of number of responses of 5 cell types (ON, OFF, ON-OFF and ON and OFF delayed) recorded with MEA at different spatial frequencies (0.2 c/d and 0.5 c/d). The number of cell responses were not significant between the group $p>0.05$, performed with paired t-test.

3.4.1 Firing Pattern of RGCs under Different Spatial Frequencies.

To understand the temporal and biophysical properties of the RGCs when focused images (0.2 c/d spatial frequency) are switched to defocused images (0.5 c/d spatial frequency), an image sequence

was presented. Similar to the previous experiment, different populations of RGCs were recorded. ON, OFF, ON-OFF, and ON/OFF delayed RGC responses were color-coded as shown in **Figure 3.7**.

In the first trial, a 0.5 c/d grating image was projected to record RGCs responses (**Figure 3.19**). Following the first recording session, the image was switched to 0.2 c/d grating and the firing patterns were rerecorded and remapped **(Figure 3.20)**. Compared with 0.5 c/d grating image recording, 0.2 c/d recordings resulted in a higher number of active units (40 in 0.2 c/d vs. 24 in the first 0.5 c/d experiments).

Interestingly, however, only 12 cells responded to both 0.5 c/d and 0.2 c/d stimuli in the same position. Of these 12 cells, only one retained the same cell responses (remained ON-OFF response), the other 11 cells, instantly change their response as shown below in table 3.6.

Table 3-6 Altered RGCs response under different spatial frequencies

No. of cells	Changed response	
	Different spatial frequencies	
	0.5 c/d	0.2 c/d
1	OFF	ON-OFF
1	OFF-D	ON
1	OFF-D	OFF
3	OFF-D	ON-OFF
1	ON	OFF
3	ON-OFF	OFF
1	ON-OFF	OFF-D

All other recorded RGCs responded to either 0.5 c/d (12 cells) or the 0.2 c/d stimuli (28 cells) but not in the same position. The 0.5 c/d image sequence was projected a second time (repeated) to test the uniformity of RGC responses **(Figure 3.21)**.

The repeat 0.5 c/d image projection, firing pattern map, produced from retesting to confirm the firing pattern, similar to former 0.5 c/d image projection. A total of 32 RGCs responded to the 0.5 c/d stimulation (repeated round), with 15/24 cells that responded to the first 0.5 c/d recordings recorded RGC responses in the same position as the first 0.5 c/d image projection. Out of these 15 cells, 8 cells keep the same responses in the same position (6 OFF cells, 1 ON cell, and 1 ON-OFF cell); 7 cells changed to other responses as shown below in table 3.7.

Table 3-7 Altered RGCs response under different spatial frequencies

No. of cells	Changed response	
	Different spatial frequencies	
	0.5 c/d	0.5 c/d repeat
2	OFF	ON-OFF
1	ON-OFF	ON
4	ON-OFF	OFF

Overall, 22 experiments were performed in which the defocus and focus images of 0.2 and 0.5 c/d were repeatedly projected on to the retina in a three-phase swapping. **Table 3.8** below shows the number of cell responses under repeated swapping of 0.2c/d and 0.5c/d stimulus projection.

Table 3-8 RGCs response to similar stimulus presentation

0.5 c/d to 0.2 c/d to again 0.5 c/d								
Exp. NO	No. of cells	0.5	0.2	0.5 REPEAT	Same response	Altered response	Same position	Different position
1	37	10	17	10	2	8	4	6
2	48	15	19	14	4	1	5	9
3	125	30	60	35	7	21	11	24
4	42	12	16	14	3	9	8	5
5	42	9	22	11	4	2	5	6
6	77	18	38	21	7	4	7	13
7	84	20	37	27	6	6	8	17
8	82	25	38	19	4	5	7	11
9	54	15	28	11	2	3	6	5
10	54	17	18	19	5	4	7	11
11	80	23	32	25	6	3	8	16
0.2 c/d to 0.5 c/d to again 0.2 c/d								
Exp. NO	No. of cells	0.2	0.5	0.2 REPEAT	Same response	Altered response	Same position	Different position
1	99	36	23	40	11	12	24	17
2	120	46	29	45	5	14	19	26
3	131	48	37	46	7	8	19	27
4	118	31	33	54	6	5	11	43
5	121	57	31	33	12	7	5	26
6	60	19	13	28	6	2	6	20
7	89	45	20	24	5	11	15	8
8	103	36	27	40	8	7	17	21
9	91	32	24	35	4	7	10	21
10	81	26	17	38	7	2	11	22

0.5

1	2	3	4	5	6	7	8	9	10	11	12	13	14	15	16
17	18	19	20	21	22	23	24	25	26	27	28	29	30	31	32
33	34	35	36	37	38	39	40	41	42	43	44	45	46	47	48
49	50	51	52	53	54	55	56	57	58	59	60	61	62	63	64
65	66	67	68	69	70	71	72	73	74	75	76	77	78	79	80
81	82	83	84	85	86	87	88	89	90	91	92	93	94	95	96
97	98	99	100	101	102	103	104	105	106	107	108	109	110	111	112
113	114	115	116	117	118	119	120	121	122	123	124	125	126	127	128
129	130	131	132	133	134	135	136	137	138	139	140	141	142	143	144
145	146	147	148	149	150	151	152	153	154	155	156	157	158	159	160
161	162	163	164	165	166	167	168	169	170	171	172	173	174	175	176
177	178	179	180	181	182	183	184	185	186	187	188	189	190	191	192
193	194	195	196	197	198	199	200	201	202	203	204	205	206	207	208
209	210	211	212	213	214	215	216	217	218	219	220	221	222	223	224
225	226	227	228	229	230	231	232	233	234	235	236	237	238	239	240
241	242	243	244	245	246	247	248	249	250	251	252	253	254	255	256

Figure 3.20 RGCs firing response to different defocused images on MEA recording and mapped with 0.5c/d spatial frequency

0.2

1	2	3	4	5	6	7	8	9	10	11	12	13	14	15	16
17	18	19	20	21	22	23	24	25	26	27	28	29	30	31	32
33	34	35	36	37	38	39	40	41	42	43	44	45	46	47	48
49	50	51	52	53	54	55	56	57	58	59	60	61	62	63	64
65	66	67	68	69	70	71	72	73	74	75	76	77	78	79	80
81	82	83	84	85	86	87	88	89	90	91	92	93	94	95	96
97	98	99	100	101	102	103	104	105	106	107	108	109	110	111	112
113	114	115	116	117	118	119	120	121	122	123	124	125	126	127	128
129	130	131	132	133	134	135	136	137	138	139	140	141	142	143	144
145	146	147	148	149	150	151	152	153	154	155	156	157	158	159	160
161	162	163	164	165	166	167	168	169	170	171	172	173	174	175	176
177	178	179	180	181	182	183	184	185	186	187	188	189	190	191	192
193	194	195	196	197	198	199	200	201	202	203	204	205	206	207	208
209	210	211	212	213	214	215	216	217	218	219	220	221	222	223	224
225	226	227	228	229	230	231	232	233	234	235	236	237	238	239	240
241	242	243	244	245	246	247	248	249	250	251	252	253	254	255	256

Figure 3.21 The map of the firing pattern changed after image stimulation shifted to 0.2 c/d.

0.5 repeat

1	2	3	4	5	6	7	8	9	10	11	12	13	14	15	16
17	18	19	20	21	22	23	24	25	26	27	28	29	30	31	32
33	34	35	36	37	38	39	40	41	42	43	44	45	46	47	48
49	50	51	52	53	54	55	56	57	58	59	60	61	62	63	64
65	66	67	68	69	70	71	72	73	74	75	76	77	78	79	80
81	82	83	84	85	86	87	88	89	90	91	92	93	94	95	96
97	98	99	100	101	102	103	104	105	106	107	108	109	110	111	112
113	114	115	116	117	118	119	120	121	122	123	124	125	126	127	128
129	130	131	132	133	134	135	136	137	138	139	140	141	142	143	144
145	146	147	148	149	150	151	152	153	154	155	156	157	158	159	160
161	162	163	164	165	166	167	168	169	170	171	172	173	174	175	176
177	178	179	180	181	182	183	184	185	186	187	188	189	190	191	192
193	194	195	196	197	198	199	200	201	202	203	204	205	206	207	208
209	210	211	212	213	214	215	216	217	218	219	220	221	222	223	224
225	226	227	228	229	230	231	232	233	234	235	236	237	238	239	240
241	242	243	244	245	246	247	248	249	250	251	252	253	254	255	256

Figure 3.22 Following the repeated presentation of 0.5 c/d image stimulation onto the retina, 46.6% of cells had a response in the same position.

3.4.2 RGCs response on identical image projection

Firing RGCs (n=5,544) were recorded from 22 mouse retina by projecting focused images (0.2 c/d spatial frequency) are switched to defocused images (0.5 c/d spatial frequency), and again switched back to (0.2 c/d spatial frequency) and vice versa. To identify whether RGCs can respond in a similar pattern to a similar image we have presented two image sequences.

Firstly, projected the image sequence **(Group 1)-0.2 c/d to 0.5 c/d to again 0.2 c/d.** In this experiment, (n= 10 mouse retina, 2520 cells), we have found that about 376 RGCs responded on 0.2 c/d stimulation and when the image switched to 0.5 c/d to again back to 0.2 c/d, interestingly 137 RGCs fired exactly in the same positions. Out of these 376 RGCs, 71 RGCs have the same response. Whereas 75 RGCs have changed their response pattern **(Figure 3.24)**. Secondly, we projected the image sequence **(Group 2)-0.5 c/d to 0.2 c/d to again 0.5 c/d** (n= 11 mouse retina, 2772) cells. A total of about 194 RGCs responded on 0.5 c/d stimulation and when the image switched to 0.2 c/d to again back to 0.5 c/d, it resulted in the firing of 66 RGCs exactly in the same position. Out of these 194 RGCs, 50 RGCs have a similar response whereas 66 RGCs have a change in the response pattern **(Figure 3.23)**. The results suggested that the response of RGCs showed a similar firing pattern with more than 60% of cells firing in similar positions, although with the altered response **(Figure 3.23 and 3.24)**. In both, the conditions of image sequences the number of cells fired in the same position and same cell response were significantly decreased when similar images projected onto the same retina.

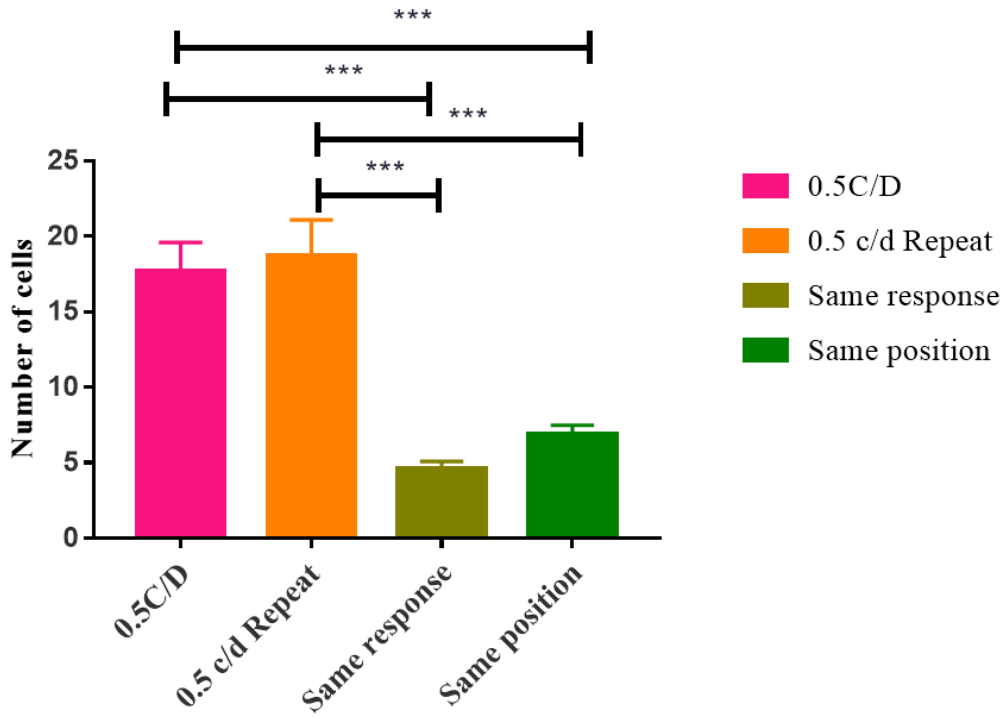

Figure 3.23 Bar graph showing the response of RGCs on repeated image projection, Image sequence 0.5-0.2-0.5 repeat (Group 2). Difference between the group is statistically significant with $p<0.001$, performed with 2-way ANOVA, post-hoc Tukey test.

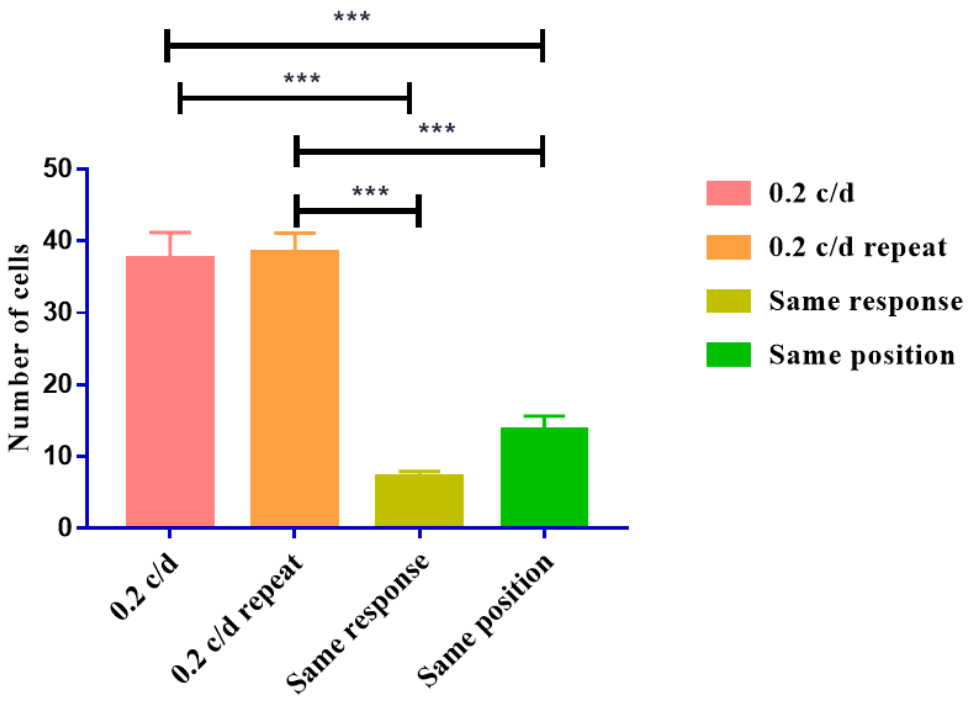

Figure 3.24 Bar graph showing the response of RGCs on repeated image projection, Image sequence 0.2-0.5-0.2 repeat (Group 1). Difference between the group is statistically significant with p<0.001, performed with 2-way ANOVA, post-hoc Tukey test.

3.4.3 RGCs firing on different spatial frequency program design.

Following the cell's responses with a 5×5 array pattern program, the next step was to compare the population of RGCs firing patterns evoked by focused and blurred images. To achieve this, a stimulus of 10×10 matrix of spatial grating images of 0.2 c/d and square wave grating for focus image was programmed, whereas Gaussian blur was used for defocusing the image. The spatial proportions of the specific image were 270 µm in height and 310 µm in width **(Figure 3.25 A–C)** and the entire matrix arrangement was projected onto the surface of the in-vitro mouse retina preparation. An array of images substantially enhanced the capacity to project images onto the retina in the MEA recording.

Besides, the image pattern could be used for tracking and mapping the MEA responses from the retinal cells.

Projection of the 0.2 cycles/degree spatial frequency, square-wave grating **(Figure 3.25 A, C)** in 10 x 10 image array (square shape; I: 8.6×10^4 Rh*/rod/sec; light stimulus time is 1 s, at 5 s interval recorded for 60 min). Then, to mimic the blurred image, a 0.2 cycle/degree, (circle shape, Gaussian blur) **(Figure 3.25 B, C)** image array (the light intensity decreased to 6.1×10^4 Rh*/rod/sec; the lowlight-sensitive-RGCs but still it can be activated; light stimulus time was 1 s and recorded for 60 min) was projected.

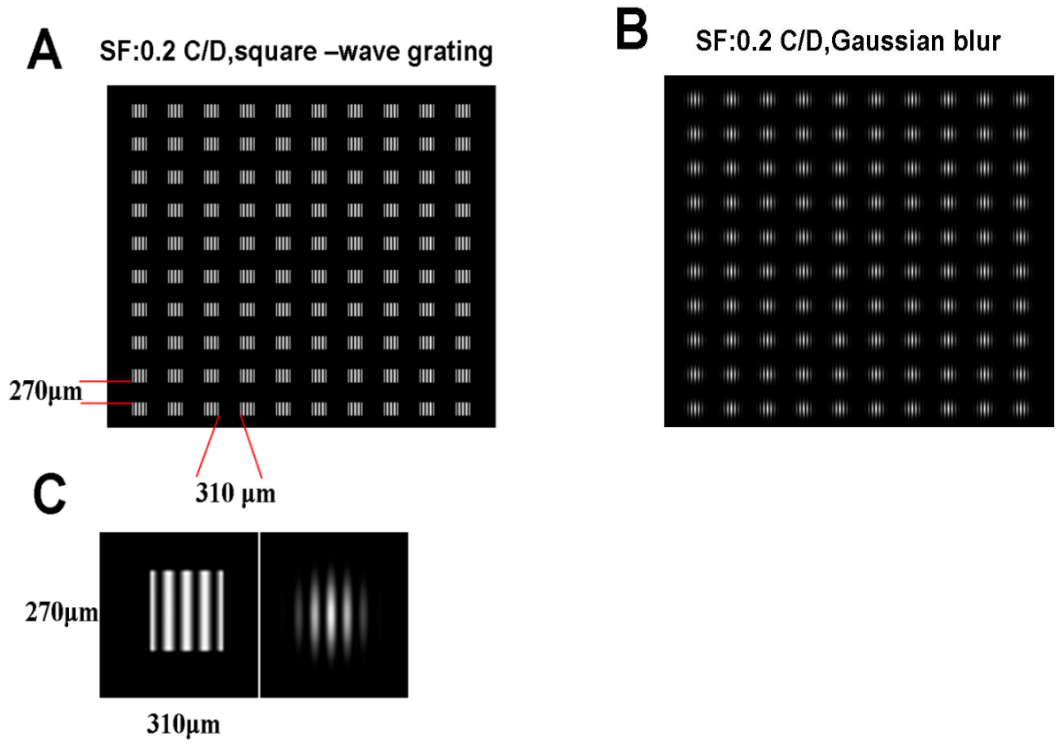

Figure 3.25 10 × 10 image array program projected with each 270µm x 310µm, spatial frequency 0.2 cycle/degree (c/d) (A and C, clear image, square–wave grating) and 0.2 C/D (B and C, blurred image, Gaussian blur).

3.4.4 Change in RGCs firing pattern on different spatial frequencies

The population of RGCs firing to 0.2 c/d, square-wave grating **(Figure 3.26)** reflected the pattern of image cluster and was anticipated as RGCs whose assumed open areas (recorded RGC somata are not essentially found within the center of RGC responsive areas) were secured by picture frameworks shown spiking actions more regularly than those with the responsive areas falling out of the picture cluster. The RGCs action design coordinated the image cluster design anticipated on the retina. The 0.2 c/d grating gaussian blur image covered very few responses from RGC light-evoked reactions **(Figure 3.27)**. Compared with the clear centred picture, the number of firing RGCs diminished drastically from 78 firing cells in 0.2c/d, square wave grating to 11 cells in 0.2 c/d gaussian blur. The RGC's firing pattern was approximately 3.8% colocalized between the clear and blur image projection **(Figure 3.26 and 3.27)**. Overall a complete loss of pattern appeared when the projection of the image switched between the square-wave grating and gaussian blur.

0.2 c/d

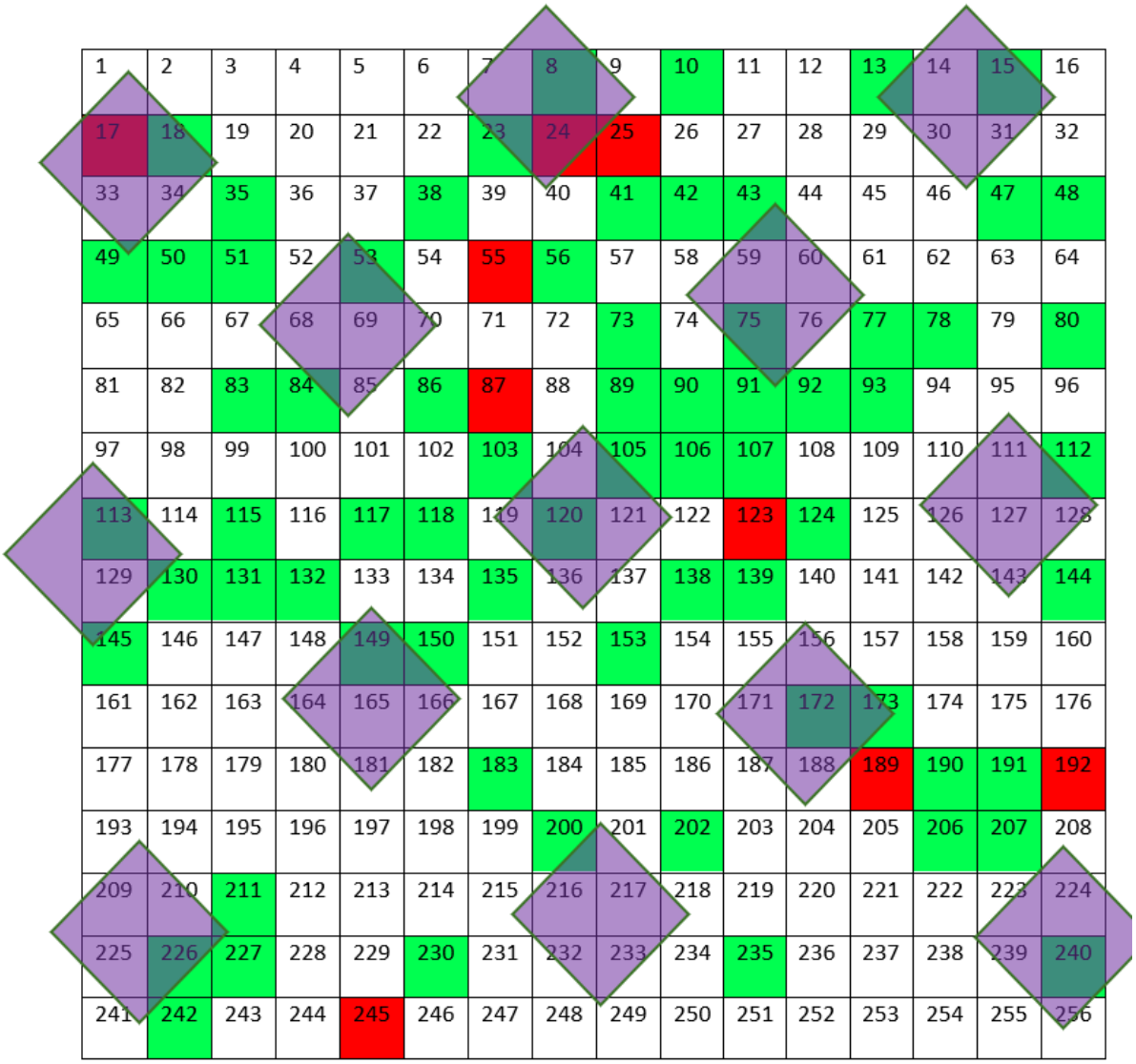

Figure 3.26 The Firing pattern of different RGCs/ACs on a projection of a clear image (Focus), square wave grating 6.1 × 10^4 Rh/rod/sec in 0.2 C/D.*

0.2 c/d

1	2	3	4	5	6	7	8	9	10	11	12	13	14	15	16
17	18	19	20	21	22	23	24	25	26	27	28	29	30	31	32
33	34	35	36	37	38	39	40	41	42	43	44	45	46	47	48
49	50	51	52	53	54	55	56	57	58	59	60	61	62	63	64
65	66	67	68	69	70	71	72	73	74	75	76	77	78	79	80
81	82	83	84	85	86	87	88	89	90	91	92	93	94	95	96
97	98	99	100	101	102	103	104	105	106	107	108	109	110	111	112
113	114	115	116	117	118	119	120	121	122	123	124	125	126	127	128
129	130	131	132	133	134	135	136	137	138	139	140	141	142	143	144
145	146	147	148	149	150	151	152	153	154	155	156	157	158	159	160
161	162	163	164	165	166	167	168	169	170	171	172	173	174	175	176
177	178	179	180	181	182	183	184	185	186	187	188	189	190	191	192
193	194	195	196	197	198	199	200	201	202	203	204	205	206	207	208
209	210	211	212	213	214	215	216	217	218	219	220	221	222	223	224
225	226	227	228	229	230	231	232	233	234	235	236	237	238	239	240
241	242	243	244	245	246	247	248	249	250	251	252	253	254	255	256

Figure 3.27 The Firing patterns of different RGCs/ACs on a projection of blur image (Defocus), Gaussian blur 6.1 × 10^4 Rh/rod/sec in 0.2 C/D.*

3.4.5 Synchrony Pattern and Coupling of OFF-Delayed RGCs with ACs/RGCs

It has been demonstrated that the retina can efficiently communicate the spatial information encoded in spike trains from RGCs to the brain (Masland, 2001). The previous experiments have revealed enhanced firing activity of the OFF delayed RGCs when an image was defocused (Figure 3.18), suggesting that OFF delayed RGCs possibly playing some role in myopia. To answer this question, the possible role of OFF delayed RGCs population in myopia was analyzed. OFF delayed RGCs spikes were evaluated under 525 nm full-field stimulation (light intensity 1311 Rh*/rod/sec; 1 s onset — similar stimulation as used in MEA recordings). It was found that the OFF delayed RGCs, based on delayed response latency of up to 0.3 sec of light responses **(Figure 3.28 A-B).** Later the cell was visualized by Neurobiotin injection and double-labeled with anti-ChAT antibody as a counteracting agent to distinguish the stratification **(Figure 3.28 C).**

To identify the synchronized firing action of cell pairs, cross-correlogram profiles (CCPs) were created for the light-evoked reactions, which revealed associated actions as histogram peaks surpassing chance over the 99% confidence level (Roy, Kumar, & Bloomfield, 2017). To determine spike correlations between OFF delayed RGC pairs that were not time-locked to the light stimulus, data were time reordered by using a shift-predictor procedure, which was then subtracted from the original CCP (Roy et al., 2017).

Dual synchronized firing patterns were seen **(Figure 3.29 A-B)** between OFF delayed RGCs. These dual synchronized patterns were both double peak and single peak, which signifies there are two types of coupled cells: RGC-RGC **(Figure 3.29 A**, **dual peak)** or between RGC-dAC or AC-AC **(Figure 3.29 B, single peak).** Following this one of OFF delayed RGCs was used as a reference cell to map synchronized spatial firing patterns under focused image conditions **(Figure 3.29 C)** and with the

equivalent of a ± 20D defocused image **(Figure 3.29 D, E)**. Only ON/OFF delayed RGC/ACs were plotted. The map revealed the edge of the image spot anticipated on the mouse retina. Hence, the focused image (the image diameter 1.804 mm; spatial frequency is 0 cycle/degree; light intensity 1.6 × 10^5 Rh*/rod/sec) was approximately reflected in the map of the mouse retina. The size of the MEA array used was 100/30 μm. With −20D defocused, the number of OFF delayed RGCs/ACs was significantly reduced. Using the same reference cell, the map of the synchronized firing pattern revealed the area plotted was also significantly reduced (Figure 3.37 D). With a +5D defocused image, no image region could be identified due to inadequate cell responses **(Figure 3.29 E).**

We have repeated this experiment multiple times and in all our experiments we have found that the synchronizations between the cells were significantly decreased when the defocused image is projected, the data can be seen in **Figure 3.30.**

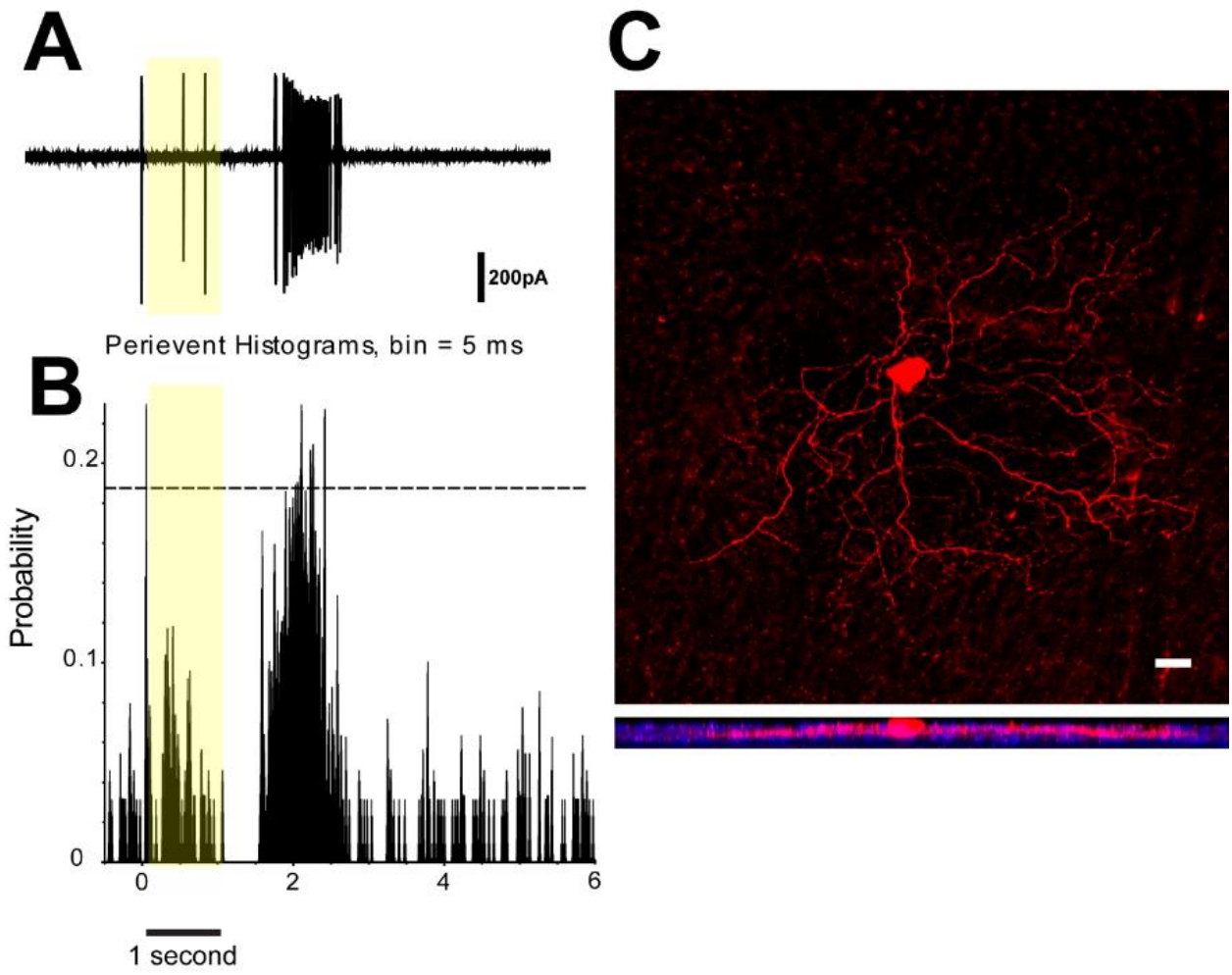

Figure 3.28 OFF delayed RGC light response and morphology. (A) The single-cell recording of OFF-Delayed RGC (525 nm full-field, light intensity 1311 Rh/rod/sec, light stimulation time 1 s). (B)Peristimulus time histogram (PSTH) of cell response. (C) The cell was visualized by Neurobiotin injection (red) double-labeled with anti-ChAT antibody (blue). Scale bar 20 µm, (Banerjee, Wang, So, et al., 2020).*

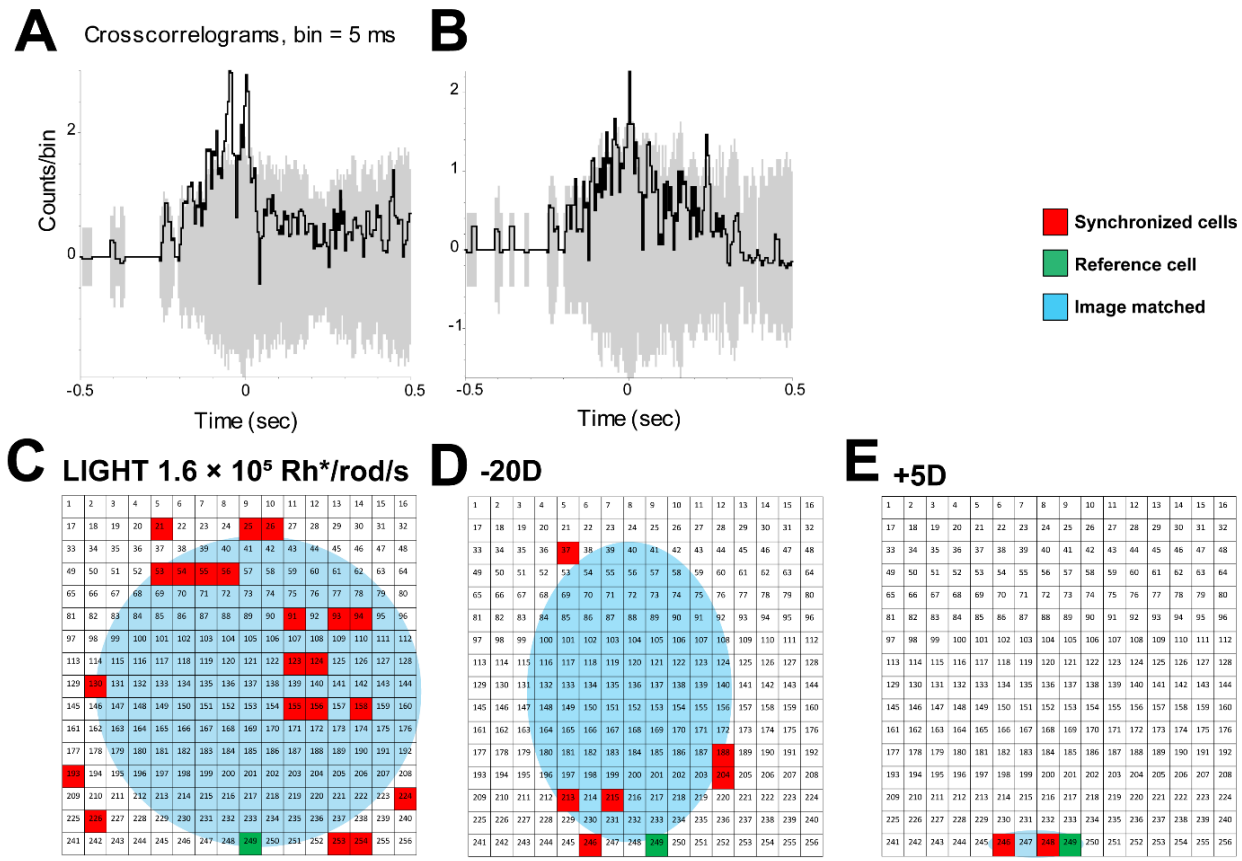

Figure 3.29 Two synchronized firing patterns (A, B) of an OFF-Delayed RGC. (C) Map of spatial firing pattern of the focused image. (D-E) Shown map of defocused image equivalent to −20D and +5D dioptric power. The green-coloured box represents the reference cell, while the Red-coloured boxes represent synchronized cells. The highlighted blue part is the representation of the edge of the image. The grey area in (A & B) showed shift predictor CCP computed from the pairs of OFF-Delayed RGCs/dACs with no coherent firing (Banerjee, Wang, So, et al., 2020).

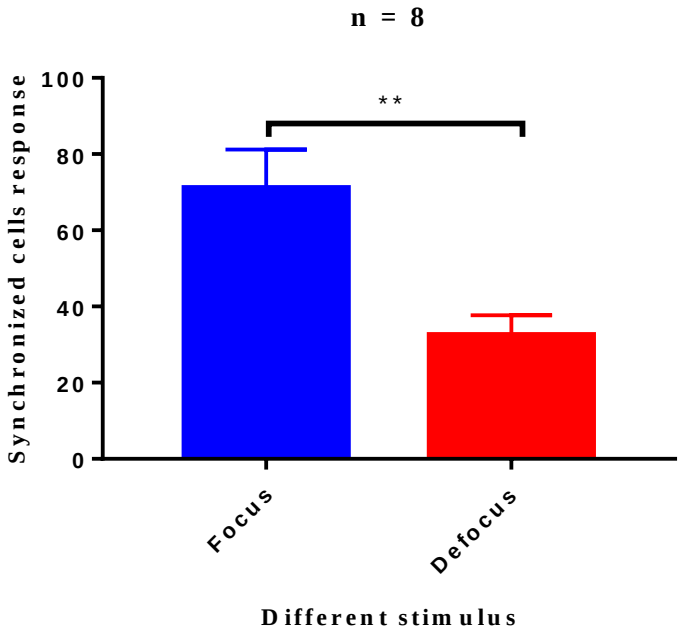

Figure 3.30 summary of the synchronized cell's response under focused and defocused stimulus presentation. (Paired t-test analysis have shown P-value significance of p< 0.01)

3.5 Effects of Dopamine on RGCs/ACs Firing patterns

Dopamine is a crucial neurotransmitter in the retina that helps in refractive development, visual signaling, and retina development. Active functioning of dopamine and dopamine D1 receptors has been identified in myopia development in the mouse retina (Huang et al., 2018; Zhou et al., 2017). The effects of dopamine D1 and D2 receptor agonists and antagonists, on their firing pattern of RGCs in the mouse retina, were tested.

Under 0.2 c/d 5x5 array image projection, D1R and D2R antagonists SCH23390 and Eticlopride, application increased the firing response of RGCs compared to the control on MEA mapping **(Figure 3.31 A/B and 3.32 A/B).** In contrast, D1R and D2R agonists decreased the response compared to the control **(Figure 3.31 C/D and 3.32 C/D).** Following data analysis, the RGC population response was mapped on the MEA map under all conditions, and the number of responding cells were compared with the control recordings.

RGCs (n= 6,804) from 27 mouse retina were recorded. Application of 5 μM D1R antagonist SCH23390 dramatically increased numbers of responding cells with numbers of cell firing in the control retina (n = 342) increasing to 420 in the presence of D1R antagonist SCH23390. Notably, only 11.5 % of cell responses fired in both control and the experimental situation in a similar position **(Figure 3.32 A) (Figure 3.33 A).**

The use of 25 μM D2 receptor blocker, eticlopride, also resulted in increased RGC response with numbers of firing cells in the control retina rising from (n=196) increasing to 363. Once again, the use of an antagonist resulted in only small numbers of cells (13 %) firing under both conditions at the same position **(Figure 3.32 B) (Figure 3.33 B).** The results suggest that the effect of the D1($p>0.05$; not statistically significant) and the D2 ($p<0.03$) antagonists were similar, both increased cell response from the overall population of firing RGCs.

In contrast, D1R agonist SKF38393 (10 μM) was applied to the RGCs responses decreased from 221 in the control 131 (59.2 %) ($p<0.05$). Only 10.3 % of RGCs fired under these same positions **(Figure 3.32 C) (Figure 3.33 C).** Similarly, Quinripole (100 μM) ($p>0.05$) reduced the numbers of RGCs firing in the control from 261 to 109 (41.7 %). Only 7.2 % RGCs population fired in a similar position compared to the control **(Figure 3.32 D) (Figure 3.33 D).** Although there was an increased firing cell response with all D1R and D2R antagonists the altered responses only reached significance for D2R antagonist Eticlopride ($P \leq 0.01$) and D2R agonist SKF38393 ($P \leq 0.05$) as shown in **(Figure 3.33 A-D)**.

Figure 3.34 summarizes the co-localized cell responses from D1R and D2R agonists and antagonists. The response of each group was compared with their respective control data and it was found that the number of co-localized cell responses was relatively higher with D1R and D2R antagonists than the agonists' group.

A 0.2c/d **B SCH23390 5µM**

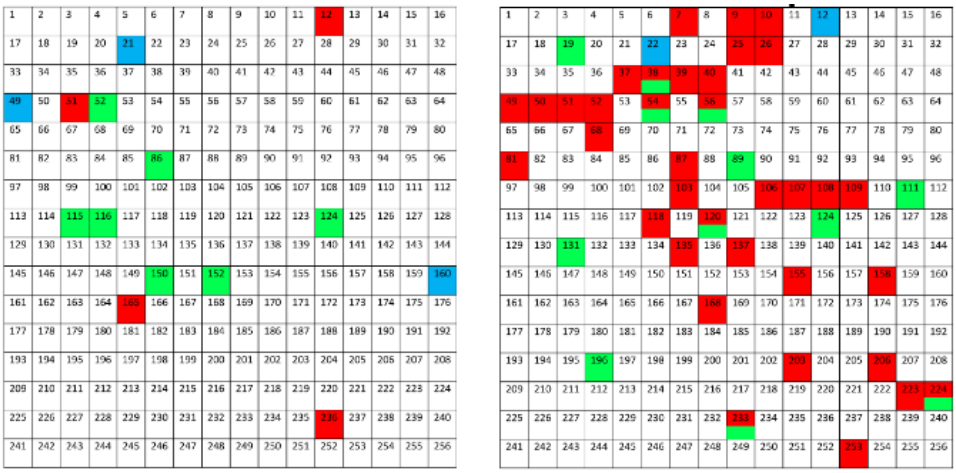

C 0.2 c/d **D SKF38393 10µM**

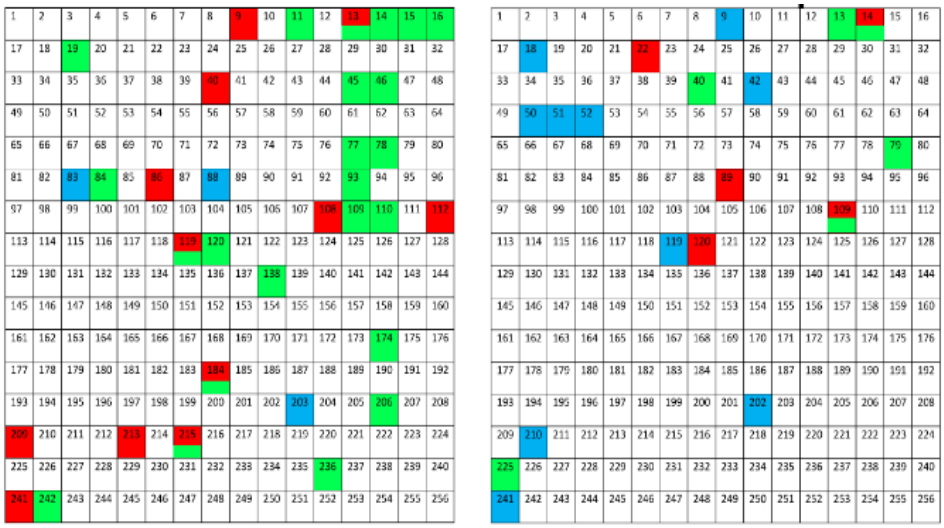

Figure 3.31 Map of firing pattern changes under Dopamine receptors 1 agonist and antagonist application in the mouse retina. D1R antagonist SCH23390 5 µM (A and B) increased firing cells numbers and in opposite, D1R agonist SKF38393 (10 µM, C and D) decreased the firing cell numbers.

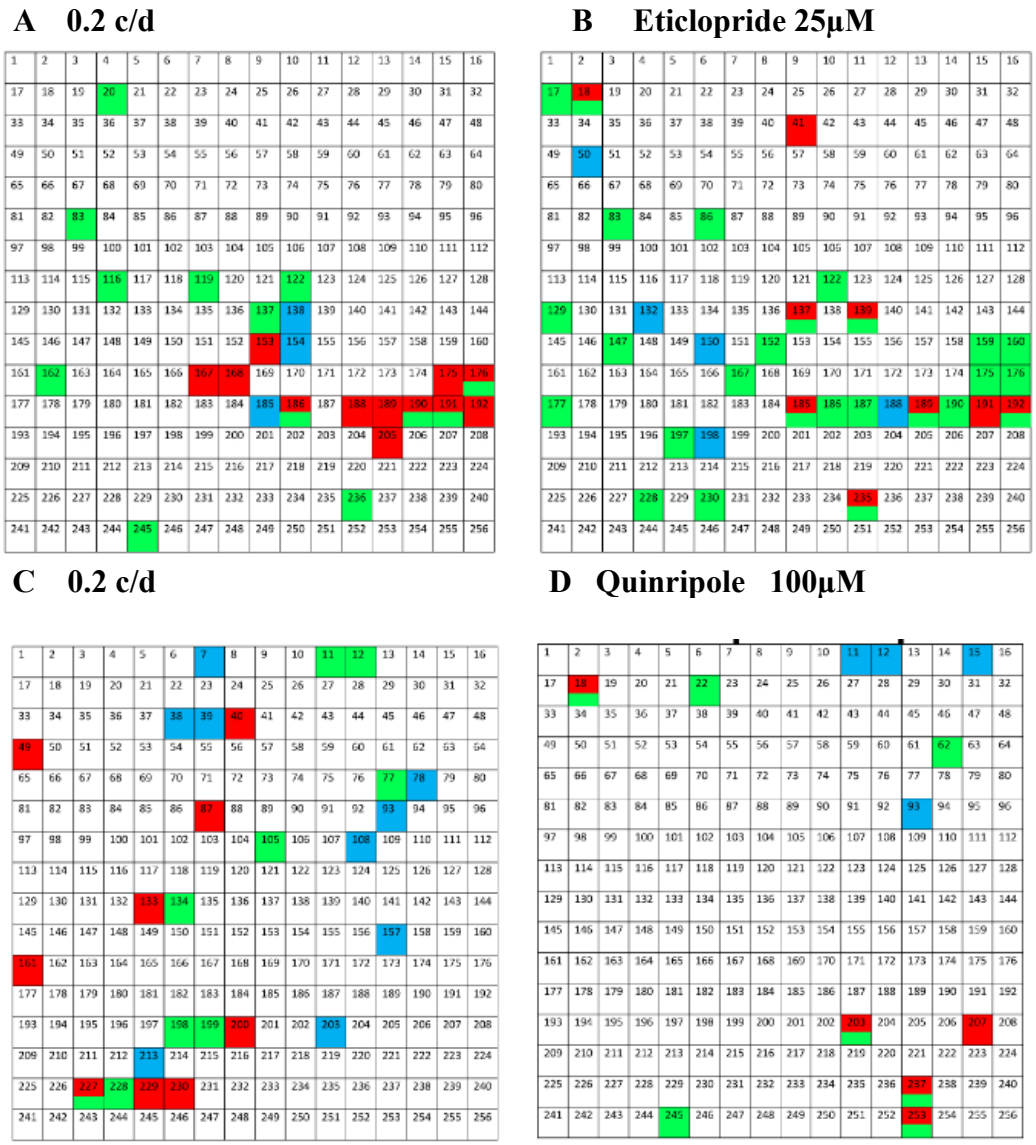

Figure 3.32 Map of firing pattern changed under D2R agonist and antagonist application in the mouse retina. D2 antagonist receptor blocker eticlopride (25 µM) (A and B) increased the cell number firing whereas D2 receptor agonist Quinripole (100 µM, C and D) decreased the firing cells number

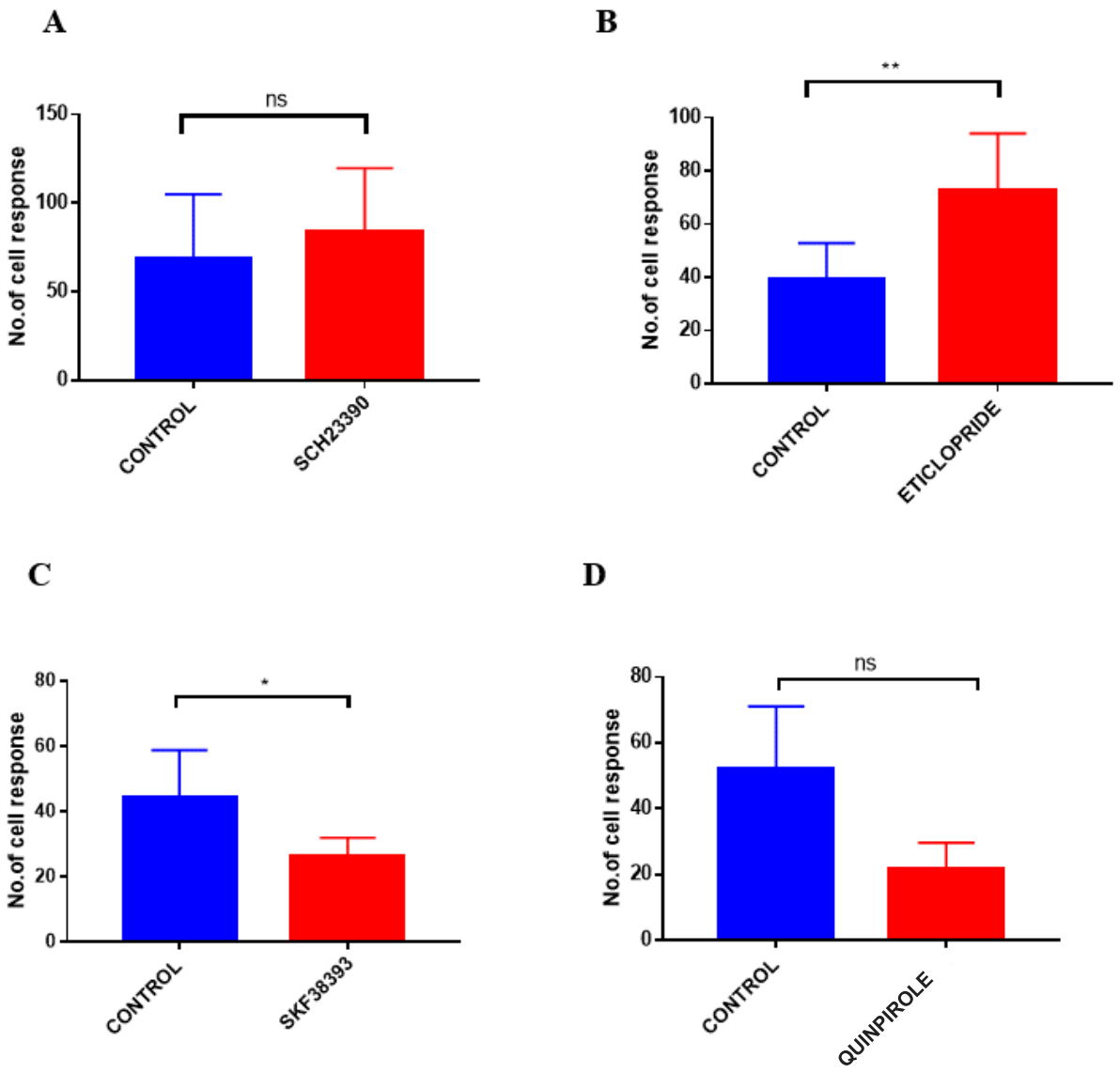

Figure 3.33 (A-D) Summary of the overall firing cell number after different agonists and antagonists of Dopamine receptor 1 and 2 applications. (Paired t-test analysis have shown P-value significance < 0.005)

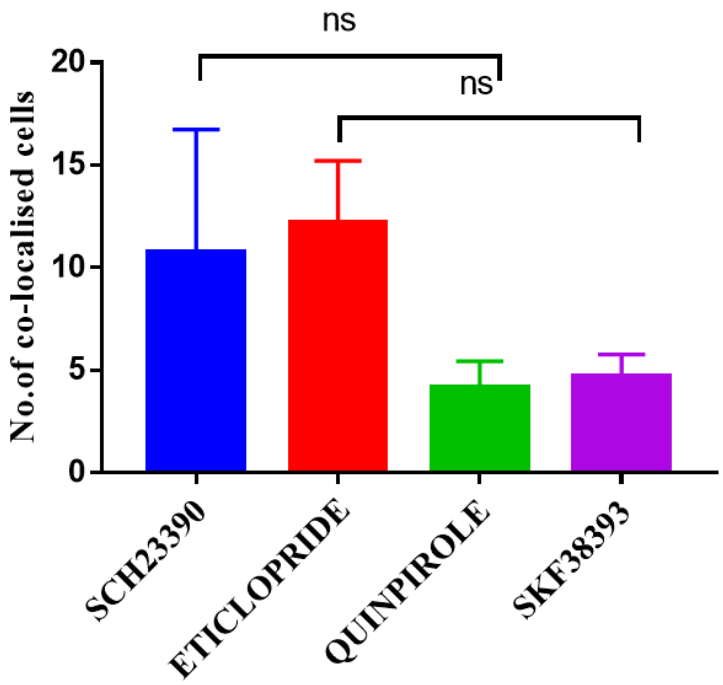

Figure 3.34: A summary of the co-localized cell percentage response with D1 and D2 agonist and antagonist application. Difference between the group is not statistically significant p>0.05, performed with 1-way ANOVA.

3.6 Role Gap junction of AII ACs in the Myopic Mouse Retina

Gap junctions play a pivotal role in signal transmission and neuronal synchronization to encode basic visual knowledge (Deans et al., 2001; DeVries et al., 2002). However, it is unclear whether gap junction expression and coupling are altered in the myopic retina. To determine if this occurs, the expression of Cx36, which is predominantly expressed in AII ACs, was evaluated.

3.6.1 The specificity of anti-Cx36 antibody phosphorylated antibodies in the mouse retina

It is important to understand how signaling from RGCs is delivered to another neuron within the retina or outside the retina. To understand this, expression, and phosphorylation of Cx36, in AII ACs coupling in the vibratome sectioned mouse retina were investigated. 95.4 ± 0.02 % Ser293-P positive puncta were identified in the IPL, co-localized with mCx36-labelled plaques in the (WT) mouse retina (5 retinas × 3 samples =50631 detectable in Ser293-P phosphorylated plaques) (**Figure 3.35 A-C**). Thus, it is proved that the Ser293-P antibody is highly specific in Cx36 as earlier reported (Ivanova et al., 2015). A connexin36 knockout (Cx36KO) mouse retina double-labeled with mCx36 and Ser293-P antibodies, was used as negative control and none of the antibodies showed any punctate staining in the OPL or IPL in the Cx36KO mouse retina (**Figure 3.35 D**). Demonstrated the high specificity of the mCx36 and Ser293-P antibody in the mouse retina.

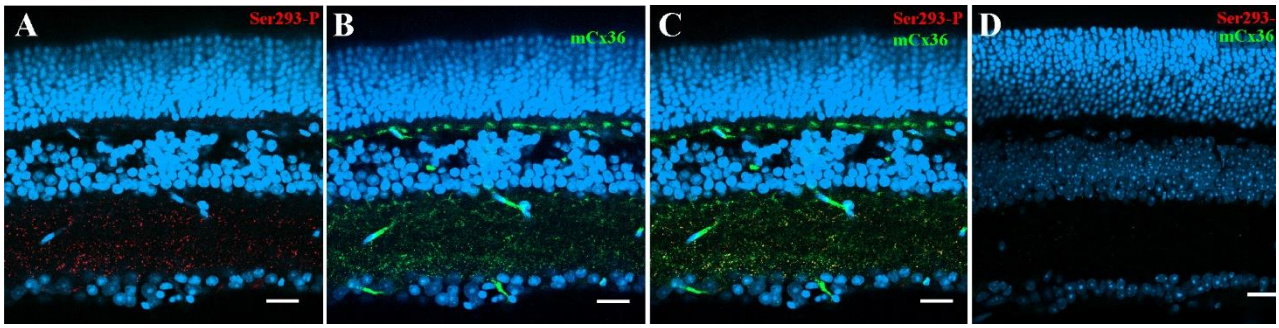

Figure 3.35 Ser293 antibody labeling patterns of the mouse retina sections. (A-C) Phospho-Ser293 antibody labeling pattern in the vertical section of the mouse retina. (A) Ser293-P antibody labeled (red) abundant punctate structures in the inner plexiform layers (IPL) and some in the outer plexiform layer (OPL). (B) Labeling with monoclonal Cx36 antibody (green) shows the labeling of Cx36 also in the OPL and IPL. (C) The merged image of A and B shows multiple plaques identified as Ser-293-P co-localized with Cx36 antibody labeling (yellow). (D) Negative control of Cx36 KO mouse retina the labeled punctate of Cx36 antibody and Ser293-P was absent in both OPL and IPL. Scale bar is 20 µm, Banerjee, Wang, Zhao, et al., 2020.

3.6.2 Change in Connexin36 Phosphorylation in the Myopic Mouse Retina

To compare the Cx36 phosphorylation and expression in the AII ACs changes in the myopic mouse retina; deprivation-induced myopic retinas from WT (control group) mice were examined. A change in the level of connexin36 phosphorylation was observed using the ser293-P antibody to recognize the connexin36 **(Figure 3.36 A- H)**, suggesting that the functional state of gap junctions was changed in myopia. As the expression level of connexin36 were identified in myopic retinas, it was possible to evaluate the density of connexin36-positive plaques, their size, and the percentage of Ser-293 of Cx36 phosphorylation and further compare the deprivation-induced myopic retinas and control groups.

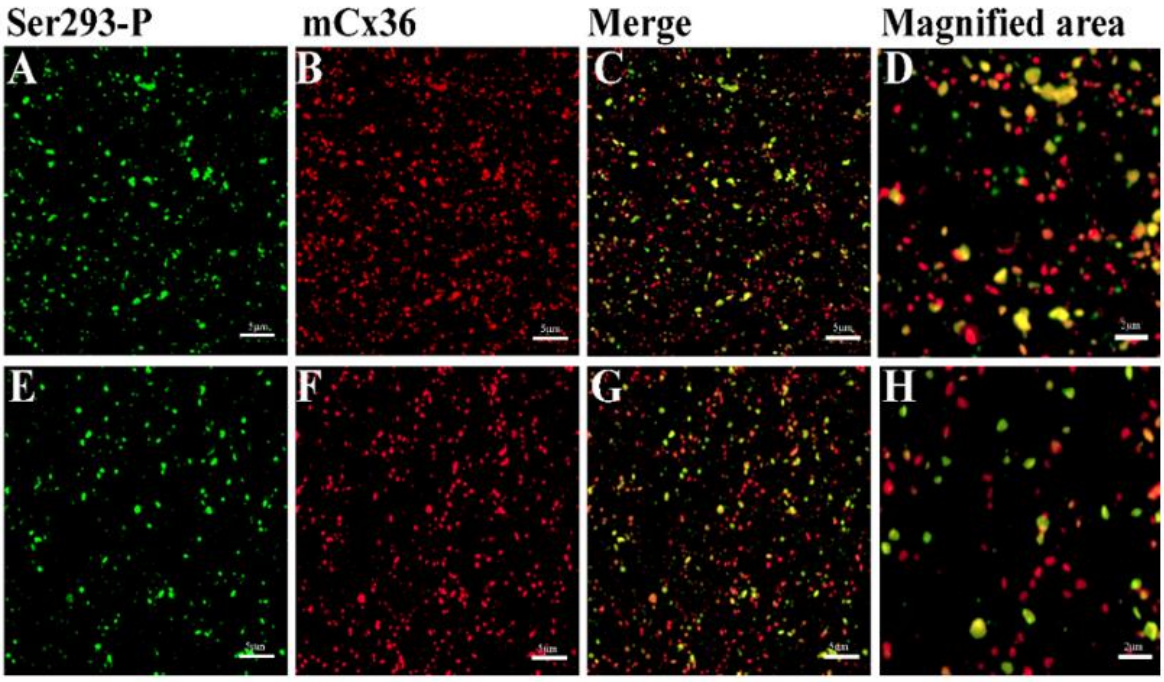

Figure 3.36 (A-D) Phospho-Ser293 antibodies specifically recognize Cx36 in the whole mount of the myopic mouse retina. Confocal stack sections in stratum 5 of the IPL of the myopic mouse retina: mCx36 labeled in red and its phosphorylated form, Ser293-P (green) are present with similar punctate labeling. The magnified areas show the merged images of phosphorylated Cx36, reflected by yellow color. (E-H) The phospho-Ser293 antibody recognizes Cx36 in the control mouse retina. Images are 2 µm deep stacks. Scale bar: A-C and E-F: 5 µm; D and H: 2 µm, Banerjee, Wang, Zhao, et al., 2020.

The results of quantification analysis of ser-293 P demonstrated that there is a significant change in the density of Ser293-P plaques found in WT [284 ± 12 per 10^3 µm^2 (means ± S.E.M.), n = 8] and myopic mouse retinas (377 ± 27 per 10^3 µm^2, n = 8, *p* =0.017,) **(Figure 3.37 A)**. A significant change was also observed in the size of Ser293-P plaques between the WT (WT 0.341 ± 0.003 µm^2) and myopic retinas (0.372 ± 0.004 µm^2; p=0.012) **(Figure 3.37 C)**. An increase in the density of Ser293-P plaques in myopic retinas indicates an increased number of Cx36 phosphorylation in the myopic retina compared to the control. There was also an increase in the size of Ser293-P plaques in myopic

retinas, which indicates that there was more labeled phosphorylation of Ser293-P in Cx36 compared with the control.

A total of 14,773 individual plaques in 8 myopic mice retina and 12,679 plaques in 8 WT (control group) mice retinas were examined, and the results were compared. There was a significant difference (p=0.036) in the Ser293-P phosphorylation rate of Cx36 **(Figure 3.37 B)**. 77.5± 0.03% (means ± S.E.M., n = 8) of connexin36 plaques were phosphorylated in the WT (control group) mice retinas, in contrast to myopic retinas, in which 92.1± 0.04% (n = 8) of the plaques had detectable phosphorylation.

However, no significant difference in the density of mCx36 plaques observed between WT [369± 16 per 10^3 μm^2 (means ± S.E.M.), n = 8] and myopic mice (392 ± 24 per 10^3 μm^2, n = 8, p =0.674) **(Figure 3.37 A).** Neither any changes observed in the size of mCx36 plaques, with 8 mice of 17,244 present in myopic retinas and 8 mice of 14,516 in WT mice retinas; (WT mice 0.412 ± 0.002 μm^2; myopic mice 0.414 ± 0.003 μm^2; p = 0.362) **(Figure 3.37 C)**. Overall, it can be demonstrated that Ser293-P increased both in size and density of the phosphorylation status of Cx36 in the myopic mouse retina.

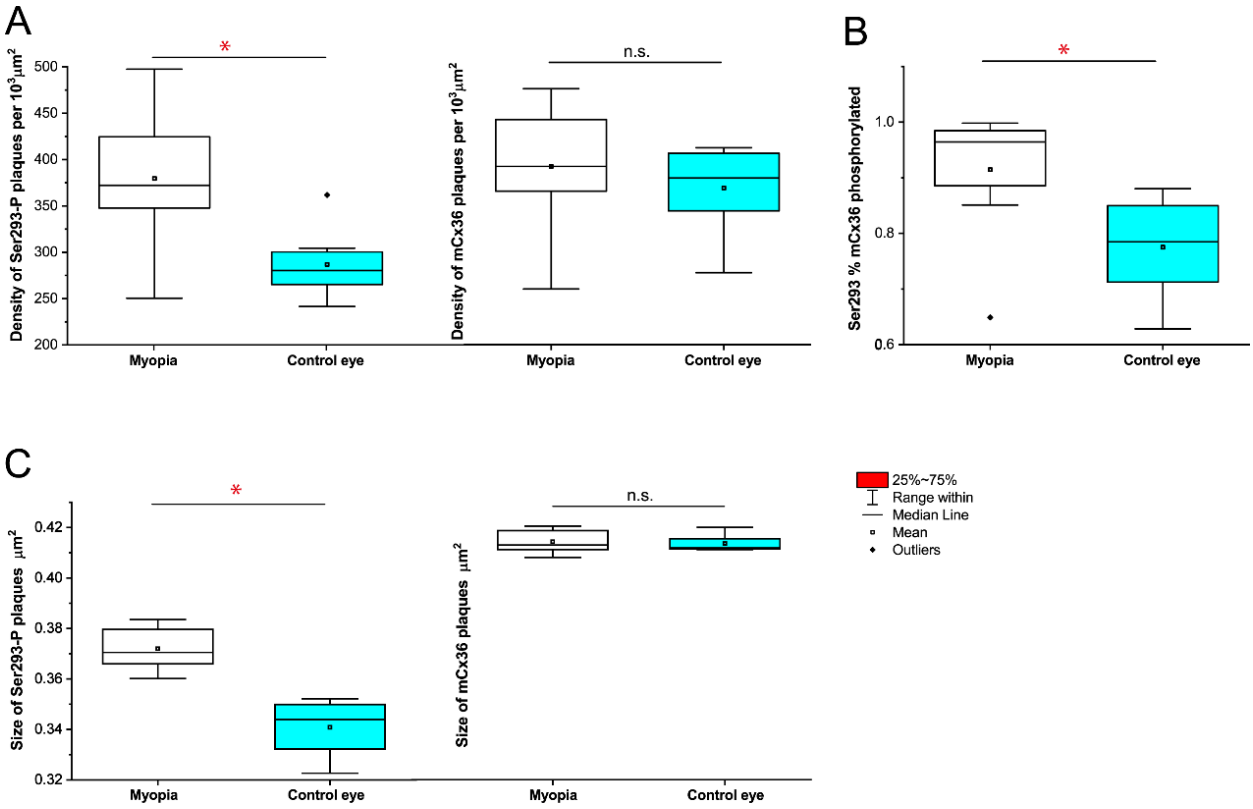

Figure 3.37 Quantification of phosphorylation of Cx36 gap junctions in AII amacrine cells in mouse myopic retinas. The data are presented as averages; Error bars are presented as SEM. Significance is based on Wilcoxon Signed Ranks Test. Where ∗ $P < 0.05$, n.s. $P > 0.05$, Banerjee, Wang, Zhao, et al., 2020.

3.6.3 Dopamine receptors can affect the coupling of AII ACs in the myopic retina

In myopic retinas, a downregulated dopaminergic synaptic pathway was noticed earlier (Zhou et al., 2017). The coupling between AII-AII Amacrine cells is modulated by dopamine signaling (Hampson, Vaney, & Weiler, 1992; Kothmann et al., 2009). Therefore, it is important to see the effect of dopamine and its receptors on AII ACs coupling in the mouse retina. The quantitative comparison of the tracer coupling pattern of AII ACs with an agonist and antagonist of the D1R application was evaluated in the mouse retina and it has been observed that the coupling of AII ACs has significantly increased ($P<0.01$) with D1R antagonist (SCH23390, 5 µm) application **(Figure 3.38 D)** compared with the control group and those with the D1R agonist (SKF38393, 10µm) application can be seen in **(Figure 3.38 E).**

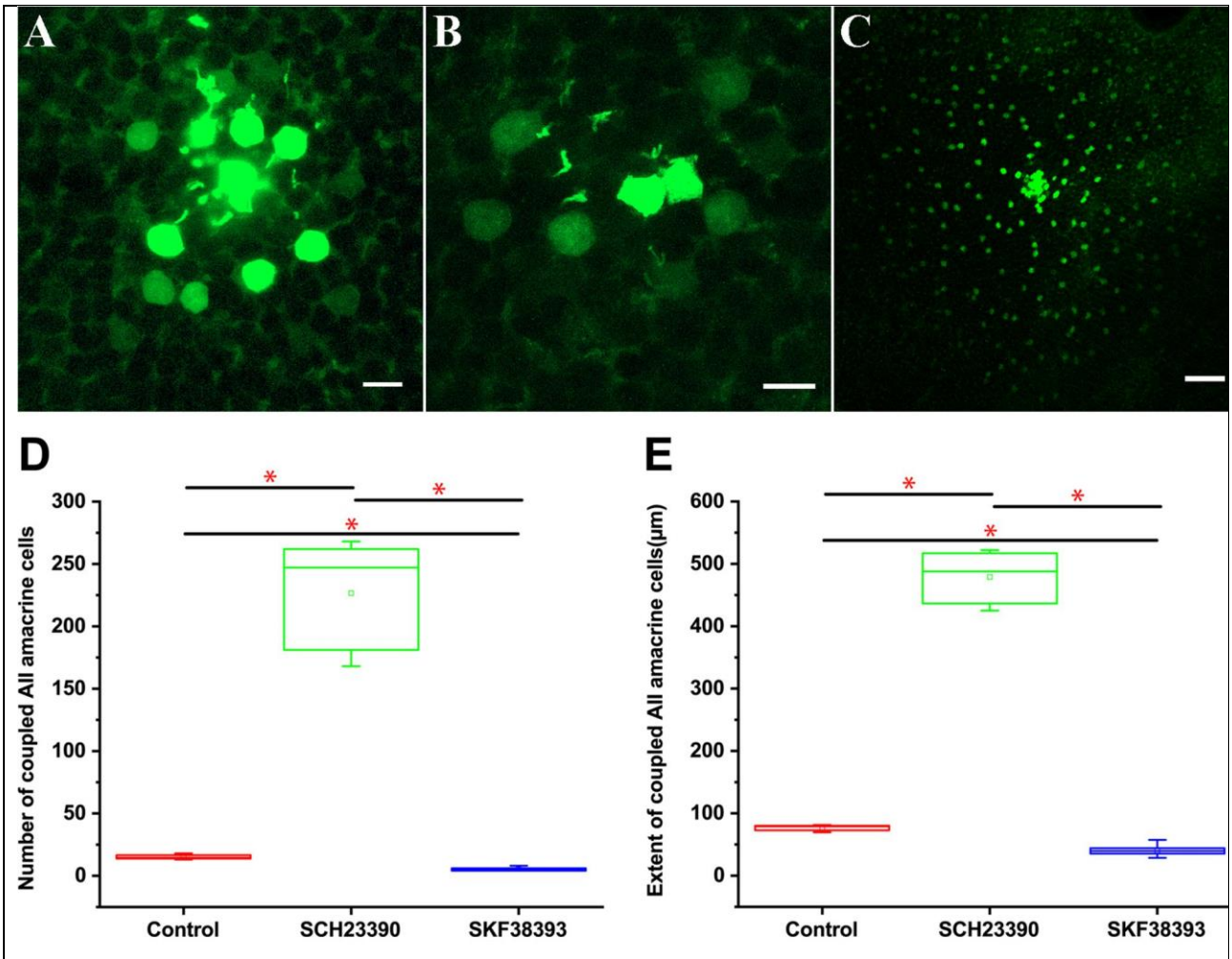

Figure 3.38 showing the quantitative comparison of trace coupling between AII AC changes after dopamine receptors agonist and antagonist application. ***(A).*** *Flat mount view of a group of tracers coupled AII ACs in the mouse retina following injection of one cell with Neurobiotin.* ***(B).*** *D1R agonist SKF38393 10 µM reduced the extent of Neurobiotin diffusion in AII ACs coupling.* ***(C).*** *D1R antagonist SCH23390 5 µM dramatically increased the tracer coupling of AII ACs.* ***(A-C)*** *Planes of focus are on the AII cell somata in the proximal inner nuclear layer. Scale bar: (A and B): 10 µm; (C): 50 µm.* ***(D):*** *Box graph showing the difference in the number of coupled AII ACs with D1R agonist SKF38393 10 µM and D1R antagonist SCH23390 5 µM application There was a statistically significant difference (asterisk, P < 0.01) in the number of coupled AII ACs.* ***(E).*** *Box graph showing the difference in the extent of coupled AII ACs somata with the D1R agonist SKF38393 10 µM and D1R antagonism SCH23390 5 µM application There was a statistically significant difference (asterisk, P < 0.01) in the number of coupled AII ACs (Banerjee, Wang, Zhao, et al., 2020).*

Part of section 3 (Chapter 3: Results) is published and * Reproduced with permission:

(1). BANERJEE, S., WANG, Q., ZHAO, F., TANG, G., SO, C., TSE, D., TO, C.-H., FENG, Y., ZHOU, X. & PAN, F. 2020b. Increased Connexin36 Phosphorylation in AII Amacrine Cell Coupling of the Mouse Myopic Retina. *Frontiers in Cellular Neuroscience,* 14.

(2). BANERJEE, S., WANG, Q., SO, C. H. & PAN, F. 2020. Defocused Images Change Multineuronal Firing Patterns in the Mouse Retina. *Cells,* 9**,** 530.

CHAPTER 4 Discussion

4.1 The Animal Model

Animal model studies have provided important insight into the field of refractive development (Wiesel & Raviola, 1977). In monkey models, myopia is induced by the lid suture method, which allowed us to understand more about the optical and biological basis of myopia, and subsequently more experimental models using a variety of other animal species to induce myopia were explored. They include chickens (Osol, Schwartz, & Foss, 1986; Yinon, Rose, & Shapiro, 1980), monkeys and marmosets (Tigges et al., 1990; Troilo & Judge, 1993), the tree shrew (McBrien & Norton, 1992; Sherman, Norton, & Casagrande, 1977), rabbits (Tokoro, 1970), cats (Gollender, Thorn, & Erickson, 1979), guinea pigs (Howlett & McFadden, 2006) and mouse (Barathi et al., 2008; Faulkner, Kim, Iuvone, & Pardue, 2007; Schaeffel et al., 2004; Tejedor & de la Villa, 2003).

Mouse models have contributed to an extensive range of scientific advances for several visual and neurological disorders and have permitted scientists to focus on fundamental questions that were troublesome to approach with other experimental models.

The mouse is the most widely used mammalian model for biomedical research because of its similarity in genetic composition with humans. Conventional genetic and targeted gene engineering approaches have yielded many mouse models that duplicate key features of human genetic conditions, including eye disease (Krebs et al., 2017).

Hence, the mouse myopia provides a piece of excellent knowledge to study refractive development for mammalian eye growth and human refractive development (Schaeffel, 2008; Christine Schmucker & Frank Schaeffel, 2004).

Several studies (Barathi et al., 2008; Pardue et al., 2013) have previously mentioned that mouse models offer several advantages over other animals in studying refractive errors. Mouse models have provided important insights into disease mechanisms (Krebs et al., 2017) and are used as a resource for preclinical studies and the development of therapeutic interventions. Experimental mouse models have the following advantages: (a) Mouse model has similar sclera and fibrous tissue structure to humans (Barathi et al., 2008; Pardue et al., 2013) (b) It is the most extensive and widely studied mammalian model for human diseases (Justice, Siracusa, & Stewart, 2011) and (c) The transgenic and mutant mouse provides an additional opportunity to test the functional pathways to refractive development (Pardue et al., 2008).

However, the use of a mouse model does have some limitations, including small eyeball size, poor optics, large lens, and considered as a nocturnal animal with no fovea. Also, mice have only blue and green cones. However, the advantages outweigh these limitations; hence the mouse model continues to be predominantly used in eye research.

In the refractive development process, retinal signaling plays an important role by mediating the retina-to-sclera signals, leading to myopia development (Park et al., 2013; Stone et al., 2013). In this study, a mouse experimental model was used to induce myopia. The results of this study can help determine the retinal signaling mechanisms involved in refractive development.

4.2 The Myopia Refraction Model

The onset of myopia development remains unclear, despite being a global public health issue that can result in severe visual disability if left uncorrected (Pardue et al., 2008). The development of the myopia model in different species has shown many significant findings in ocular parameters and refractive status of the eye (LAUBER, 1991; McBrien & Norton, 1992; Schaeffel et al., 2004; Troilo & Judge, 1993).

In the present study, the lid suture model method was successfully used in C57/BLJ6 mice to induce axial length elongation and myopia refractive development after 6 to 10 weeks of lid suture. Results from induced myopia mice showed that the average AL increased in the experimental eye, which is approximately equal to 27D of defocus, as in the schematic model of mouse eye axial elongation of 5.5 to 6 μm can induce 1 dioptre (D) of myopia (Christine Schmucker & Frank Schaeffel, 2004). Under this lid suture method, the myopia induction success rate was only 42.3% due to factors such as cataracts or corneal and lid scarring, while some died during the experiment. Also, myopia less than 5D were excluded from the study. The success rate can be improved with more care time attending regularly on sutured lids to repair loose stitches and resuture on time, when necessary.

Using photorefraction, statistically significant average refractive power differences of -3.502D, -3.613D, and -4.978D myopic shift were observed between the control and sutured eye in 6, 8, and 10 weeks, respectively. The changes in the axial length were similar in trend with previous studies performed using a mouse model (Barathi et al., 2008). Although the refraction data from photorefraction and streak retinoscopy has shown some differences that can be due to the selection of different time periods, a smaller number of sample sizes, and individual genetic factors between animals.

Streak retinoscopy measurements are generally reported as more hyperopic than IR photorefraction in earlier studies (Pardue et al., 2008; Schaeffel et al., 2004). The difference of refractive power measured in retinoscopy vs photorefraction has shown an average difference ranging from 2D to 6D change in previous studies (Barathi et al., 2008; Pardue et al., 2008; Schaeffel et al., 2004; Zhou et al., 2008). The results from this study are also found inconsistent with the previous studies. Mouse eyes are very small, the amount of hyperopia measured can result from the artifact. As the retinoscopy reflex perceived while performing refractions originate from the inner limiting membrane layer of the retina, making the eye length shorter (Glickstein & Millodot, 1970).

One of the major limitations of this experiment was the success rate of the myopic mouse model, as it was very difficult to maintain the lid sutures intact for the whole experimental period. Which could be the reason for lesser degrees of myopia development? Another major limitation was the post-surgical complications which have resulted in the exclusion of a huge number of data leading to lower sample size. We also believe that complications such as corneal scars and lid swellings may cause inconsistency in the refractive power calculations with the streak retinoscopy when compared to the IR photorefraction and axial length.

From our unpublished data, it has been proven that myopia can be induced successfully with a success rate increasing up to 50% with a better surgical technique. Although challenges remain with surgical complications but with proper care and technique this can be achieved. A standardized suturing technique design is much needed for successful myopia development in mouse models.

4.3 RGCs firing pattern changes with different light intensities

A previous study (Pan, 2019) suggests that different light intensities could change the firing pattern of RGCs, and the recorded threshold sensitivity of the ON and OFF alpha RGCs was found to be 10-20 Rh*per rod per second. Recording the RGCs response with MEA by projecting 20 Rh*per rod per second of light intensity, we have identified five major types of cell responses that were identified based on the firing pattern of their light-evoked potentials.

It has been previously reported (Pan et al., 2016) that RGCs have specific responses for different light intensities and, can be classified into high sensitive (HS), low-intermediate sensitive (LIS), intermediate sensitive (IS), and low sensitivity (LS) RGCs. LS is corresponding to the threshold of the cone photoreceptors with the highest peak threshold sensitivity at ~20 Rh*/rod/sec and considered as purely cone driven response (Deans et al., 2002; Pan et al., 2016; Völgyi, Deans, Paul, & Bloomfield, 2004). Therefore, we used the same threshold intensity to record the cell response from the RGCs layer and further segregated them into 5 different types based on their response to light-evoked potentials. The electrical coupling between RGCs helps in synchronizing their light-evoked signals which are believed to compress information for more effective communication, thereby enabling more information to be transferred through the optic nerve to the central nervous system (Bloomfield & Völgyi, 2009).

Several factors can affect the recording of RGCs with different light intensities among which dark adaptation plays a key role. It is very important to maintain the animal dark adaptation prior experiment, as light causes bleaching of visual pigments and can affect the recording (Ebrey & Koutalos, 2001). There are few challenges while preparation of the retinal tissue, among which vitreous strand removal is one, and we believe is the most important part of the experiment. Because vitreous strands can cause noise while recording the signal with poor contact between the retinal

tissue and the electrode. Therefore, a well-prepared retinal tissue and dark-adapted retina are necessary for successful recording from the RGCs.

4.4 Myopic vs Non-myopic RGCs firing pattern.

Visual functions including visual acuity (Strang, Winn, & Bradley, 1998), contrast sensitivity (Liou & Chiu, 2001), and grating acuity (Atchison, Schmid, & Pritchard, 2006) are negatively affected in the myopic eyes (Wolsley et al., 2008).

Several clinical studies have also reported an increased risk of abnormalities and structural changes to the sclera, choroid, and retina in high myopes (McBrien & Gentle, 2003; Rada, Shelton, & Norton, 2006; Rymer & Wildsoet, 2005). A study employing form-deprived myopia models have also shown a direct association between structural changes with myopia (Beresford, Crewther, Kiely, & Crewther, 2001; Liang, Crewther, Crewther, & Barila, 1995). In the present study, the firing pattern of RGCs under focused and defocused images in the myopic mouse retina were investigated and compared with a matched control. There were no significant changes in the firing of cell responses were seen under different focused and defocused image projections between the control and myopic retina.

The results from this study demonstrated that the firing response number of RGCs in the myopic eye decreased significantly as compared to the matched control in all the stimulus conditions such as clear and blur but the results were not statistically significant. This is maybe due to the amount of myopia induced by the lid suture model was insufficient to induce functional and structural changes. Which has served as one of the major limitations of this study. 4 mice with average AL of 3.55mm to 3.6mm were used, which can contribute to 16D to 19D defocus according to the schematic mouse eye model.

However, we do not know whether this amount of change in defocus can result in structural or functional changes in the mouse model or not. We also think that the lesser sample size is a contributing factor to the significance level of the result. Better suture technique and larger sample size studies are needed. We also know that Lid suture can cause flattening of the cornea, and thus the overall axial length of the eye also increases, and possibly there will be no change in the retinal structures.

Clinical studies have reported that myopia >6D can increase the risk of chorioretinal abnormalities (Saw, Gazzard, Shih-Yen, & Chua, 2005) and pathological changes. Studies on human subjects have shown significant changes in the RGC and IPL profiles (Seo et al., 2017) but such structural or functional changes in the form-deprived mouse model have not been reported. Future studies of the morphological changes in the ganglion cell layer of the myopic retina are wanted.

4.5 Effects of Defocused images on the signaling and firing pattern of RGCs.

Optical defocus is the first trigger of myopia development, which is largely governed by the retina (Maiello et al., 2017). Although the aetiology of myopia development remains unspecific, it is proven that image blur alters eye growth; hence the refractive status of the eye (Smith III & Hung, 1999). However, reports on the exact effect defocus has on RGC signaling refractive error changes or emmetropization is still limited. A previous study using chicken retina (Bitzer & Schaeffel, 2002) showed that defocus manipulates eye growth through the expression of ZENK. Other studies have reported that retinal signals facilitate the eye's refractive development through a retina-to-sclera signaling pathway (Harper & Summers, 2015; Smith, Hung, & Arumugam, 2014). In the current study, it was observed that defocused images change murine RGC signaling, which may act as the crucial step in this retina-to-sclera signaling mechanism.

ON and OFF responses are the two most important visual elements encoded by RGCs in the parallel information processing of the retina (Asari & Meister, 2012; Gjorgjieva et al., 2014). Defocused images, irrespective of whether the retina senses these changes, will change the size, focus plane, and light intensity, compared to a focused image, but it is uncertain whether the retina can sense this change or not (Pan, 2019).

In the current study, changes in the RGCs firing patterns were noted with different dioptric powers of defocus recorded with MEA. ON, OFF, ON-OFF RGCs, and OFF-delayed RGCs were observed to change their firing pattern and their response numbers. Interestingly, responses from OFF-delayed RGCs were identified more with the application of defocus of different dioptric powers compared to focused. Similar results were seen on the projection of defocus images of 0.5 c/d, when the 0.5 c/d images were projected on the retina and shown again after a different spatial frequency image of 0.2 c/d had been projected, the retina showed a similar firing pattern as before. This suggests that the retina can understand an image change of different spatial frequencies and RGCs can respond

accordingly to different stimulation patterns. Even though the similar spatial frequency image did not produce the exact firing pattern as earlier, it maintained a similar pattern in all trials **(Figure 3.23 & 3.24)**. For example, in **(Figure 3.20 and 3.22)**, in **figure 3.20** cell numbers 123, 119, and 120 in the map represent OFF- Delayed response in 0.5c/d but changes to ON/OFF, OFF, and ON- Delayed response when 0.5 c/d images again repeated. This suggests that the retina has a complex process to code and identify image similarities or perhaps the MEA electrode picks up the signal from the same cell's soma or dendrite in the receptive field but that it is shown in another electrode of MEA. A previous study mentioned that pattern adaptation is found to be the clever functions of the neural circuitry and possibly RGCs playing a major role in it (Gollisch & Meister, 2010).

The current results differ from those reported in the chicken retina, which showed no difference in the response pattern on defocused images (Diedrich & Schaeffel, 2009). This may be due to differences in species examined.

4.6 Synchronization pattern of OFF-Delayed RGCs changes with Defocus.

In the present study, dual synchronizing firing patterns among the OFF delayed RGCs (dual peak but less than 400 µm distance and OFF delayed RGCs coupled ACs (single peak) were observed. It has been shown that single spikes can code significant information about visual stimuli and the retina can rapidly and dependably code spatial information by neural population with relative spike latencies (Gollisch & Meister, 2008; Meister & Berry, 1999). It is possible that these coupled ACs could be polyaxonal ACs or wide-field ACs which cover extended space (Bloomfield & Volgyi, 2007; Volgyi, Xin, Amarillo, & Bloomfield, 2001). OFF delayed RGCs may synchronize with other delayed RGC/dAC to describe the edge of an image area.

However, it is important to note that OFF delayed RGCs lost their synchronous firing pattern when a defocused image was projected. As a result, retina neural population spikes signified that a defocused image reduces the synchronized firing response of the OFF delayed RGCs. Based on the synchronized firing pattern of the OFF-Delayed RGCs we have repeated the experiment several times and have found a similar response of reduced synchronization of OFF-Delayed RGCs with defocused images. Therefore, it will be crucial to study OFF-Delayed RGCs in future studies.

In a previous study, it was noted that ON-OFF RGCs allow multiple efficient neural coding, which can offer a superior mechanism for obtaining information (Gjorgjieva et al., 2014). Bistratified ON-OFF RGCs may be an advantage over regular ON/OFF RGCs. In this study, ON-OFF RGCs had different response cells percentage to different defocused images **(Figure 3.9, 3.11-3.15)**. Thus, it can be concluded that ON-OFF RGCs can identify and analyze information from focused and defocused images.

4.7 Dopamine excites RGCs /ACs firing pattern response.

Dopamine is involved in the signaling cascade in the retina that regulates eye growth during visual development (Feldkaemper & Schaeffel, 2013). Dopamine produces its effect via two families of D1 and D2 receptors. In this study, D1 and D2 agonists and antagonists were used to evaluate the changes in the firing pattern of RGCs. It has been reported that agonists inhibit myopia, whereas antagonists can stimulate it. Not all authors found this statement true, there are several pieces of evidence which state that dopamine can stimulate the diffusor wear than the negative lens wear (Feldkaemper & Schaeffel, 2013).

In the previous study, dopamine D1 receptor agonist and antagonist used caused variations in trace coupling of ACs-RGCs, RGCs-RGCs, and AII-AII ACs (Banerjee, Wang, Zhao, et al., 2020). When D1 and D2 receptor antagonists were used the RGCs fired dramatically in increasing order, whereas, in the presence of agonists, responses were reduced. This indicates that dopamine, via both its receptor types, manages RGC's excitability to initiate spiked responses. However, in this preliminary data, it is unclear how dopamine causes changes in the firing pattern of RGCs mechanics. Both dopamine agonists and antagonists were applied to the RGCs layer into the MEA chamber and signals were recorded which is a different methodology as compared to the previous studies reported on the effects of dopamine. Therefore, it would be an important step to investigate the functions and implications of the dopamine via its both receptor under different stimulus conditions and comparing it.

Dopamine and dopamine D1 receptor play key roles in myopia development in the mouse retina (Huang et al., 2018; Zhou et al., 2017), and dopamine is closely related to myopia development, but their effects need to be carefully investigated so that it can be used in a translational research method for studying the control of retinal signaling in the myopic retina.

4.8 AII amacrine cells function in retinal signaling

Amacrine cells play a key role in increasing RGCs signaling and reducing background noise (Pan, 2019). AII ACs are the most abundant types of ACs present in the vertebrate retina. AII ACs coupled with Cx36 is present in the rod and cone pathways to segregate signals to their respective ON and OFF pathways (Bloomfield & Völgyi, 2004). Dopamine signaling modulates the coupling between AII-AII ACs (Hampson et al., 1992; Kothmann et al., 2009). Cx36 is the predominant subunit of gap junctions in AII ACs (Feigenspan et al., 2001). Phosphorylation of Cx36 promotes gap junction coupling (Kothmann et al., 2012). In this study, a major finding demonstrated increased phosphorylation of connexin36 in AII ACs in mouse myopic retinas. The size and density of Ser293-P have also been shown to increase in the mouse myopic retinal model, which relates to the role. Ser293-p antibody plays in recognizing the phosphorylated form of Cx36 (Ivanova et al., 2015).

It is known that gap junction plasticity contributes to the communication and processing of visual information to the higher centres (O'Brien & Bloomfield, 2018; O'Brien., 2014), so gap junctions in AII ACs may be compensated at a certain stage of myopia, leading to increased Cx36 phosphorylation, and coupling to improve the visual information under a defocused state (Figure Appendix 7.3). Gap junctions are considered regulators of oscillations and provide precise visual signaling transportation to the downstream network system (Pernelle, Nicola, & Clopath, 2018). It can be assumed that defocused images in myopia are noisy and transmit additional visual information downstream compared to focused images. Thus, more coupling of AII ACs or functional gap junctions (Cx36) may be necessary to filter noise. Some studies have suggested that pharmacological agents can be used to adjust phosphorylation (Kothmann et al., 2007; Kothmann et al., 2012). It is also well known that dopamine D1 receptors affect the coupling

between AII amacrine (Banerjee, Wang, Zhao, et al., 2020). In the emmetropic retina, reduced dopamine release from dopaminergic amacrine cells combined with the dopamine receptor(D1R) finally resulted in the dephosphorylation of Cx36. However, in myopic retina defocused image generates more noise in the signaling leading to increased phosphorylation of Cx36 in AII ACs coupling to filter out maximum noise. It has been observed that the dopamine level decreases to adapt to the defocus state as a certain phase of myopia (Feldkaemper & Schaeffel, 2013). Therefore, we may assume that AII ACs can actively make compensation to focus and defocus status through its electrical and chemical synapses and might play a crucial role in the visual process in the myopic mouse retina.

CHAPTER 5 Conclusion

In this study, we have investigated the effects of defocused images on the RGCs signaling in the mouse retina. We have also investigated the basic firing pattern of RGCs signaling in the myopic mouse retina. Also, the functions of gap junctions coupling between AII ACs in myopia and the effect of dopamine and its receptors on AII ACs in myopic mouse models were studied.

The mouse myopia model is excellent for inducing deprivation myopia model even though the overall success rate was less than <50%, regular follow up and close examination of suture condition can help in achieving better success rates. Deprivation myopia in mice is challenging but it can be induced significantly with longer treatment periods and better technique.

The study has shown that the RGCs in the retina can respond diversely to focused and defocused images at both single-cell and multiple cellular levels. These neuronal response mechanisms can be the trigger sites from the retinal to the scleral signaling pathway. We have also shown that a defocused image reduces the synchronized firing response of the OFF delayed RGCs which is one of the major findings of this study. It can be assumed that OFF-Delayed RGCs maintain synchrony patterns with other delayed RGCs or dACs to define or appreciate the edge of an image. Therefore, the functional changes of the OFF-Delayed RGCs and their synchronous pattern concerning different degrees of defocused images will be investigated in future studies.

Furthermore, we have also studied the expression and phosphorylation of Cx36 in the myopic mouse model. It was observed that the phosphorylation of connexin36 significantly increased in AII ACs in mouse myopic retinas, which may indicate increased gap junction coupling of AII ACs is plausible

in myopia. Besides, the effects of dopamine and both of its receptors type have shown excitations in RGCs firing responses.

Overall, our results suggest that retinal signals may play the first step in inducing myopia and a key signal in triggering the development of myopia. This study has also identified the gap junctions between AII ACs, which may serve as a new potential target for myopia control or prevention.

CHAPTER 6 References

Asari, H., & Meister, M. (2012). Divergence of visual channels in the inner retina. *Nat Neurosci, 15*(11), 1581-1589. doi:10.1038/nn.3241

Ashby, R. S., Zeng, G., Leotta, A. J., Tse, D. Y., & McFadden, S. A. (2014). Egr-1 mRNA expression is a marker for the direction of mammalian ocular growth. *Invest Ophthalmol Vis Sci, 55*(9), 5911-5921. doi:10.1167/iovs.13-11708

Atchison, D. A., Schmid, K. L., & Pritchard, N. (2006). Neural and optical limits to visual performance in myopia. *Vision Res, 46*(21), 3707-3722.

Baden, T., Berens, P., Franke, K., Román Rosón, M., Bethge, M., & Euler, T. (2016). The functional diversity of retinal ganglion cells in the mouse. *Nature, 529*(7586), 345-350. doi:10.1038/nature16468

Banerjee, S., Wang, Q., So, C. H., & Pan, F. (2020). Defocused Images Change Multineuronal Firing Patterns in the Mouse Retina. *Cells, 9*(3), 530.

Banerjee, S., Wang, Q., Zhao, F., Tang, G., So, C., Tse, D., . . . Pan, F. (2020). Increased Connexin36 Phosphorylation in AII Amacrine Cell Coupling of the Mouse Myopic Retina. *Frontiers in Cellular Neuroscience, 14*(124). doi:10.3389/fncel.2020.00124

Barathi, V. A., Boopathi, V. G., Yap, E. P. H., & Beuerman, R. W. (2008). Two models of experimental myopia in the mouse. *Vision Res, 48*(7), 904-916. doi:https://doi.org/10.1016/j.visres.2008.01.004

Beresford, J. A., Crewther, S. G., Kiely, P. M., & Crewther, D. P. (2001). Comparison of refractive state and circumferential morphology of retina, choroid, and sclera in chick models of experimentally induced ametropia. *Optometry and vision science, 78*(1), 40-49.

Bitzer, M., & Schaeffel, F. (2002). Defocus-induced changes in ZENK expression in the chicken retina. *Invest Ophthalmol Vis Sci, 43*(1), 246-252.

Bloomfield, S. A., & Miller, R. F. (1982). A physiological and morphological study of the horizontal cell types of the rabbit retina. *The Journal of comparative neurology, 208*(3), 288-303. doi:10.1002/cne.902080306

Bloomfield, S. A., & Volgyi, B. (2007). Response properties of a unique subtype of wide-field amacrine cell in the rabbit retina. *Vis Neurosci, 24*(4), 459-469. doi:10.1017/S0952523807070071

Bloomfield, S. A., & Volgyi, B. (2009). The diverse functional roles and regulation of neuronal gap junctions in the retina. *Nat Rev Neurosci, 10*(7), 495-506. doi:10.1038/nrn2636

Bloomfield, S. A., & Völgyi, B. (2004). Function and plasticity of homologous coupling between AII amacrine cells. *Vision Res, 44*(28), 3297-3306. doi:https://doi.org/10.1016/j.visres.2004.07.012

Bloomfield, S. A., & Völgyi, B. (2009). The diverse functional roles and regulation of neuronal gap junctions in the retina. *Nature Reviews Neuroscience, 10*, 495. doi:10.1038/nrn2636

Bowrey, H., Zeng, G., Tse, D., Leotta, A., Wu, Y., To, C.-H., . . . McFadden, S. (2017). The Effect of Spectacle Lenses Containing Peripheral Defocus on Refractive Error and Horizontal Eye Shape in the Guinea Pig. *Invest Ophthalmol Vis Sci, 58*(5), 2705-2714. doi:10.1167/iovs.16-20240

Chakraborty, R., Park, H. n., Hanif, A. M., Sidhu, C. S., Iuvone, P. M., & Pardue, M. T. (2015). ON pathway mutations increase susceptibility to form-deprivation myopia. *Experimental Eye Research, 137*, 79-83. doi:https://doi.org/10.1016/j.exer.2015.06.009

Chui, Y., Yap, M., & Chan, H. (2002). The Retinal Ganglion Cell Density and Nerve Fiber Layer Thickness in the Human Myopic Eye. *Invest Ophthalmol Vis Sci, 43*(13), 183-183.

Deans, M. R., Volgyi, B., Goodenough, D. A., Bloomfield, S. A., & Paul, D. L. (2002). Connexin36 is essential for transmission of rod-mediated visual signals in the mammalian retina. *Neuron, 36*(4), 703-712. doi:10.1016/s0896-6273(02)01046-2

Deans., Gibson, J. R., Sellitto, C., Connors, B. W., & Paul, D. L. (2001). Synchronous activity of inhibitory networks in neocortex requires electrical synapses containing connexin36. *Neuron, 31*(3), 477-485. doi:10.1016/s0896-6273(01)00373-7

Dedek, K., Schultz, K., Pieper, M., Dirks, P., Maxeiner, S., Willecke, K., . . . Janssen-Bienhold, U. (2006). Localization of heterotypic gap junctions composed of connexin45 and connexin36 in the rod pathway of the mouse retina. *Eur J Neurosci, 24*(6), 1675-1686. doi:10.1111/j.1460-9568.2006.05052.x

Della Santina, L., Inman, D. M., Lupien, C. B., Horner, P. J., & Wong, R. O. (2013). Differential progression of structural and functional alterations in distinct retinal ganglion cell types in a mouse model of glaucoma. *Journal of Neuroscience, 33*(44), 17444-17457.

Demb, J. B., & Singer, J. H. (2015). Functional Circuitry of the Retina. *Annual Review of Vision Science, 1*(1), 263-289. doi:10.1146/annurev-vision-082114-035334

DeVries, S. H., Qi, X., Smith, R., Makous, W., & Sterling, P. (2002). Electrical coupling between mammalian cones. *Curr Biol, 12*(22), 1900-1907. doi:10.1016/s0960-9822(02)01261-7

Diedrich, E., & Schaeffel, F. (2009). Spatial resolution, contrast sensitivity, and sensitivity to defocus of chicken retinal ganglion cells in vitro. *Vis Neurosci, 26*(5-6), 467-476. doi:10.1017/S0952523809990253

Doyle, S. E., McIvor, W. E., & Menaker, M. (2002). Circadian rhythmicity in dopamine content of mammalian retina: role of the photoreceptors. *J Neurochem, 83*(1), 211-219. doi:10.1046/j.1471-4159.2002.01149.x

Du, Y.-m., Xia, C.-k., Zhao, N., Dong, Q., Lei, M., & Xia, J.-h. (2012). 18β-Glycyrrhetinic acid preferentially blocks late Na current generated by ΔKPQ Nav1.5 channels. *Acta Pharmacologica Sinica, 33*(6), 752-760. doi:10.1038/aps.2012.22

Ebrey, T., & Koutalos, Y. (2001). Vertebrate Photoreceptors. *Progress in retinal and eye research, 20*(1), 49-94. doi:https://doi.org/10.1016/S1350-9462(00)00014-8

Euler, T., Haverkamp, S., Schubert, T., & Baden, T. (2014). Retinal bipolar cells: elementary building blocks of vision. *Nature Reviews Neuroscience, 15*(8), 507-519. doi:10.1038/nrn3783

Famiglietti, E. V., Jr., & Kolb, H. (1975). A bistratified amacrine cell and synaptic cirucitry in the inner plexiform layer of the retina. *Brain Res, 84*(2), 293-300. doi:10.1016/0006-8993(75)90983-x

Farajian, R., Pan, F., Akopian, A., Völgyi, B., & Bloomfield, S. A. (2011). Masked excitatory crosstalk between the ON and OFF visual pathways in the mammalian retina. *The Journal of physiology, 589*(Pt 18), 4473-4489. doi:10.1113/jphysiol.2011.213371

Farshi, P., Fyk-Kolodziej, B., Krolewski, D. M., Walker, P. D., & Ichinose, T. (2016). Dopamine D1 receptor expression is bipolar cell type-specific in the mouse retina. *The Journal of comparative neurology, 524*(10), 2059-2079. doi:10.1002/cne.23932

Faulkner, A. E., Kim, M. K., Iuvone, P. M., & Pardue, M. T. (2007). Head-mounted goggles for murine form deprivation myopia. *J Neurosci Methods, 161*(1), 96-100.

Feigenspan, A., Janssen-Bienhold, U., Hormuzdi, S., Monyer, H., Degen, J., Sohl, G., . . . Weiler, R. (2004). Expression of connexin36 in cone pedicles and OFF-cone bipolar cells of the mouse retina. *J Neurosci, 24*(13), 3325-3334. doi:10.1523/jneurosci.5598-03.2004

Feigenspan, A., Teubner, B., Willecke, K., & Weiler, R. (2001). Expression of neuronal connexin36 in AII amacrine cells of the mammalian retina. *J Neurosci, 21*(1), 230-239.

Feldkaemper, M., & Schaeffel, F. (2013). An updated view on the role of dopamine in myopia. *Exp Eye Res, 114*, 106-119. doi:10.1016/j.exer.2013.02.007

Fischer, A. J., McGuire, J. J., Schaeffel, F., & Stell, W. K. (1999). Light- and focus-dependent expression of the transcription factor ZENK in the chick retina. *Nat Neurosci, 2*(8), 706-712. doi:10.1038/11167

Fu, Y., & Yau, K.-W. (2007). Phototransduction in mouse rods and cones. *Pflugers Archiv : European journal of physiology, 454*(5), 805-819. doi:10.1007/s00424-006-0194-y

Gao, Q., Liu, Q., Ma, P., Zhong, X., Wu, J., & Ge, J. (2006). Effects of direct intravitreal dopamine injections on the development of lid-suture induced myopia in rabbits. *Graefe's archive for clinical and experimental ophthalmology, 244*(10), 1329-1335.

Ghahari, A., Kumar, S. R., & Badea, T. C. (2018). Identification of Retinal Ganglion Cell Firing Patterns Using Clustering Analysis Supplied with Failure Diagnosis. *Int J Neural Syst, 28*(8), 1850008. doi:10.1142/s0129065718500089

Ghosh, K. K., Bujan, S., Haverkamp, S., Feigenspan, A., & Wassle, H. (2004). Types of bipolar cells in the mouse retina. *The Journal of comparative neurology, 469*(1), 70-82. doi:10.1002/cne.10985

Gjorgjieva, J., Sompolinsky, H., & Meister, M. (2014). Benefits of pathway splitting in sensory coding. *J Neurosci, 34*(36), 12127-12144. doi:10.1523/jneurosci.1032-14.2014

Glickstein, M., & Millodot, M. (1970). Retinoscopy and eye size. *Science, 168*(3931), 605-606.

Goh, W. S., & Lam, C. S. (1994). Changes in refractive trends and optical components of Hong Kong Chinese aged 19-39 years. *Ophthalmic Physiol Opt, 14*(4), 378-382.

Gollender, M., Thorn, F., & Erickson, P. (1979). Development of axial ocular dimensions following eyelid suture in the cat. *Vision Res, 19*(2), 221-223.

Gollisch, T., & Meister, M. (2008). Rapid neural coding in the retina with relative spike latencies. *Science, 319*(5866), 1108-1111. doi:10.1126/science.1149639

Gollisch, T., & Meister, M. (2010). Eye smarter than scientists believed: neural computations in circuits of the retina. *Neuron, 65*(2), 150-164. doi:10.1016/j.neuron.2009.12.009

Goodenough, D. A., & Paul, D. L. (2003). Beyond the gap: functions of unpaired connexon channels. *Nat Rev Mol Cell Biol, 4*(4), 285-294. doi:10.1038/nrm1072

Hampson, E. C., Vaney, D. I., & Weiler, R. (1992). Dopaminergic modulation of gap junction permeability between amacrine cells in mammalian retina. *J Neurosci, 12*(12), 4911-4922. Retrieved from http://www.ncbi.nlm.nih.gov/pubmed/1281499

Harper, A. R., & Summers, J. A. (2015). The dynamic sclera: extracellular matrix remodeling in normal ocular growth and myopia development. *Exp Eye Res, 133*, 100-111. doi:10.1016/j.exer.2014.07.015

Hartline, H. K. (1938). The response of single optic nerve fibers of the vertebrate eye to illumination of the retina. *American Journal of Physiology, 121*, 400-415.

Holden, B. A., Fricke, T. R., Wilson, D. A., Jong, M., Naidoo, K. S., Sankaridurg, P., . . . Resnikoff, S. (2016). Global Prevalence of Myopia and High Myopia and Temporal Trends from 2000 through 2050. *Ophthalmology, 123*(5), 1036-1042. doi:10.1016/j.ophtha.2016.01.006

Hombach, S., Janssen-Bienhold, U., Sohl, G., Schubert, T., Bussow, H., Ott, T., . . . Willecke, K. (2004). Functional expression of connexin57 in horizontal cells of the mouse retina. *Eur J Neurosci, 19*(10), 2633-2640. doi:10.1111/j.0953-816X.2004.03360.x

Howland, H. C. (1985). Optics of photoretinoscopy: results from ray tracing. *Am J Optom Physiol Opt, 62*(9), 621-625.

Howlett, M. H., & McFadden, S. A. (2006). Form-deprivation myopia in the guinea pig (Cavia porcellus). *Vision Res, 46*(1-2), 267-283.

Huang, F., Zhang, L., Wang, Q., Yang, Y., Li, Q., Wu, Y., . . . Zhou, X. (2018). Dopamine D1 Receptors Contribute Critically to the Apomorphine-Induced Inhibition of Form-Deprivation Myopia in Mice. *Invest Ophthalmol Vis Sci, 59*(6), 2623-2634. doi:10.1167/iovs.17-22578

Ivanova, E., Yee, C. W., & Sagdullaev, B. T. (2015). Increased phosphorylation of Cx36 gap junctions in the AII amacrine cells of RD retina. *Frontiers in Cellular Neuroscience, 9*(390). doi:10.3389/fncel.2015.00390

Jackman, S. L., Babai, N., Chambers, J. J., Thoreson, W. B., & Kramer, R. H. (2011). A positive feedback synapse from retinal horizontal cells to cone photoreceptors. *PLoS Biol, 9*(5), e1001057. doi:10.1371/journal.pbio.1001057

Jalligampala, A., Sekhar, S., Zrenner, E., & Rathbun, D. L. (2017). Optimal voltage stimulation parameters for network-mediated responses in wild type and rd10 mouse retinal ganglion cells. *J Neural Eng, 14*(2), 026004. doi:10.1088/1741-2552/14/2/026004

Jiang, X., Kurihara, T., Kunimi, H., Miyauchi, M., Ikeda, S.-i., Mori, K., . . . Tsubota, K. (2018). A highly efficient murine model of experimental myopia. *Scientific Reports, 8*(1), 2026. doi:10.1038/s41598-018-20272-w

Justice, M. J., Siracusa, L. D., & Stewart, A. F. (2011). Technical approaches for mouse models of human disease. *Disease models & mechanisms, 4*(3), 305-310.

Kolb, H., & Famiglietti, E. V. (1974). Rod and cone pathways in the inner plexiform layer of cat retina. *Science, 186*(4158), 47-49. doi:10.1126/science.186.4158.47

Kothmann, W. W., Li, X., Burr, G. S., & O'Brien, J. (2007). Connexin 35/36 is phosphorylated at regulatory sites in the retina. *Visual neuroscience, 24*(3), 363-375. doi:10.1017/s095252380707037x

Kothmann, W. W., Massey, S. C., & O'Brien, J. (2009). Dopamine-stimulated dephosphorylation of connexin 36 mediates AII amacrine cell uncoupling. *J Neurosci, 29*(47), 14903-14911. doi:10.1523/jneurosci.3436-09.2009

Kothmann, W. W., Trexler, E. B., Whitaker, C. M., Li, W., Massey, S. C., & O'Brien, J. (2012). Nonsynaptic NMDA receptors mediate activity-dependent plasticity of gap junctional coupling in the AII amacrine cell network. *J Neurosci, 32*(20), 6747-6759. doi:10.1523/jneurosci.5087-11.2012

Krebs, M. P., Collin, G. B., Hicks, W. L., Yu, M., Charette, J. R., Shi, L. Y., . . . Nishina, P. M. (2017). Mouse models of human ocular disease for translational research. *PLoS ONE, 12*(8), e0183837. doi:10.1371/journal.pone.0183837

Lan, W., Yang, Z., Feldkaemper, M., & Schaeffel, F. (2016). Changes in dopamine and ZENK during suppression of myopia in chicks by intense illuminance. *Experimental Eye Research, 145*, 118-124. doi:https://doi.org/10.1016/j.exer.2015.11.018

Lasater, E. M., & Dowling, J. E. (1985). Dopamine decreases conductance of the electrical junctions between cultured retinal horizontal cells. *Proc Natl Acad Sci U S A, 82*(9), 3025-3029. doi:10.1073/pnas.82.9.3025

LAUBER, J. K. (1991). Avian models for experimental myopia. *Journal of Ocular Pharmacology and Therapeutics, 7*(3), 259-276.

Lee, E. J., Han, J. W., Kim, H. J., Kim, I. B., Lee, M. Y., Oh, S. J., . . . Chun, M. H. (2003). The immunocytochemical localization of connexin 36 at rod and cone gap junctions in the guinea pig retina. *Eur J Neurosci, 18*(11), 2925-2934. doi:10.1046/j.1460-9568.2003.03049.x

Lettvin, J. Y., Maturana, H. R., McCulloch, W. S., & Pitts, W. H. (1959). What the frog's eye tells the frog's brain. *Proceedings of the IRE, 47*(11), 1940-1951.

Liang, H., Crewther, D., Crewther, S. G., & Barila, A. (1995). A role for photoreceptor outer segments in the induction of deprivation myopia. *Vision Res, 35*(9), 1217-1225.

Lin, B., & Masland, R. H. (2006). Populations of wide-field amacrine cells in the mouse retina. *Journal of Comparative Neurology, 499*(5), 797-809. doi:10.1002/cne.21126

Liou, S.-W., & Chiu, C.-J. (2001). Myopia and contrast sensitivity function. *Current Eye Research, 22*(2), 81-84.

Liu, M.-G., Chen, X.-F., He, T., Li, Z., & Chen, J. (2012). Use of multi-electrode array recordings in studies of network synaptic plasticity in both time and space. *Neuroscience Bulletin, 28*(4), 409-422. doi:10.1007/s12264-012-1251-5

Maccione, A., Gandolfo, M., Zordan, S., Amin, H., Di Marco, S., Nieus, T., . . . Berdondini, L. (2015). Microelectronics, bioinformatics and neurocomputation for massive neuronal recordings in brain circuits with large scale multielectrode array probes. *Brain Res Bull, 119*(Pt B), 118-126. doi:10.1016/j.brainresbull.2015.07.008

Maiello, G., Walker, L., Bex, P. J., & Vera-Diaz, F. A. (2017). Blur perception throughout the visual field in myopia and emmetropia. *J Vis, 17*(5), 3. doi:10.1167/17.5.3

Mani, A., & Schwartz, G. W. (2017). Circuit Mechanisms of a Retinal Ganglion Cell with Stimulus-Dependent Response Latency and Activation Beyond Its Dendrites. *Curr Biol, 27*(4), 471-482. doi:10.1016/j.cub.2016.12.033

Masland, R. H. (2001). The fundamental plan of the retina. *Nat Neurosci, 4*(9), 877-886. doi:10.1038/nn0901-877

Masland, R. H. (2012). The neuronal organization of the retina. *Neuron, 76*(2), 266-280. doi:10.1016/j.neuron.2012.10.002

Massey, S. C. (2006). Chapter 4 - Functional Anatomy of the Mammalian Retina. In S. J. Ryan, D. R. Hinton, A. P. Schachat, & C. P. Wilkinson (Eds.), *Retina (Fourth Edition)* (pp. 43-82). Edinburgh: Mosby.

Mazade, R. E., Flood, M. D., & Eggers, E. D. (2019). Dopamine D1 receptor activation reduces local inner retinal inhibition to light-adapted levels. *J Neurophysiol, 121*(4), 1232-1243. doi:10.1152/jn.00448.2018

McBrien, N. A., & Gentle, A. (2003). Role of the sclera in the development and pathological complications of myopia. *Progress in retinal and eye research, 22*(3), 307-338.

McBrien, N. A., & Norton, T. T. (1992). The development of experimental myopia and ocular component dimensions in monocularly lid-sutured tree shrews (Tupaia belangeri). *Vision Res, 32*(5), 843-852.

Meister, M., & Berry, M. J., 2nd. (1999). The neural code of the retina. *Neuron, 22*(3), 435-450. doi:10.1016/s0896-6273(00)80700-x

Meister, M., Pine, J., & Baylor, D. A. (1994). Multi-neuronal signals from the retina: acquisition and analysis. *J Neurosci Methods, 51*(1), 95-106.

Meyer, A., Hilgen, G., Dorgau, B., Sammler, E. M., Weiler, R., Monyer, H., . . . Hormuzdi, S. G. (2014). AII amacrine cells discriminate between heterocellular and homocellular locations when assembling connexin36-containing gap junctions. *Journal of cell science, 127*(Pt 6), 1190-1202. doi:10.1242/jcs.133066

Miccoli, B., Lopez, C. M., Goikoetxea, E., Putzeys, J., Sekeri, M., Krylychkina, O., . . . Braeken, D. (2019). High-Density Electrical Recording and Impedance Imaging With a Multi-Modal CMOS Multi-Electrode Array Chip. *Frontiers in Neuroscience, 13*(641). doi:10.3389/fnins.2019.00641

Mills, S. L., O'Brien, J. J., Li, W., O'Brien, J., & Massey, S. C. (2001). Rod pathways in the mammalian retina use connexin 36. *The Journal of comparative neurology, 436*(3), 336-350.

Mills., O'Brien., Li, W., O'Brien., & Massey. (2001). Rod pathways in the mammalian retina use connexin 36. *The Journal of comparative neurology, 436*(3), 336-350.

Morgan, I. G., French, A. N., Ashby, R. S., Guo, X., Ding, X., He, M., & Rose, K. A. (2018). The epidemics of myopia: Aetiology and prevention. *Prog Retin Eye Res, 62*, 134-149. doi:10.1016/j.preteyeres.2017.09.004

Morgan, I. G., Ohno-Matsui, K., & Saw, S.-M. (2012). Myopia. *The Lancet, 379*(9827), 1739-1748. doi:https://doi.org/10.1016/S0140-6736(12)60272-4

Murphy, G. J., & Rieke, F. (2006). Network variability limits stimulus-evoked spike timing precision in retinal ganglion cells. *Neuron, 52*(3), 511-524. doi:10.1016/j.neuron.2006.09.014

Muzyka, V. V., Brooks, M., & Badea, T. C. (2018). Postnatal developmental dynamics of cell type specification genes in Brn3a/Pou4f1 Retinal Ganglion Cells. *Neural Dev, 13*(1), 15. doi:10.1186/s13064-018-0110-0

Nebbioso, M., Plateroti, A., Pucci, B., & Pescosolido, N. (2014). Role of the Dopaminergic System in the Development of Myopia in Children and Adolescents. *Journal of Child Neurology, 29*(12), 1739-1746. doi:10.1177/0883073814538666

Nguyen-Legros, J., Versaux-Botteri, C., & Vernier, P. (1999). Dopamine receptor localization in the mammalian retina. *Mol Neurobiol, 19*(3), 181-204. doi:10.1007/bf02821713

Norton, T. T. (1999). Animal Models of Myopia: Learning How Vision Controls the Size of the Eye. *Ilar j, 40*(2), 59-77. doi:10.1093/ilar.40.2.59

O'Brien, & Bloomfield, S. A. (2018). Plasticity of Retinal Gap Junctions: Roles in Synaptic Physiology and Disease. *Annu Rev Vis Sci, 4*, 79-100. doi:10.1146/annurev-vision-091517-034133

O'Brien, J. J., Li, W., Pan, F., Keung, J., O'Brien, J., & Massey, S. C. (2006). Coupling between A-type horizontal cells is mediated by connexin 50 gap junctions in the rabbit retina. *J Neurosci, 26*(45), 11624-11636. doi:10.1523/jneurosci.2296-06.2006

O'Brien. (2014). The ever-changing electrical synapse. *Curr Opin Neurobiol, 29*, 64-72. doi:10.1016/j.conb.2014.05.011

Obien, M. E., Deligkaris, K., Bullmann, T., Bakkum, D. J., & Frey, U. (2014). Revealing neuronal function through microelectrode array recordings. *Front Neurosci, 8*, 423. doi:10.3389/fnins.2014.00423

Ohno-Matsui, K. (2016). Pathologic Myopia. *Asia Pac J Ophthalmol (Phila), 5*(6), 415-423. doi:10.1097/apo.0000000000000230

Osol, G., Schwartz, B., & Foss, D. C. (1986). The effects of photoperiod and lid suture on eye growth in chickens. *Invest Ophthalmol Vis Sci, 27*(2), 255-260.

Pan, F. (2019). Defocused Image Changes Signaling of Ganglion Cells in the Mouse Retina. *Cells, 8*(7). doi:10.3390/cells8070640

Pan, F., Toychiev, A., Zhang, Y., Atlasz, T., Ramakrishnan, H., Roy, K., . . . Bloomfield, S. A. (2016). Inhibitory masking controls the threshold sensitivity of retinal ganglion cells. *J Physiol, 594*(22), 6679-6699. doi:10.1113/jp272267

Pang, J. J., Gao, F., & Wu, S. M. (2003). Light-evoked excitatory and inhibitory synaptic inputs to ON and OFF alpha ganglion cells in the mouse retina. *J Neurosci, 23*(14), 6063-6073. doi:10.1523/jneurosci.23-14-06063.2003

Pardue, M., Faulkner, A. E., Fernandes, A., Yin, H., Schaeffel, F., Williams, R. W., . . . Iuvone, P. M. (2008). High Susceptibility to Experimental Myopia in a Mouse Model with a Retinal ON Pathway Defect. *Invest Ophthalmol Vis Sci, 49*(2), 706-712. doi:10.1167/iovs.07-0643

Pardue., Stone, R. A., & Iuvone, P. M. (2013). Investigating mechanisms of myopia in mice. *Exp Eye Res, 114*, 96-105. doi:10.1016/j.exer.2012.12.014

Park, H., Tan, C. C., Faulkner, A., Jabbar, S. B., Schmid, G., Abey, J., . . . Pardue, M. T. (2013). Retinal degeneration increases susceptibility to myopia in mice. *Mol Vis, 19*, 2068-2079.

Peirce, J. W. (2007). PsychoPy--Psychophysics software in Python. *Journal of neuroscience methods, 162*(1-2), 8-13. doi:10.1016/j.jneumeth.2006.11.017

Peirce, J. W. (2009). Generating Stimuli for Neuroscience Using PsychoPy. *Frontiers in neuroinformatics, 2*, 10-10. doi:10.3389/neuro.11.010.2008

Pérez De Sevilla Müller, L., Shelley, J., & Weiler, R. (2007). Displaced amacrine cells of the mouse retina. *The Journal of comparative neurology, 505*(2), 177-189. doi:10.1002/cne.21487

Pernelle, G., Nicola, W., & Clopath, C. (2018). Gap junction plasticity as a mechanism to regulate network-wide oscillations. *PLOS Computational Biology, 14*(3), e1006025. doi:10.1371/journal.pcbi.1006025

Pourcho, R. G. (1996). Neurotransmitters in the retina. *Current Eye Research, 15*(7), 797-803. doi:10.3109/02713689609003465

Rada, J. A. S., Shelton, S., & Norton, T. T. (2006). The sclera and myopia. *Experimental Eye Research, 82*(2), 185-200.

Reinhard, K., Tikidji-Hamburyan, A., Seitter, H., Idrees, S., Mutter, M., Benkner, B., & Münch, T. A. (2014). Step-By-Step Instructions for Retina Recordings with Perforated Multi Electrode Arrays. *PLoS ONE, 9*(8), e106148. doi:10.1371/journal.pone.0106148

Roy, K., Kumar, S., & Bloomfield, S. A. (2017). Gap junctional coupling between retinal amacrine and ganglion cells underlies coherent activity integral to global object perception. *Proceedings of the National Academy of Sciences of the United States of America, 114*(48), E10484-E10493. doi:10.1073/pnas.1708261114

Rymer, J., & Wildsoet, C. F. (2005). The role of the retinal pigment epithelium in eye growth regulation and myopia: a review. *Visual neuroscience, 22*(3), 251-261.

Saw, S. M., Gazzard, G., Shih-Yen, E. C., & Chua, W. H. (2005). Myopia and associated pathological complications. *Ophthalmic and Physiological Optics, 25*(5), 381-391.

Schaeffel, F. (2008). Test systems for measuring ocular parameters and visual function in mice. *Front Biosci, 13*, 4904-4911. doi:10.2741/3049

Schaeffel, F. (2010). The Mouse Model of Myopia. In *Myopia* (pp. 303-330): WORLD SCIENTIFIC.

Schaeffel, F., Burkhardt, E., Howland, H. C., & Williams, R. W. (2004). Measurement of refractive state and deprivation myopia in two strains of mice. *Optom Vis Sci, 81*(2), 99-110.

Schaeffel, F., Farkas, L., & Howland, H. C. (1987). Infrared photoretinoscope. *Appl Opt, 26*(8), 1505-1509. doi:10.1364/ao.26.001505

Schaeffel, F., Glasser, A., & Howland, H. C. (1988). Accommodation, refractive error and eye growth in chickens. *Vision Res, 28*(5), 639-657.

Schaeffel, F., & Wildsoet, C. (2013). Can the retina alone detect the sign of defocus? *Ophthalmic Physiol Opt, 33*(3), 362-367. doi:10.1111/opo.12058

Schippert, R., Burkhardt, E., Feldkaemper, M., & Schaeffel, F. (2007). Relative Axial Myopia in Egr-1 (ZENK) Knockout Mice. *Invest Ophthalmol Vis Sci, 48*(1), 11-17. doi:10.1167/iovs.06-0851

Schmid, K. L., & Wildsoet, C. F. (2004). Inhibitory effects of apomorphine and atropine and their combination on myopia in chicks. *Optometry and vision science, 81*(2), 137-147.

Schmucker, C., & Schaeffel, F. (2004). A paraxial schematic eye model for the growing C57BL/6 mouse. *Vision Res, 44*(16), 1857-1867. doi:10.1016/j.visres.2004.03.011

Schmucker, C., & Schaeffel, F. (2004). A paraxial schematic eye model for the growing C57BL/6 mouse. *Vision Research, 44*(16), 1857-1867. doi:https://doi.org/10.1016/j.visres.2004.03.011

Schubert, T., Degen, J., Willecke, K., Hormuzdi, S. G., Monyer, H., & Weiler, R. (2005). Connexin36 mediates gap junctional coupling of alpha-ganglion cells in mouse retina. *Journal of Comparative Neurology, 485*(3), 191-201. doi:10.1002/cne.20510

Schubert, T., Maxeiner, S., Kruger, O., Willecke, K., & Weiler, R. (2005). Connexin45 mediates gap junctional coupling of bistratified ganglion cells in the mouse retina. *The Journal of comparative neurology, 490*(1), 29-39. doi:10.1002/cne.20621

Segev, R., Goodhouse, J., Puchalla, J., & Berry, M. J., 2nd. (2004). Recording spikes from a large fraction of the ganglion cells in a retinal patch. *Nat Neurosci, 7*(10), 1154-1161. doi:10.1038/nn1323

Seo, S., Lee, C. E., Jeong, J. H., Park, K. H., Kim, D. M., & Jeoung, J. W. (2017). Ganglion cell-inner plexiform layer and retinal nerve fiber layer thickness according to myopia and optic disc area: a quantitative and three-dimensional analysis. *BMC Ophthalmology, 17*(1), 22. doi:10.1186/s12886-017-0419-1

Shelley, J., Dedek, K., Schubert, T., Feigenspan, A., Schultz, K., Hombach, S., . . . Weiler, R. (2006). Horizontal cell receptive fields are reduced in connexin57-deficient mice. *Eur J Neurosci, 23*(12), 3176-3186. doi:10.1111/j.1460-9568.2006.04848.x

Sherman, S. M., Norton, T., & Casagrande, V. (1977). Myopia in the lid-sutured tree shrew (Tupaia glis). *Brain research, 124*(1), 154-157.

Smith, E. L., 3rd, Hung, L. F., & Arumugam, B. (2014). Visual regulation of refractive development: insights from animal studies. *Eye (Lond), 28*(2), 180-188. doi:10.1038/eye.2013.277

Smith III, E. L., & Hung, L.-F. (1999). The role of optical defocus in regulating refractive development in infant monkeys. *Vision Res, 39*(8), 1415-1435.

Smith III, E. L., & Hung, L.-F. (2000). Form-deprivation myopia in monkeys is a graded phenomenon. *Vision Res, 40*(4), 371-381.

Söhl, G., Maxeiner, S., & Willecke, K. (2005). Expression and functions of neuronal gap junctions. *Nat Rev Neurosci, 6*(3), 191-200. doi:10.1038/nrn1627

Söhl, G., & Willecke, K. (2003). An update on connexin genes and their nomenclature in mouse and man. *Cell Commun Adhes, 10*(4-6), 173-180. doi:10.1080/cac.10.4-6.173.180

Stone, R. A., Pardue, M. T., Iuvone, P. M., & Khurana, T. S. (2013). Pharmacology of myopia and potential role for intrinsic retinal circadian rhythms. *Exp Eye Res, 114*, 35-47. doi:10.1016/j.exer.2013.01.001

Strang, N. C., Winn, B., & Bradley, A. (1998). The role of neural and optical factors in limiting visual resolution in myopia. *Vision Res, 38*(11), 1713-1721.

Strettoi, E., Dacheux, R. F., & Raviola, E. (1990). Synaptic connections of rod bipolar cells in the inner plexiform layer of the rabbit retina. *The Journal of comparative neurology, 295*(3), 449-466. doi:10.1002/cne.902950309

Strettoi, E., & Masland, R. H. (1995). The organization of the inner nuclear layer of the rabbit retina. *J Neurosci, 15*(1 Pt 2), 875-888. doi:10.1523/jneurosci.15-01-00875.1995

Strettoi, E., Raviola, E., & Dacheux, R. F. (1992). Synaptic connections of the narrow-field, bistratified rod amacrine cell (AII) in the rabbit retina. *The Journal of comparative neurology, 325*(2), 152-168. doi:10.1002/cne.903250203

Tejedor, J., & de la Villa, P. (2003). Refractive changes induced by form deprivation in the mouse eye. *Invest Ophthalmol Vis Sci, 44*(1), 32-36. doi:10.1167/iovs.01-1171

Thomas, C. A., Springer, P. A., Loeb, G. E., Berwald-Netter, Y., & Okun, L. M. (1972). A miniature microelectrode array to monitor the bioelectric activity of cultured cells. *Experimental Cell Research, 74*(1), 61-66. doi:https://doi.org/10.1016/0014-4827(72)90481-8

Thoreson, W. B., & Mangel, S. C. (2012). Lateral interactions in the outer retina. *Progress in retinal and eye research, 31*(5), 407-441. doi:10.1016/j.preteyeres.2012.04.003

Tian, N., Xu, H. P., & Wang, P. (2015). Dopamine D2 receptors preferentially regulate the development of light responses of the inner retina. *Eur J Neurosci, 41*(1), 17-30. doi:10.1111/ejn.12783

Tigges, M., Tigges, J., Fernandes, A., Eggers, H. M., & Gammon, J. (1990). Postnatal axial eye elongation in normal and visually deprived rhesus monkeys. *Invest Ophthalmol Vis Sci, 31*(6), 1035-1046.

Tkatchenko, T. V., Shen, Y., & Tkatchenko, A. V. (2010). Analysis of postnatal eye development in the mouse with high-resolution small animal magnetic resonance imaging. *Investigative Ophthalmology & Visual Science, 51*(1), 21-27. doi:10.1167/iovs.08-2767

Tkatchenko, T. V., Troilo, D., Benavente-Perez, A., & Tkatchenko, A. V. (2018). Gene expression in response to optical defocus of opposite signs reveals bidirectional mechanism of visually guided eye growth. *PLoS Biol, 16*(10), e2006021. doi:10.1371/journal.pbio.2006021

Tokoro, T. (1970). Experimental myopia in rabbits. *Invest Ophthalmol Vis Sci, 9*(12), 926-934.

Troilo, D., & Judge, S. J. (1993). Ocular development and visual deprivation myopia in the common marmoset (Callithrix jacchus). *Vision Res, 33*(10), 1311-1324.

Vaney, D. I. (1985). The morphology and topographic distribution of AII amacrine cells in the cat retina. *Proc R Soc Lond B Biol Sci, 224*(1237), 475-488. doi:10.1098/rspb.1985.0045

Vaney, D. I. (1991). Many diverse types of retinal neurons show tracer coupling when injected with biocytin or Neurobiotin. *Neurosci Lett, 125*(2), 187-190. doi:10.1016/0304-3940(91)90024-n

Vaney, D. I., & Weiler, R. (2000). Gap junctions in the eye: evidence for heteromeric, heterotypic and mixed-homotypic interactions. *Brain Res Brain Res Rev, 32*(1), 115-120. doi:10.1016/s0165-0173(99)00070-3

Völgyi, B., Abrams, J., Paul, D. L., & Bloomfield, S. A. (2005). Morphology and tracer coupling pattern of alpha ganglion cells in the mouse retina. *The Journal of comparative neurology, 492*(1), 66-77. doi:10.1002/cne.20700

Völgyi, B., Deans, M. R., Paul, D. L., & Bloomfield, S. A. (2004). Convergence and segregation of the multiple rod pathways in mammalian retina. *The Journal of neuroscience : the official journal of the Society for Neuroscience, 24*(49), 11182-11192. doi:10.1523/JNEUROSCI.3096-04.2004

Völgyi, B., Deans, M. R., Paul, D. L., & Bloomfield, S. A. (2004). Convergence and segregation of the multiple rod pathways in mammalian retina. *Journal of Neuroscience, 24*(49), 11182-11192.

Volgyi, B., Pan, F., Paul, D. L., Wang, J. T., Huberman, A. D., & Bloomfield, S. A. (2013). Gap junctions are essential for generating the correlated spike activity of neighboring retinal ganglion cells. *PLoS ONE, 8*(7), e69426. doi:10.1371/journal.pone.0069426

Völgyi, B., Pan, F., Paul, D. L., Wang, J. T., Huberman, A. D., & Bloomfield, S. A. (2013). Gap junctions are essential for generating the correlated spike activity of neighboring retinal ganglion cells. *PLoS One, 8*(7), e69426-e69426. doi:10.1371/journal.pone.0069426

Volgyi, B., Xin, D., Amarillo, Y., & Bloomfield, S. A. (2001). Morphology and physiology of the polyaxonal amacrine cells in the rabbit retina. *J Comp Neurol, 440*(1), 109-125. doi:10.1002/cne.1373

Wässle, H. (2004). Parallel processing in the mammalian retina. *Nature Reviews Neuroscience, 5*, 747. doi:10.1038/nrn1497

Wässle, H., Puller, C., Müller, F., & Haverkamp, S. (2009). Cone contacts, mosaics, and territories of bipolar cells in the mouse retina. *J Neurosci, 29*(1), 106-117. doi:10.1523/jneurosci.4442-08.2009

Wei, W., Elstrott, J., & Feller, M. B. (2010). Two-photon targeted recording of GFP-expressing neurons for light responses and live-cell imaging in the mouse retina. *Nature protocols, 5*(7), 1347-1352. doi:10.1038/nprot.2010.106

Werblin, F. S., & Dowling, J. E. (1969). Organization of the retina of the mudpuppy, Necturus maculosus. II. Intracellular recording. *Journal of neurophysiology, 32*(3), 339-355.

Wiesel, T. N., & Raviola, E. (1977). Myopia and eye enlargement after neonatal lid fusion in monkeys. *Nature, 266*(5597), 66-68.

Willecke, K., Eiberger, J., Degen, J., Eckardt, D., Romualdi, A., Güldenagel, M., . . . Söhl, G. (2002). Structural and functional diversity of connexin genes in the mouse and human genome. *Biol Chem*, *383*(5), 725-737. doi:10.1515/bc.2002.076

Wolsley, C. J., Saunders, K. J., Silvestri, G., & Anderson, R. S. (2008). Investigation of changes in the myopic retina using multifocal electroretinograms, optical coherence tomography and peripheral resolution acuity. *Vision Res*, *48*(14), 1554-1561. doi:https://doi.org/10.1016/j.visres.2008.04.013

Yinon, U., Rose, L., & Shapiro, A. (1980). Myopia in the eye of developing chicks following monocular and binocular lid closure. *Vision Res*, *20*(2), 137-141.

Zhang, D. Q., Zhou, T. R., & McMahon, D. G. (2007). Functional heterogeneity of retinal dopaminergic neurons underlying their multiple roles in vision. *J Neurosci*, *27*(3), 692-699. doi:10.1523/jneurosci.4478-06.2007

Zhou, X., Pardue, M. T., Iuvone, P. M., & Qu, J. (2017). Dopamine signaling and myopia development: What are the key challenges. *Prog Retin Eye Res*, *61*, 60-71. doi:10.1016/j.preteyeres.2017.06.003

Zhou, X., Shen, M., Xie, J., Wang, J., Jiang, L., Pan, M., . . . Lu, F. (2008). The development of the refractive status and ocular growth in C57BL/6 mice. *Invest Ophthalmol Vis Sci*, *49*(12), 5208-5214. doi:10.1167/iovs.07-1545

7.1 Appendix 1

Email permission

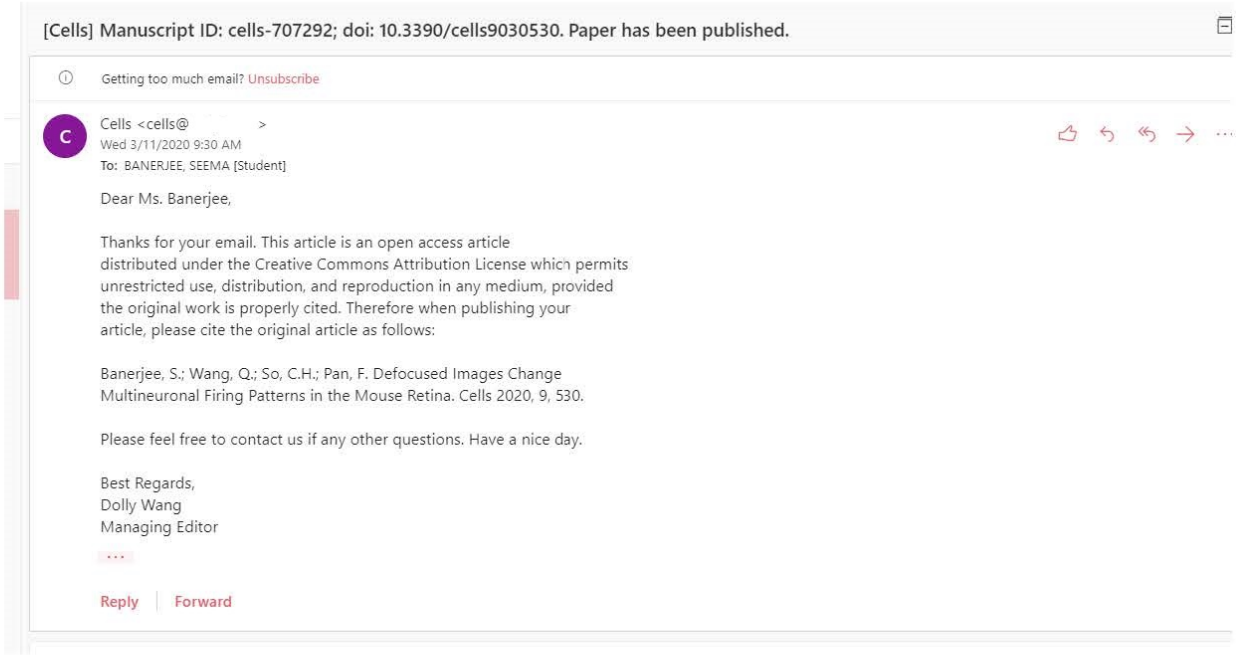

[Cells] Manuscript ID: cells-707292; doi: 10.3390/cells9030530. Paper has been published.

Getting too much email? Unsubscribe

Cells <cells@ >
Wed 3/11/2020 9:30 AM
To: BANERJEE, SEEMA [Student]

Dear Ms. Banerjee,

Thanks for your email. This article is an open access article distributed under the Creative Commons Attribution License which permits unrestricted use, distribution, and reproduction in any medium, provided the original work is properly cited. Therefore when publishing your article, please cite the original article as follows:

Banerjee, S.; Wang, Q.; So, C.H.; Pan, F. Defocused Images Change Multineuronal Firing Patterns in the Mouse Retina. Cells 2020, 9, 530.

Please feel free to contact us if any other questions. Have a nice day.

Best Regards,
Dolly Wang
Managing Editor

Reply | Forward

7.2 Appendix 2

Code for focused and defocused images used for stimulation

0.2 multiple dot 5x5

```
import numpy

from ctypes import windll

from psychopy import visual, event, core

#create a window

# Some variables and a window

dotSpaceX = 100

dotSpaceY = 100

win = visual.Window(size=(800,600), color=(-1,-1,-1))

# Create a matrix with 0's and 1's. Here a 10x10 identity-matrix

dotMatrix = numpy.array([[0,0,0,0,0],[0,0,0,0,0],[0,0,0,0,0],[0,0,0,0,0],[0,0,0,0,0]])

# Loop through each element of matrix. x and y are used to position stimulus. value is used to color
it

for x, row in enumerate(dotMatrix):

    for y, value in enumerate(row):

        # Specify color for values. Here in RGB code

        if value == 0: dotColor = (1,1,1)

        if value == 1: dotColor = (0,0,0)

    # Translate coordinates into something appropriate for your window

        xpos = (x-dotMatrix.shape[0]/2)*dotSpaceX
```

```
        ypos = (y-dotMatrix.shape[1]/2)*dotSpaceY

        # Actually draw circle with dotColor, xpos and ypos.

        # Technical note: I don't assign each visual.Circle to a variable. I just draw it and throw it away so it doesn't fill up memory.

        #visual.Circle(win, pos=(xpos,ypos), fillColor=dotColor, lineColor=None, radius=dotRadius).draw()

        grating = visual.GratingStim(win=win, units="pix", size=[60, 60], pos=(xpos,ypos), ori=0.0)

        grating.sf = 20 / 100.0

        grating.mask = "gauss"

        grating.draw()

        print (x,y,value, xpos, ypos)

# Ok, all circles have been drawn. Now create one single stimulus - let's call it "stim1". Empty   buffer with a win.flip() afterwards.

     stim1 = visual.BufferImageStim(win)

      win.flip

       for i_stim in range(1, 100):

        stim1.draw()

        stim1.setOpacity(1)

        stim1.draw(win)

        stim1.draw()

        win.flip()

        windll.inpout32.Out32(0x378, 255) # set all pin high

        core.wait(1, 0.2)

        stim1.setOpacity(0)

        stim1.draw(win)
```

```
win.flip()
windll.inpout32.Out32(0x378, 0) # set all pin low
core.wait(5, 0.2)
```

0.5 multiple dot 5x5

```
import numpy
from ctypes import windll

from psychopy import visual, event, core
#create a window
# Some variables and a window
dotSpaceX = 100
dotSpaceY = 100
win = visual.Window(size=(800,600), color=(-1,-1,-1))
# Create a matrix with 0's and 1's. Here a 10x10 identity-matrix
dotMatrix = numpy.array([[0,0,0,0,0],[0,0,0,0,0],[0,0,0,0,0],[0,0,0,0,0],[0,0,0,0,0]])

# Loop through each element of matrix. x and y are used to position stimulus. value is used to color it
for x, row in enumerate(dotMatrix):
    for y, value in enumerate(row):
        # Specify color for values. Here in RGB code
        if value == 0: dotColor = (1,1,1)
```

```
    if value == 1: dotColor = (0,0,0)


    # Translate coordinates into something appropriate for your window

    xpos = (x-dotMatrix.shape[0]/2)*dotSpaceX

    ypos = (y-dotMatrix.shape[1]/2)*dotSpaceY


    # Actually draw circle with dotColor, xpos and ypos.

    # Technical note: I don't assign each visual.Circle to a variable. I just draw it and throw it away so it doesn't fill up memory.

    #visual.Circle(win, pos=(xpos,ypos), fillColor=dotColor, lineColor=None, radius=dotRadius).draw()

    grating = visual.GratingStim(win=win, units="pix", size=[60, 60], pos=(xpos,ypos), ori=0.0)

    grating.sf = 50 / 100.0

    grating.mask = "gauss"

    grating.draw()

    print (x,y,value, xpos, ypos)


# Ok, all circles have been drawn. Now create one single stimulus - let's call it "stim1". Empty buffer with a win.flip() afterwards.

stim1 = visual.BufferImageStim(win)

win.flip


for i_stim in range(1, 50):

    stim1.draw()

    stim1.setOpacity(1)
```

```
        stim1.draw(win)
        stim1.draw()

        win.flip()

        windll.inpout32.Out32(0x378, 255) # set all pin high

        core.wait(1, 0.2)
        stim1.setOpacity(0)

        stim1.draw(win)
        win.flip()
        windll.inpout32.Out32(0x378, 0) # set all pin low
        core.wait(5, 0.2)

# ... and draw it
stim1.draw()
win.flip()
event.waitKeys()

# ... and draw it
stim1.draw()
win.flip()
event.waitKeys()
```

7.3 Appendix 3

Illustration of the plasticity of gap junctions in AII-ACs in myopic and normal retina (Banerjee, Wang, Zhao, et al., 2020).

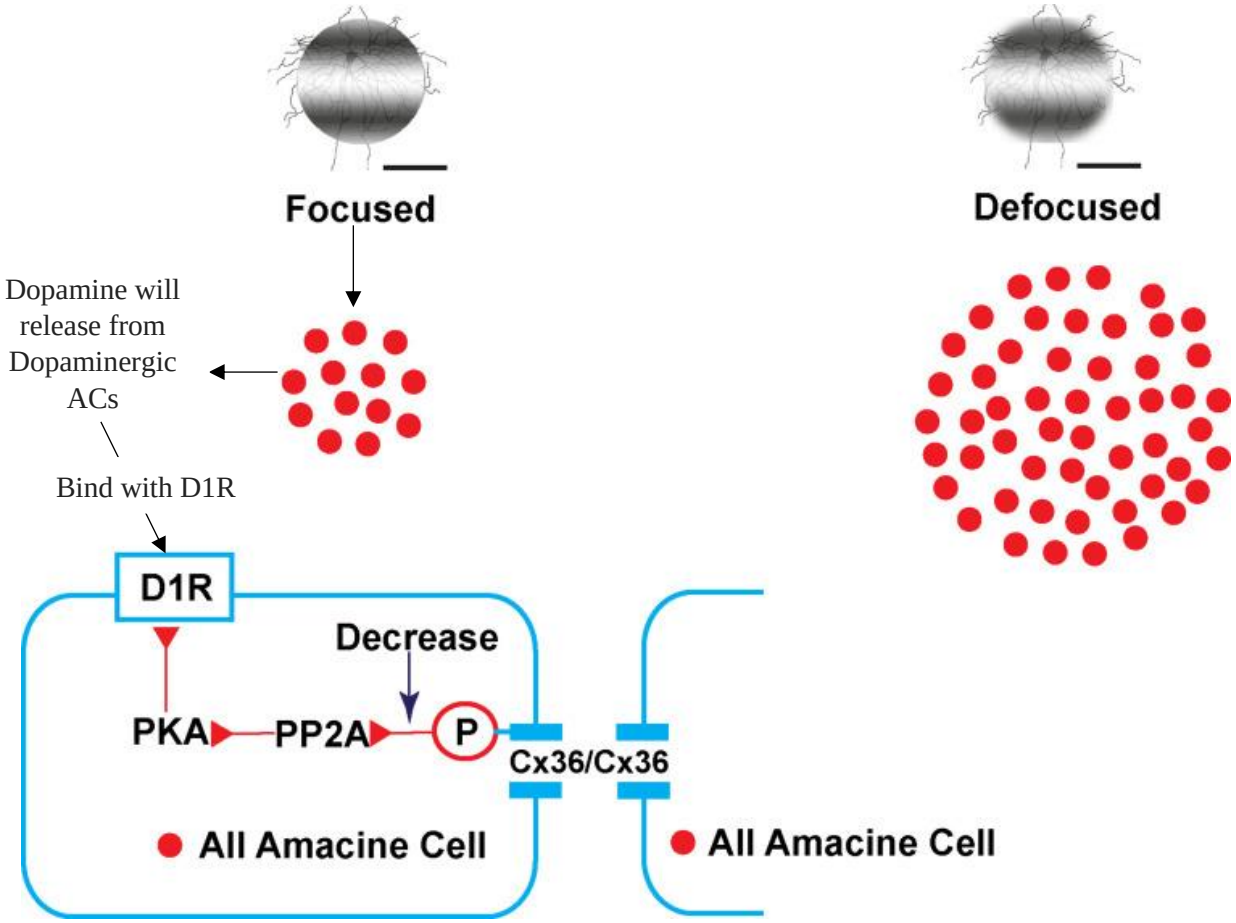

When images are focused on the retina (left), dopamine will be released from dopaminergic ACs, which will further bind with D1R activating the cAMP-dependent protein kinase α (PKA) and protein phosphatase 2A (PP2A), Which in turn dephosphorylates Cx36 gap junctions, thereby reducing the gap junction's conductance. In contrast, decreased dopamine increases the conductance of Cx36 in AII ACs by increasing the phosphorylation in the defocused status of the myopic retina (right).

7.4 Appendix 4

Enlarged view of the OPL to show the functional form of Cx36, shown in red punctate (Banerjee, Wang, Zhao, et al., 2020).

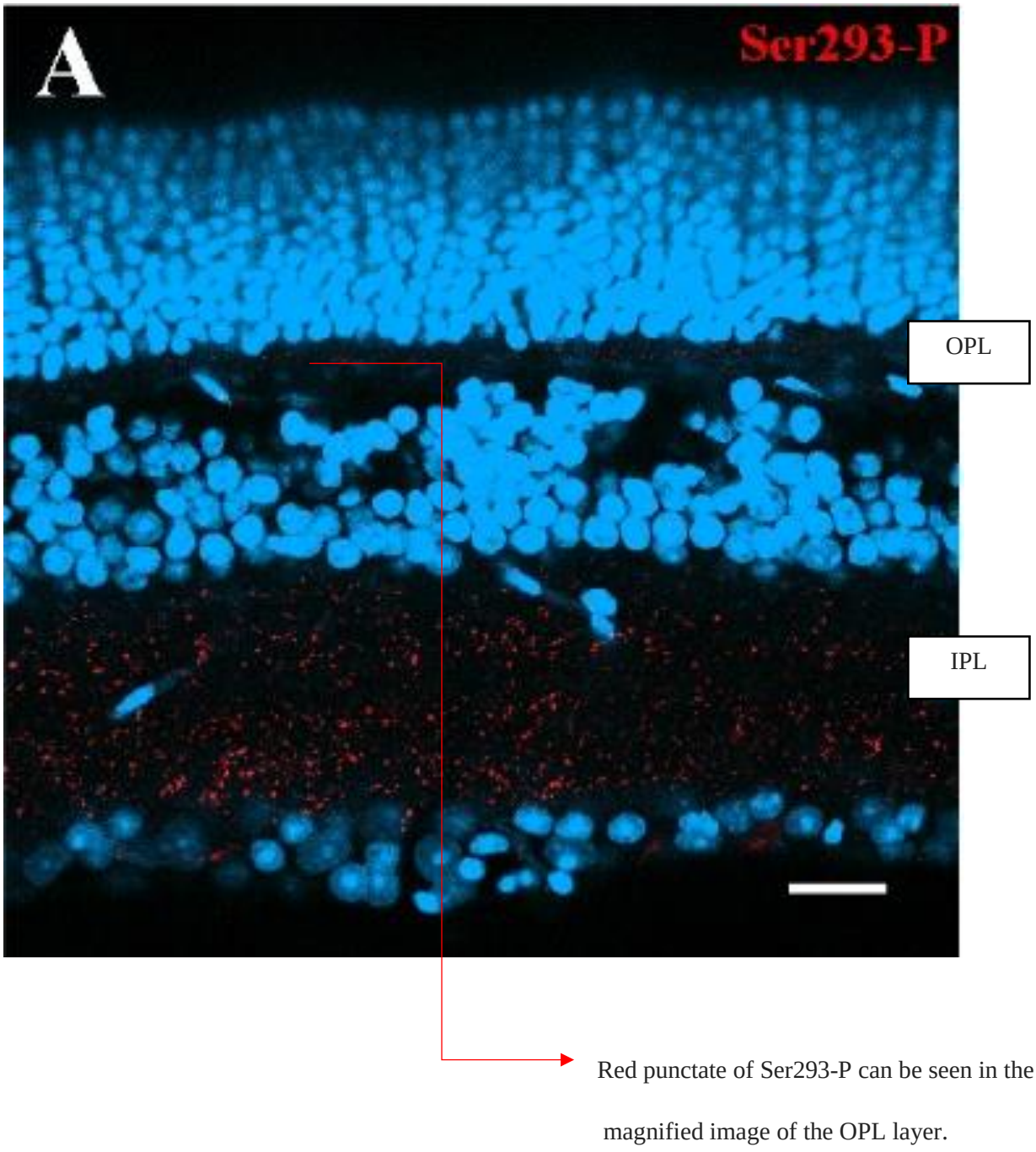

7.5 Appendix 5

ON RGC (Banerjee, Wang, Zhao, et al., 2020).

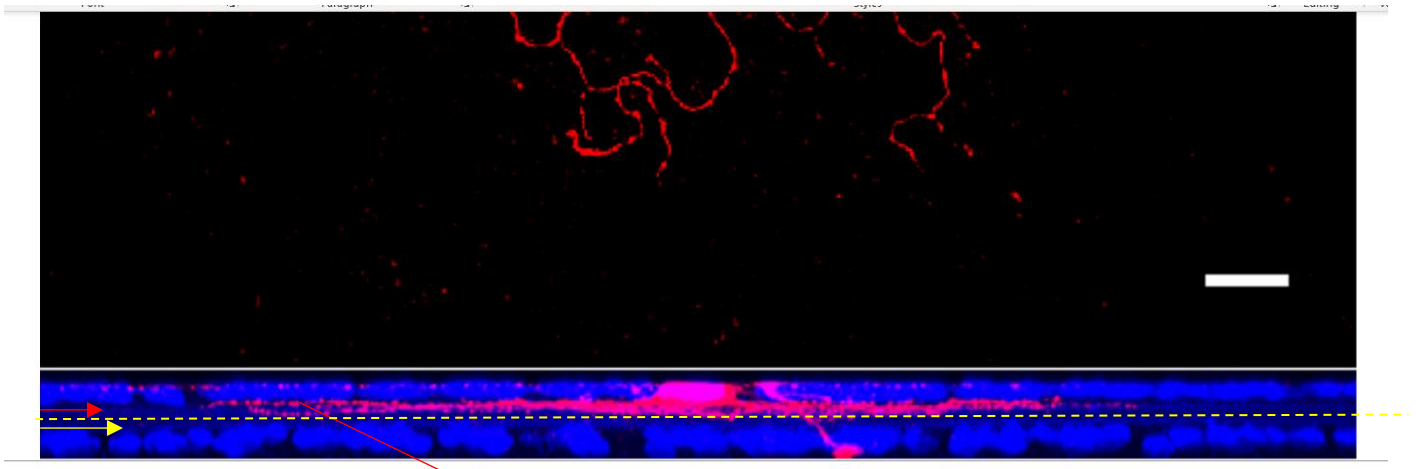

Sublamina b (red arrow) Dendrites of the ON RGCs are in the sublamina b

Sublamina a (yellow arrow)

OFF RGC (Banerjee, Wang, Zhao, et al., 2020).

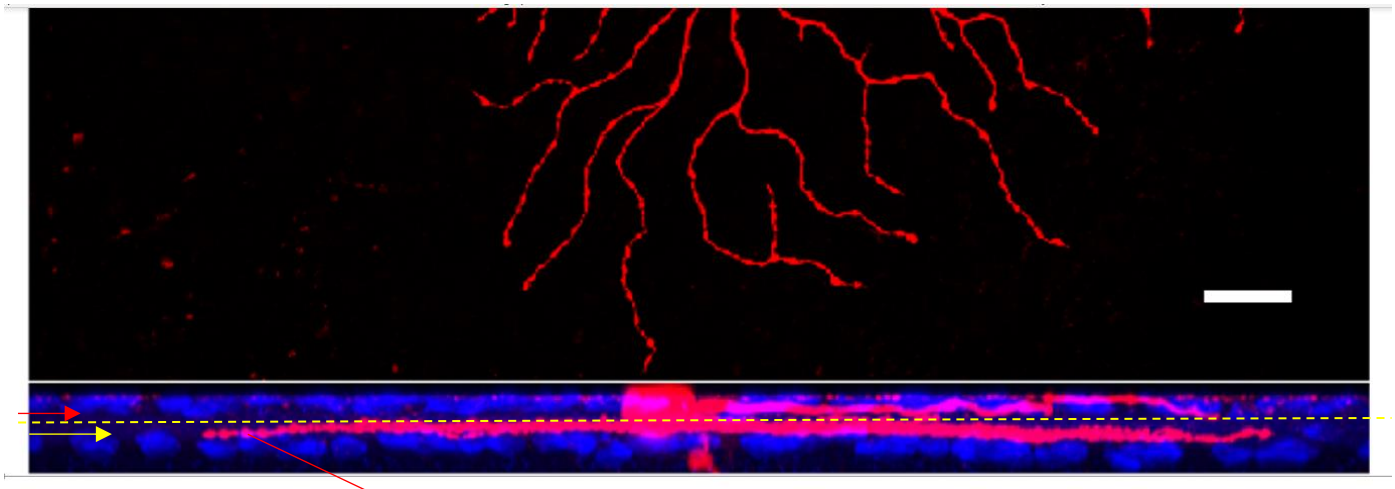

Dendrites of the OFF RGCs are in the sublamina a

Sublamina b (red arrow)

Sublamina a (yellow arrow)

7.6 Appendix 6

Functional RGCs types of mouse retina (Baden et al., 2016)

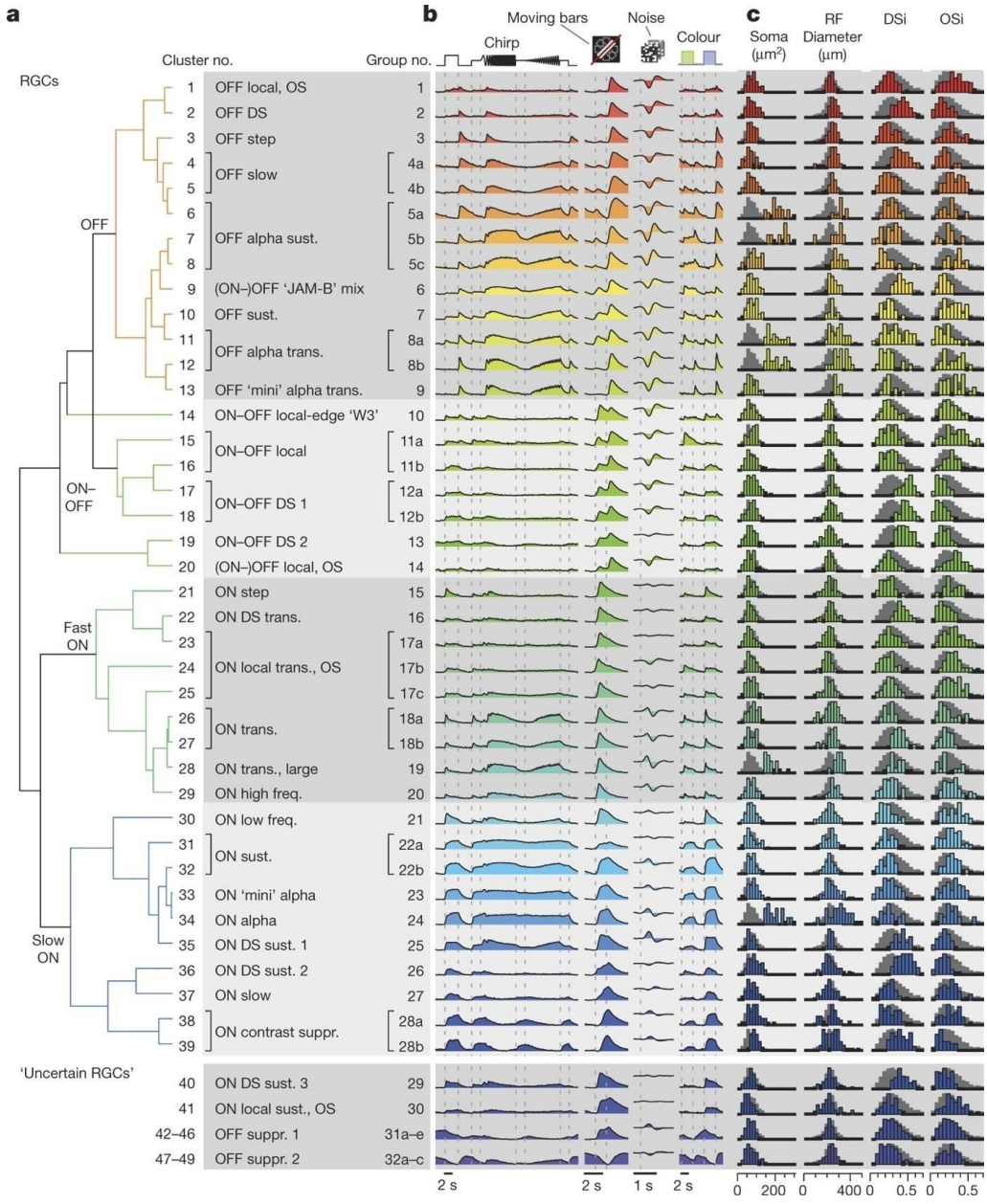

(a). Cluster-dendrogram (Methods) with groups indicated: $n = 28$ RGC and $n = 4$ 'uncertain' RGC groups. **(b).** Cluster-mean Ca^{2+} responses to the four stimuli. **(c).** Selected metrics, from left to right: region of interest (soma) area, receptive field (RF) diameter (2 s.d. of Gaussian), direction-selectivity index (DSi) and orientation-selectivity index (OSi) (Methods). Background-histograms demarcate all RGCs.

7.7 Appendix 7

Illustration of the MEA methodology, (Jalligampala, Sekhar, Zrenner, & Rathbun, 2017).

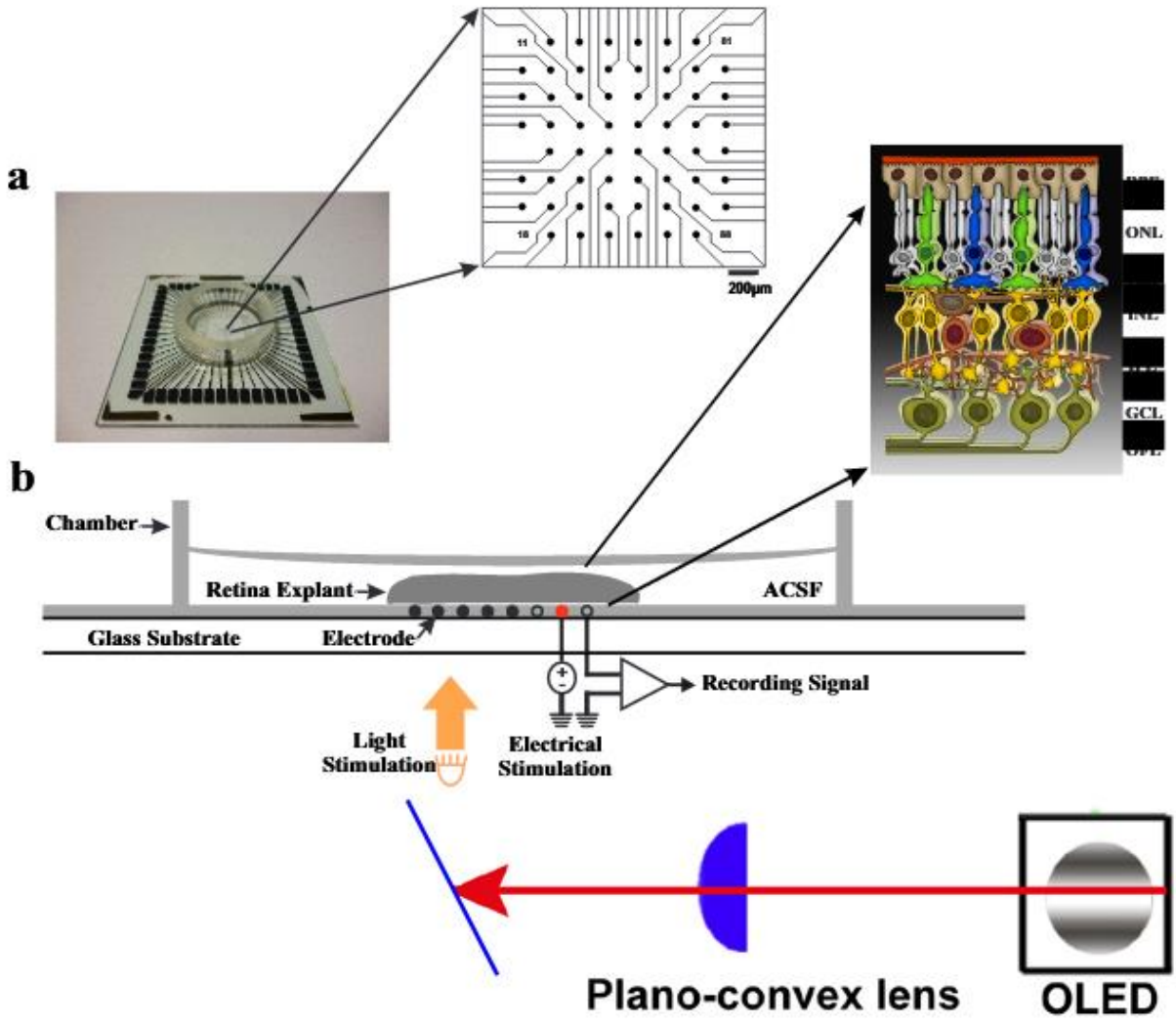

Figure: (a) shows the glass electrode MEA chamber design. (b) showing the overall procedure of the MEA recording of the mouse retina.

7.8 Appendix 8

OFF- Delayed cell (Banerjee, Wang, So, et al., 2020).

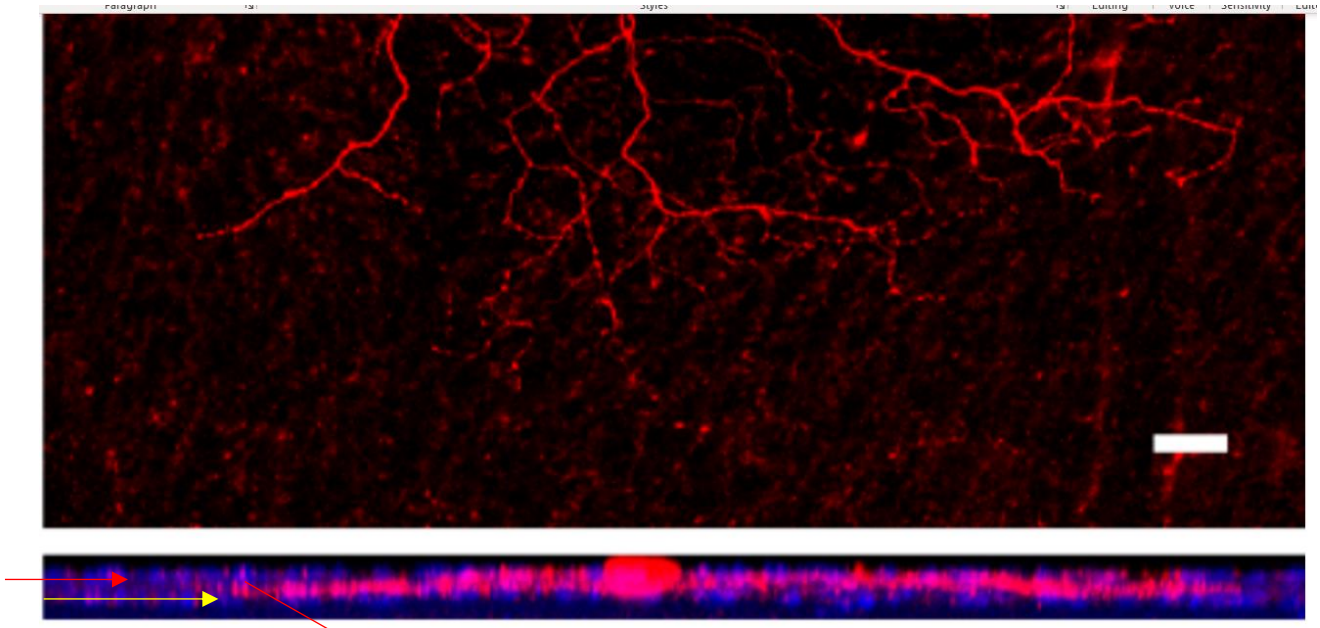

Sublamina b (red arrow)

Sublamina a (yellow arrow)

Dendrites of the OFF RGCs are in the sublamina a, irrespective of the delay because we classify them based on their response to the light stimulus.